

© Copyright by Siu Chun Michael Ho, 2012
All Rights Reserved.

Development of Advanced Fiber Bragg Grating Based Sensors

A Dissertation

Presented to

the Faculty of the Department of Mechanical Engineering

University of Houston

In Partial Fulfillment

of the Requirements for the Degree

Doctor of Philosophy

in

Mechanical Engineering

by

Siu Chun Michael Ho

December 2012

DEVELOPMENT OF ADVANCED FIBER BRAGG GRATING BASED SENSORS

Siu Chun Michael Ho

Approved:

Chair of the Committee
Gangbing Song, Professor
Mechanical Engineering

Committee Members:

Matthew Franchek, Professor
Mechanical Engineering

Yi-Lung Mo, Professor
Civil and Environmental Engineering

Li Sun, Associate Professor
Mechanical Engineering

Mehdi Razavi, Associate Professor
Texas Heart Institute

Suresh K. Khator, Associate Dean
Cullen College of Engineering

Pradeep Sharma, Professor and Chair
Mechanical Engineering

Acknowledgements

I am profoundly grateful to Dr. Song for his support, guidance and encouragement during my studies as a graduate student. Dr. Song introduced me to the important and intriguing field of smart materials, and fiber optic sensors in particular. He has given me the opportunity to acquire diversified experience with many different people and research topics. I am obliged to Dr. Mehdi Razavi for his joint effort in the development of the fiber Bragg grating contact sensor for ablation catheters (chapter three). He provided me with vital knowledge and guidance from the perspective of a physician. I would like to thank Dr. Yi-Lung Mo for his indispensable collaboration during the investigation of using fiber Bragg grating sensors for measuring bond slip in prestressed concrete bridge girders (chapter seven). I would also like to thank Dr. Ren Liang's valuable suggestions for the development of dynamic fiber Bragg grating sensor system (chapter five). Special thanks go to Dr. Matthew Franchek for his generous mentorship since I was a freshman at UH. I would like to express my appreciation to all the committee members for their valuable time and suggestions.

I would like to show my gratitude towards all my colleagues from the Smart Materials and Structures Lab for their unwavering friendship and moral support. In particular are Dr. Claudio Olmi and Dr. Mithun Singla for their help with instrumentation; Mr. Devendra Patil for his expertise in mechanical design and chocolate connoisseurship; Ms. Christiana Chang for willingly presenting my papers in conferences when I was unable attend personally, and Mr. Qingzhao Kong and Mr. Jiabiao Ruan for their assistance on electronics. Last but not least is my family for their love and support throughout the course of my graduate studies.

Development of Advanced Fiber Bragg Grating Based Sensors

An Abstract

of a

Dissertation

Presented to

the Faculty of the Department of Mechanical Engineering

University of Houston

In Partial Fulfillment

of the Requirements for the Degree

Doctor of Philosophy

in

Mechanical Engineering

by

Siu Chun Michael Ho

December 2012

Abstract

The discovery of fiber optics opened the door to a vast new world of possibilities in sensing technology. One important class of fiber optic sensor is the fiber Bragg grating (FBG) structure. The compactness and low loss properties of the FBG make it a highly versatile sensor, and has allowed efficient deployment of FBGs in many different technological fields.

This dissertation describes five innovative designs and applications of FBG-based sensors. An FBG sensor was used as a contact level sensor allowing surgeons to gauge their level of contact with the heart wall in order to avoid perforation during cardiac ablation procedures. The sensor was able to determine the onset of contact and was also able to observe a potential warning sign of impending perforation.

The second FBG-based sensor was developed for detecting harmful water ingress in civil structures. Through the use of super absorbent polymers (SAPs) and an innovative sensor design, the sensor was able to undergo multiple loading cycles (up to 1 mL was tested) as well as survive flooding conditions.

The third FBG-based sensor comprised of two wavelength matched FBG for the measurement of high frequency vibrations. Measurement of acoustic vibrations generated by a piezoelectric wafer up to 100 KHz was demonstrated. A basic identification of a model wind turbine blade was performed using this set up.

An FBG sensor network consisting of multiplexed strain, temperature, and water sensors (23 sensors total) was deployed for the monitoring of a grout cube that models

the wall of a nuclear containment facility. Cracking, thermal fluctuations and water ingress were detected by the FBG sensor network over a period of about two months.

Finally, FBG strain sensors were used to develop a method for the local measurement of bond slip in reinforcing tendons of a prestressed concrete bridge girder. The method allowed the tracking of the entire bond slip process from a local perspective, which was, up to now, not yet accomplished using conventional sensors.

Table of Contents

Acknowledgements	v
Abstract	vii
Table of Contents	ix
List of Figures	xiv
List of Tables	xix
Chapter 1 Introduction	1
1.1. Motivation and Objectives	1
1.2. Contribution	5
1.3. Organization.....	6
Chapter 2 Introduction to Fiber Bragg Grating Sensors	9
2.1. Fiber optics.....	9
2.2. Extrinsic vs. Intrinsic Fiber Optic Sensors	10
2.3. Fiber Bragg Gratings.....	11
2.3.1. Strain and Temperature Sensing	16
2.3.2. Interrogation of FBGs	17
Chapter 3 Contact Sensor for Ablation Catheter	19
3.1. Introduction.....	19
3.1.1. Background	19
3.1.2. Literature.....	20

3.2. Sensor Design	22
3.2.1. Sensor Construction	22
3.3. Experimental Setup.....	26
3.3.1. Bench Tests	26
3.3.2. Ballistics Gel	26
3.3.3. Porcine heart	26
3.3.4. Animal Tests	26
3.4. Results.....	28
3.4.1. Ballistics Gel	28
3.4.2. Porcine Heart	29
3.4.3. Animal Test.....	31
3.5. Discussion	39
3.5.1. Ballistics Gel	39
3.5.2. Porcine Heart	39
3.5.3. Animal Test.....	40
3.6. Conclusions.....	44
 Chapter 4 A Fiber Bragg Grating Sensor for Detection of Liquid Moisture in Concrete Structures	 45
4.1. Introduction.....	45
4.1.1. Literature	45

4.2. Sensor Design	50
4.2.1. Housing and transduction mechanism	50
4.3. Model/Characterization.....	52
4.3.1. Swelling Model	52
4.3.2. FBG Model	53
4.3.3. Combined Model	54
4.4. Experimental Setup.....	57
4.4.1. Polymer Swelling Characterization	57
4.4.2. Sensor Cycling	57
4.4.3. Flooding Simulation.....	58
4.5. Results.....	59
4.5.1. Polymer Swelling Characterization	59
4.5.2. Sensor Cycling	59
4.5.3. Flooding Simulation.....	66
4.6. Discussion	68
4.7. Conclusions.....	72
Chapter 5 Dynamic Fiber Bragg Grating Sensing Method.....	74
5.1. Introduction.....	74
5.2. System Design	76
5.3. Calculation of spectral width	77

5.4. Experimental Setup.....	82
5.4.1. Experiment 1 – FBG sensor directly bonded to PZT actuator.....	83
5.4.2. Experiment 2 – FBG sensor bonded at a distance away from PZT actuator	84
5.4.3. Simulation.....	85
5.5. Results.....	86
5.5.1. Experiment 1 – FBG sensor directly bonded to PZT actuator.....	86
5.5.2. Experiment 2 – FBG sensor bonded at a distance away from PZT actuator	87
5.6. Discussion	93
5.7. Conclusions.....	96
Chapter 6 Fiber Grating Sensor Network for the Structural Health Monitoring of a Medium Scale Grout Structure	97
6.1. Introduction and Literature Review of FBGs in Structural Health Monitoring.....	97
6.1.1. Strain sensors	100
6.1.2. Temperature sensors	103
6.1.3. Water sensors	104
6.2. Application of FBGs in the SHM of Nuclear Containment Facilities	105
6.2.1. Sensors	107
6.2.2. Experimental Setup.....	109
6.2.3. Results.....	112
6.2.4. Discussion	117

6.2.5. Conclusion	120
Chapter 7 FBG Based-Bond Slip Detection of Prestressed Tendons in Concrete Bridge	
Girders.....	121
7.1. Introduction.....	121
7.1.1. Background.....	121
7.1.2. Bond Slip in Reinforced Concrete	121
7.1.3. Detection of bond slip.....	122
7.2. Experimental Program	125
7.2.1. Concrete Girder Construction and Testing	125
7.3. Experimental Results	130
7.3.1. LVDT Readings	130
7.3.2. FBG Readings.....	131
7.4. Discussion of FBG Based-Bond Slip Detection	133
7.5. Conclusions.....	136
Chapter 8 General Conclusions and Future Work	137
References	139
Appendix I	155

List of Figures

Figure 2-1. The schematic of a generic fiber optic.	9
Figure 2-2. Examples of fiber optic sensors.	11
Figure 2-3 An illustration of how an FBG operates. An uniform FBG is shown.....	13
Figure 2-4. Reflection spectrum of a uniform Type I FBG.	15
Figure 3-1. (A) Schematic of the sensor head. (B) Photos of the sensor exterior and interior.....	23
Figure 3-2. (A) Pushing of the sensor through the left atrial wall. The sensor tip is visible through thin tissue. (B) Completion of perforation. Forceps were used to assist this particular perforation.	27
Figure 3-3. Perforation of ballistics gel slab using epoxy-based sensor.....	28
Figure 3-4. Perforation of ballistics gel slab using urethane-based sensor.....	29
Figure 3-5. Perforation of LA using epoxy-based sensor (over 8 s, with 0.035 nm shift in wavelength).....	30
Figure 3-6. Perforation of LA using urethane-based sensor (over 3 s, with 0.04 nm shift in wavelength).....	30
Figure 3-7 Contact of epoxy-based sensor with left atrium.....	32
Figure 3-8. Zoom in of signals during contact.....	32
Figure 3-9 Contrast between resting and contact for epoxy-based sensor.....	33
Figure 3-10. Contrast between resting and contact for urethane-based sensor.....	33
Figure 3-11. Resting and Contact inside the left ventricle for urethane-based sensor.	34
Figure 3-12. Perforation of left atrium using epoxy-based sensor.....	36
Figure 3-13. Perforation of left atrium using epoxy-based sensor with positive loading curve.....	36

Figure 3-14 Perforation of left atrium using epoxy-based sensor.....	37
Figure 3-15. Perforation of left atrium using urethane-based sensor.....	37
Figure 3-16. Perforation of left atrium using urethane-based sensor.....	38
Figure 4-1. (A) Top-down view of the housing without the middle cover. (B) Overall perspective of the water sensor housing. (C) Side view of the sensor housing. (D) Axial view of the sensor housing.....	50
Figure 4-2. Two different sensor configurations were used. (left) Free configuration. (right) Rail configuration – wires were used to restrict lateral movement of the polymer bead.....	51
Figure 4-3. Graphical representation of the simplified water sensor.....	54
Figure 4-4. Approximation of the beam deformation due to deflection.	55
Figure 4-5. Experimental set up for testing the water sensors.....	58
Figure 4-6. Submersion of FBG water and temperature sensor into a water bath.....	59
Figure 4-7. 0.1 mL of drinking water was input into the Free configuration sensor six times.....	60
Figure 4-8. 0.3 mL of drinking water was input into the Free and Rail configuration sensor four times.	61
Figure 4-9. 0.5 mL of drinking water was input into the Free and Rail configuration sensor three times.....	62
Figure 4-10. 0.7 mL of drinking water was input into the Free and Rail configuration sensor three times.....	63
Figure 4-11. 1.0 mL of drinking water was input into the Free and Rail(x4) configuration sensor three times.	64

Figure 4-12. Average peak amplitude (with standard deviation) for increasing input volumes into the Free sensor configuration.	65
Figure 4-13. Average peak amplitude (with standard deviation) for increasing input volumes into the Rail sensor configuration.	66
Figure 4-14. Flooding test for both sensor configurations.....	67
Figure 4-15. Photo of water sensors under flooding conditions. (A) (Left) Flooded situation for Free configuration, (Right) Dried sensor after flooding; (B) (Left) Flooded situation for Rail configuration, (Right) Dried sensor after flooding.	67
Figure 4-16 Different stages of loading for the Rail configuration sensor. A) Initial loading; B-C) Contact with rails and continued expansion; D) Saturation of sensor and cracking of polymer bead.....	70
Figure 5-1. Optical circuit of the wavelength-matched dynamic FBG sensing system....	76
Figure 5-2. Comparison of FBG Reflectivity Models.	78
Figure 5-3. Tracing of the optical power along the sensor system's optical circuit.	79
Figure 5-4. Comparison of the relevant spectrums of FBG1 and FBG2.	80
Figure 5-5. Photodetector power versus wavelength mismatch between FBG1 and FBG2.....	82
Figure 5-6. Set up of Experiment 1.....	83
Figure 5-7. Set up of Experiment 1 (photo).....	84
Figure 5-8. Relative location between the FBG and the PZT patch.	85
Figure 5-9 Time domain response of the FBG sensor to a sweep sine excitation (bonded to PZT wafer).....	86
Figure 5-10. Power spectral density of the sweep sine response (bonded to PZT wafer). 87	

Figure 5-11. Initial portion of the sweep sine result.	88
Figure 5-12. Power spectral density of sweep sine response.....	88
Figure 5-13. Impulse response of the turbine blade as sensed by the FBG sensor system.	89
Figure 5-14. Dominant natural frequencies of the turbine blade as measured by the FBG sensor system.....	90
Figure 5-15. Impulse response of the turbine blade as sensed by the PZT patch.	91
Figure 5-16. Natural frequencies of the turbine blade as measured by the PZT patch....	91
Figure 5-17 Comparison of the experimental and simulation results.	92
Figure 5-18. Zoom in of the data showing slight discrepancies between the results.....	93
Figure 6-1. Schematic of FBG strain sensor.	101
Figure 6-2. Schematic of FBG temperature sensor.....	103
Figure 6-3. Schematic of FBG water sensor.	104
Figure 6-4. Calibration for FBG sensors (Left) Strain sensor, (Right) Temperature sensor.	108
Figure 6-5. Response of water sensor to <0.5 mL volume of water.	108
Figure 6-6 (Left) Top-down view of grout cube schematic, (Right) Photo of sensor panel.....	109
Figure 6-7 (Left) Sensor and data acquisition system configuration. (Right) Example of sensor cluster (Panel 5).....	110
Figure 6-8 (Top Left) Panels 1 and 9 sensor cluster placement. (Top Right) Panels 3 and 7 sensor cluster placement (Bottom) Panel 5 sensor cluster placement.....	111
Figure 6-9 Strain sensor results from January 17 to March 3, 2012 (Panels 1, 3, 5). ...	113

Figure 6-10 Strain sensor results from January 17 to March 3, 2012 (Panels 5, 7, 9). .	113
Figure 6-11 Temperature sensor results from January 17 to March 3, 2012 (Panels 1, 3, 5).	114
Figure 6-12 Temperature sensor results from January 17 to March 3, 2012 (Panels 5, 7, 9).	115
Figure 6-13 Water sensor results from January 17 to March 3, 2012 (Panels 1, 3, 5)..	116
Figure 6-14 Water sensor results from January 17 to March 3, 2012 (Panels 5, 7, 9)..	116
Figure 7-1 Bond stress vs bond slip behavior (adapted from CEB-FIP).	122
Figure 7-2 Cross section of tested girder Tx28.....	126
Figure 7-3 Experimental set-up of the girder loading experiment.....	127
Figure 7-4 Layout of the Selected Tendons with LVDTs.....	128
Figure 7-5 (Left) Installation of FBG sensors onto the tendons prior to concrete pouring. (Right) Strain sensors are bonded via cyanoacrylate to the tendons.	129
Figure 7-6. Relative placement of FBG sensors in the concrete girder along the top row of tendons.	129
Figure 7-7 Measured Global Slip versus Shear Force.	131
Figure 7-8 Measured Local Slip versus Shear Force. a) Strain profile for sensor SG1..	132
Figure 7-9. Close up of SG2 readings near girder failure.....	135
Figure 9-1 Calibration curve of FBG temperature sensor.	155
Figure 9-2 Calibration curve of FBG strain sensor.....	155

List of Tables

Table 2-1 The domains in which FOSs have been used, along with specific applications	10
Table 3-1. Parameters used for estimation of average strain transfer.....	25
Table 4-1. Summary of the cycling experiment.....	58
Table 4-2. Summary of cycling results for both sensor configurations.....	65
Table 6-1. Parameters relevant to SHM [95]	98
Table 6-2 Sensors used during the SHM experiment.	109
Table 6-3 Summarization of sensor placement throughout the sensor network and the grout cube.....	111
Table 7-1 FBG strain (short and long gauge) and temperature sensors used during the experiment. Each sensor was encapsulated in a stainless steel casing to provide robustness.....	124
Table 7-2. Sensor placement within the girder.	130

Chapter 1 Introduction

One of the key, defining moments of 20th century technology was the discovery of fiber optics. Fiber optics have modernized the field of optical communications and opened the door to a vast new world of possibilities in sensing technology. Prior to the introduction of fiber optics, optical technology was composed mainly by bulk components and the requirement for extremely finely tuned instrumentation. All the advantages of using light as a tool for sensing were clouded by the general fragility and immobility of bulk optics. Components such as the laser source and beam splitters are vital in the operation of an optical system, and each requires careful handling and precise calibrations. With the development of the fiberized counterparts of such components, traditionally cumbersome optical technologies were freed for use in innumerable applications. One of the indispensable fruits and contributing driver of the fiber optic revolution is the fiber Bragg grating (FBG) structure. The compactness and low loss properties of the FBG make it a highly versatile sensor, and has allowed efficient deployment of FBGs in many different technological fields.

1.1.Motivation and Objectives

Many problems encountered in science and engineering require accurate and precise measurement of certain parameters in order to be solved. The measurement of the parameters is enabled through the use of the appropriate sensor, which depends on the constraints of the problem. Fiber optic sensors, FBGs in particular, have many advantages, such as high precision, electromagnetic (EM) immunity and compactness (more will be discussed in chapter two). These advantages allow FBGs to be used in

areas that conventional sensors cannot be used. The sensor developments described in chapters three through five are examples in which FBGs are able to perform sensing where conventional sensors would otherwise have difficulty functioning or be impractical.

One of the primary examples where fiber optics has opened the doors to new sensing possibilities is the field of medicine. Many diagnosis and treatment procedures, such as magnetic resonance imaging (MRI) and tissue ablation, involve the use of electronic equipment that emits strong EM fields. These EM fields are often strong enough to preclude the use of electronic sensors, as the fields will either produce an unacceptable amount of noise in the measurement or even disable the sensor. However, since fiber optics are inherently immune to EM interference, previously immeasurable parameters can now be measured. Chapter three illustrates the application of FBG sensors in cardiac ablation procedures. Tissue ablation using radio frequency (RF) emission requires large amounts of electrical power supplied to the ablating tip. Both the power supply and the emitted RF will render conventional electronic sensors unusable, but will not have any effect on fiber optic-based sensors. The objective of the experiment in chapter three was to enable the operator to gauge the contact level of the catheter against the endocardial surface, and investigate any anomalous signal behavior associated with the perforation of the heart wall with the catheter.

Emerging during the past few decades is the new concept of smart structures, where a structure is given a sort of nervous system allowing it to interact in a controllable manner with the environment. At the highest levels, the smart structure emulates the several key functions of a living, intelligent being. The smart structure can potentially sense the environment, react to it, and adapt to changing situations. Such functions are

enabled by a complex system composed of a sensor and actuator network, as well as a learning algorithm that evolves based on past experiences. The foundation supporting the higher functions such as physical control and learning is the sensor network, which allows the structure to observe the environment. The use of the sensor network by itself has led to the establishment of the field of structural health monitoring (SHM), where operators are able to measure the vital stats of a structure to determine its structural integrity. While many different types of materials and devices have been used successfully to implement smart structures and enable SHM, fiber optics are increasingly being used due to their advantages as mentioned previously. In this dissertation are several examples describing both the development of new FBG sensors and their applications towards unexplored areas of FBG-based SHM.

Chapter four begins the theme of SHM and describes the development of an FBG-based water sensor. Water ingress in a reinforced concrete structure can cause severe damage to the reinforcing members due to corrosion and reduce the overall life-time of the structure. While there are many commercially available sensors for the measurement of humidity levels, sensors for the detection of liquid moisture are still lacking. The FBG based water sensor used in chapter six had a limiting factor in that the sensor readings were not able to return to resting levels within practical time limits once an input volume of liquid moisture has been received. The objective of the work presented in chapter four was to improve the water sensor so that it can have repeatable loading cycles as well as survive extreme loading conditions (e.g., flooding). The theory described in chapter four also paves the way for the ability of the water sensor to measure the volume of input water instead of only detecting the presence of water.

Chapter five presents the development of a sensor for the detection of high frequency vibrations. In many situations, especially in SHM, the presence of high frequency vibrations can be an indicator for specific types of damage. On the other hand, some active sensing systems rely on the propagation of high frequency acoustic waves as a carrier of information between sensors. However, current FBG wavelength demodulation techniques often have limited ranges in sampling frequency due to components such as scanning optical filters. Reliable high frequency demodulation techniques while available can be costly. Several inexpensive high frequency sensing methods for FBGs have been proposed in the literature. The goal of the sensor setup in this chapter is to provide a comparatively inexpensive, alternative method for using FBGs in the dynamic measurement of high frequency vibrations, and may offer similarly alternative benefits depending on the situation requiring the use of such a set up.

Chapters six and seven present two examples in which FBG-based sensing methods were developed for tackling current problems in SHM. In chapter six, FBG sensors were used to monitor a model wall of a nuclear containment facility. The work in this chapter was motivated by the increasing number of decommissioning nuclear power plants around the world. Each decommissioning requires the careful inspection and monitoring of the radiation levels in a shut-down nuclear power plant before the space can be opened to public and used again. A certain procedure for decommissioning is to enclose the entire facility in a thick concrete wall that must last for many years. Thus the goal of the FBG sensor network is to monitor the wall and alert the operator should any damage occur.

In chapter seven, FBG sensors were used to investigate the bond slip in a prestressed concrete bridge girder. The prestressing of the tendons in a concrete girder provides the girder with extra strength in handling tensile loads. Unfortunately, as the girder accumulates damage and wears out over time, the bond between the tendon and the concrete weakens and diminishes the benefits provided by the prestressing. While many researchers have investigated the bond slip in steel rebar reinforcement, less study has been committed to the bond slip of steel tendons due to the harsh manufacturing conditions of prestressed structures with respect to conventional sensors. Furthermore, most studies only report the global slip of the reinforcing member and not the local slip along the reinforcing member. Therefore, a novel FBG-based method was developed to measure the local strain conditions of a slipping tendon in a prestressed concrete bridge girder and provide further insight into the mechanics of bond-slip in prestressed structures.

1.2.Contribution

Each chapter in this dissertation has contributions to their respective engineering problem. In chapter three, the contact sensor helps the operator to gauge the level of contact between the ablation catheter and the heart wall. At the current stage, the sensor works as a tool for the characterization of catheter-induced perforation in cardiac ablation procedures. An examination of the results show that through the use of this sensor, suggestions for the highest level of contact with the heart wall can be made, as well as reveal a potential pre-perforation signal that can be further studied in future work.

The new FBG based water sensor in chapter four firstly contributes itself as another tool that can be used to monitor the ingress of liquid moisture in concrete

structures. While primarily acting as a viable tool for the long term monitoring of liquid moisture ingress, the design of the sensor allows simple interchangeability in regards to the moisture-sensitive component. In future experiments, reagents sensitive to chemicals other than water can be used with this sensor design.

In chapter five, a dynamic FBG based sensing technique is added to the repertoire of FBG interrogation methods already available in the field. The contributions of this sensor include the straightforward realization of dynamic measurements using FBGs, and the potential reduction of costs normally associated with the usage of FBG systems. The analysis provided in the chapter can help the design of future systems that rely on a similar sensing principle.

In chapter six, a FBG sensor system was applied to the SHM of a model nuclear containment wall. The results provide information that can help the creation of more sophisticated and reliable measures for the monitoring of nuclear containment facilities.

Finally in chapter seven, FBG sensors were applied for use in detecting bond slip in prestressed bridge girders, and were able to provide a previously unseen perspective in regards to the local slip of prestressing tendons in a concrete bridge girder. This new information can serve as a benchmark for use in SHM and improve the safety of prestressed concrete support members.

1.3.Organization

This dissertation is organized into seven chapters. Chapter one introduces the background of fiber optics and FBGs, and the motivation of this dissertation.

Chapter two provides briefly describes the mechanism of fiber optics along with some general examples of fiber optic sensors. Afterwards, FBGs are given a basic introduction, including some of the relevant theory and interrogation methods.

Chapter three presents the development and use of FBGs in cardiac ablation surgery. Results ranging from bench-top tests to *in vivo* trials in adult sheep are included in this chapter. The sensor was able to detect and monitor contact with the endocardial surface as well as provide some insight into the mechanics of the mechanical perforation of the heart wall due to excessive pressure from the sensor (shaped as an ablation catheter).

Chapter four presents an improvement upon the water sensor described in chapter six. In chapter six, the FBG inside the water sensor was coated with super absorbent polymer (SAP) that swells in the presence of water, but had limited loading cycles. An improvement in the design was made in this chapter to allow extended amounts of loading cycles and easier interchangeability between SAP types.

Chapter five describes the development of a FBG optical circuit allowing the dynamic measurement of high frequency vibrations. In the optical circuit, two wavelength matched FBGs were used. The first FBG filters out optical power matching its center wavelength and minimizes the amount of light in that wavelength from reaching the second FBG. Any perturbances in the center wavelength of either FBG will increase the power of the reflection spectrum from the second FBG, thus causing change in the output of the photodiode observing the second FBG. This method allows the measurement of high frequency signals.

Chapter six shows a brief literature review of FBGs in SHM and describes the FBG sensors that will be used in both chapter six and seven. The work in chapter six involves the deployment of FBG sensors that separately measure strain, temperature and the presence of water. The FBG sensor network was used for the monitoring of a grout cube modeled after the walls of a nuclear containment facility.

In chapter seven, the strain and temperature FBG sensors are applied for use in the investigation of the bond slip phenomenon in prestressed concrete bridge girders. The FBG strain sensors were bonded directly onto the prestressing tendons and were able to monitor the entire bond slip process as it occurred.

Chapter eight closes the dissertation with some general conclusions regarding the research problems described in the previous chapters. Remarks regarding the future work of the work presented in this dissertation are also provided.

Chapter 2 Introduction to Fiber Bragg Grating Sensors

2.1. Fiber optics

Fiber optics is the result of research into methods for transmitting light across large distances with low loss (< 20 dB/km). The fiber optic generally consists of a core, a cladding, and an outer protective layer (Figure 2-1). Light propagates through the core, which is usually made of ultrapure silicon (SiO_2) with refractive index n_c . Other crystals such as sapphire (Al_2O_3) can be used to improve the transmittance of different wavelengths of light.. The cladding, which wraps around the core, has a smaller valued refractive index of n_L . When light is guided into the core at the critical angle θ , according to Snell's Law, it will propagate by totally reflecting off the core-cladding interface [1].

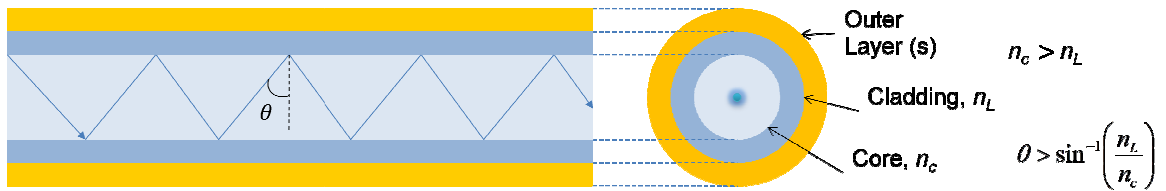


Figure 2-1. The schematic of a generic fiber optic.

Furthermore, by adjusting the diameter ratio of the core and the cladding, one can adjust the number of modes allowed to propagate through the fiber. Optical fibers allowing only one mode are *single-mode* fibers. On the other hand, *multimode* fibers can have up to millions of modes traveling simultaneously.

Fiber optics has also been used to sense a large variety of measurands due to the versatile properties of light. These fiber optic sensors are within a family of photonic/optical sensors [1]. In optical sensors, an external force alters the parameters of the light, such as amplitude, polarity, etc., contained within the system. The alteration is

detected and an output signal is emitted to signify the change. Optical sensors making use of fiber optics are often called Fiber Optic Sensors (FOS), or Optical Fiber Sensors (OFS) [1]. FOSs can be adapted to measure signals from multiple domains (Table 2-1) [1].

Table 2-1 The domains in which FOSs have been used, along with specific applications.

Domain	Signals
Mechanical	Vibrations, velocity, acceleration, pressure, displacement, temperature, flow and turbulence of fluids
Electromagnetic/Radiation	Electric fields, magnetic fields, current, X-rays, luminescent radiation, nuclear radiation
Bio/Chemical	Reactions, substrate concentrations, blood flow, genetic material

2.2. Extrinsic vs. Intrinsic Fiber Optic Sensors

Fiber optic sensors can be categorized into extrinsic and intrinsic sensors. Their fundamental difference lies in how they transduce their signals.

For extrinsic sensors (or hybrid), light exits the fiber and interacts with the measurand before returning or entering into another fiber. Essentially, a separate, external device is needed for the operability of extrinsic FOS. The use of fiber optics can replace electrical-based communication and allow sensing to take place in previously inaccessible areas. However, any disadvantages associated with the external device must now be considered. A common example of an extrinsic FOS is the reflection of the light beam of a moving mirror back into the transmitting fiber (Figure 2-2 Left).

Intrinsic FOS (or all fiber) operates by allowing the measurand to alter the intrinsic characteristics of optical transduction while the light beam remains fully or partially within the fiber optic. In other words, the properties of light within a fiber optic is changed an external force, and the magnitude and the nature of the change is used to determine the parameter to be sensed. Intrinsic sensors can thus bypass the disadvantages

of exposing light directly to an external environment or device. An example of an intrinsic FOS is the microbend sensor, where the bends in the transducer causes a loss of optical intensity of the light within the optical fiber (Figure 2-2 Right).

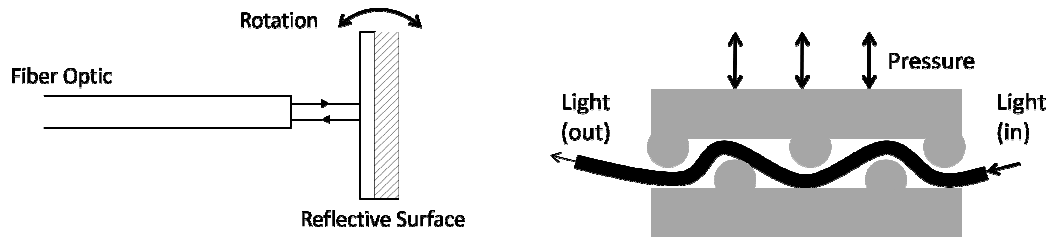


Figure 2-2. Examples of fiber optic sensors.

2.3.Fiber Bragg Gratings

Fiber Bragg gratings (FBGs) are a type of intrinsic, spectroscopic FOS and thus the wavelength of light is modulated while within the fiber. This is accomplished by the inscription of a reflective periodic pattern along a portion of the fiber core. The pattern is inscribed by exposing the desired portion of the core to the interference pattern of two precisely placed ultraviolet beams. For a uniform pattern, a UV beam can be split by a beam splitter and two mirrors can guide the two resulting beams to interfere with each other [1]. Other techniques exist for a variety of patterns to give different reflective spectrums, but their description is beyond the scope of this thesis.

For a fiber optic core with refractive index of n_c , an uniform pattern inscribed by the UV beam interference is composed of periodically spaced (with period Λ) sections/gratings with refractive index n_g . The difference between the refractive indices of the core and the gratings causes a small portion of the light to scatter. However, scattered light waves will have a net direction only if enough of the scattered light waves are in-phase in that direction. In the case of the FBG, the weak reflections from each

grating add up in-phase to generate a backward traveling light wave. The dominant backward mode has a wavelength of λ_b . This wavelength is also known as the resonant or Bragg wavelength, and is related to the grating period by

$$\lambda_b = 2n_e\Lambda \quad (2.1)$$

where n_e is the effective index of the reflected mode, which describes how light travels depending on its current mode [1]. Thus, any external force that may alter n_e or Λ will cause a direct and proportional change in the peak measured wavelength of the reflected light. The change in λ_B can be linearly correlated to changes in temperature T , strain ε , and pressure P through

$$\frac{\Delta\lambda_B}{\lambda_B} = \alpha_T\Delta T + \alpha_\varepsilon\Delta\varepsilon + \alpha_P\Delta P, \quad (2.2)$$

where α_T , α_ε , and α_P are the coefficients of temperature, strain, and pressure, respectively [1]. These coefficients are further related to the material properties of the fiber and the properties of the light propagating within the fiber. As seen from (2.2), strain, temperature and pressure have a coupled effect on the Bragg wavelength. Thus, practical sensors usually require a decoupling of these parameters. Figure 2-3 illustrates the operational principles of an FBG.

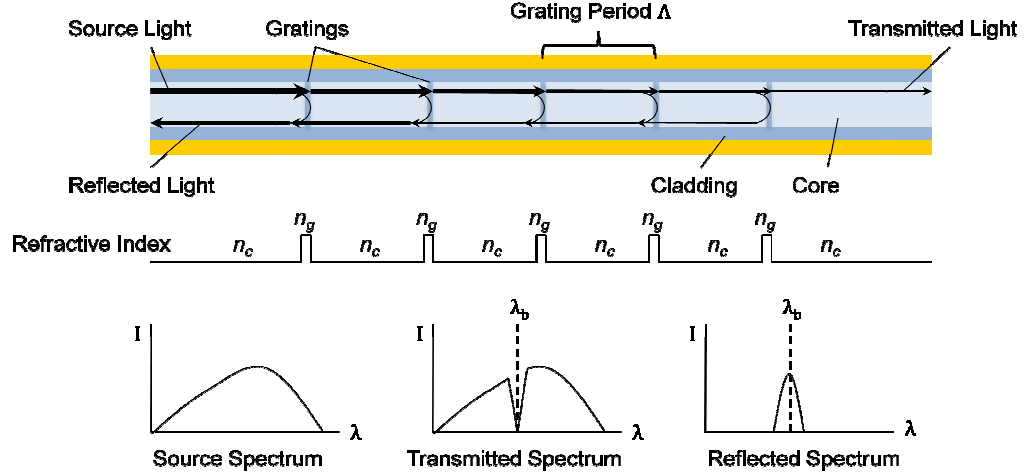


Figure 2-3 An illustration of how an FBG operates. An uniform FBG is shown.

Several types of common FBG structures are available, including the common Bragg reflector, blazed Bragg grating, and chirped Bragg gratings, etc. [2]. These different structures have distinct variations in their grating patterns, thus producing different reflection spectrum profiles. The common Bragg reflectors are most widely used and can be further categorized into sub-types, such as Type I, Type IIA, Type II, etc., which are determined during the grating inscription process [2]. The FBGs used in this dissertation are common, Type I FBGs, which have a highly periodic grating pattern and do not require special inscription methods or doping in the fiber core. A brief discussion of the theory describing the characteristics of FBGs follows.

For a Type 1 FBG, the change in the index of refraction, n , over the grating can be described by

$$\Delta n(z) = \overline{\Delta n}(z) \left[1 + s \cos \left(\frac{2\pi}{\Lambda} z + \varphi(z) \right) \right], \quad (2.3)$$

Where s is the fringe visibility related to the index change ($0 < s < 1$), $\varphi(z)$ is the phase variation compensation term for chirped gratings ($\varphi(z) = 0$ for uniform gratings), $\overline{\Delta n}(z)$

is the index change spatially averaged over the grating period, and z is the axial axis of the FBG [2]. Many different types of FBGs can be inscribed based on Equation (2.3). From coupled mode theory, the reflectivity per wavelength can be calculated. Consider a forward mode $R(z)$ and backward mode $S(z)$, then

$$\frac{dR(z)}{dz} = i\hat{\zeta}R(z) + i\kappa S(z), \quad (2.4)$$

$$\frac{dS(z)}{dz} = -i\hat{\zeta}S(z) - i\kappa R(z), \quad (2.5)$$

with

$$R(z) = A(z) \exp(2\pi i z n \left[\frac{1}{\lambda} - \frac{1}{\lambda_d} \right] - \frac{\varphi(z)}{2}), \quad (2.6)$$

$$S(z) = B(z) \exp(-2\pi i z n \left[\frac{1}{\lambda} - \frac{1}{\lambda_d} \right] + \frac{\varphi(z)}{2}), \quad (2.7)$$

$$\hat{\zeta} = 2\pi n \left[\frac{1}{\lambda} - \frac{1}{\lambda_d} \right] + \frac{2\pi}{\lambda} \overline{\Delta n(z)} - \frac{1}{2} \frac{d\varphi(z)}{dz}, \quad (2.8)$$

where $A(z)$ and $B(z)$ are the amplitudes of the forward and backward modes, respectively,

$\hat{\zeta}$ is the general self-coupling coefficient, $\kappa = \frac{\pi}{\lambda} \overline{s\Delta n(z)}$ is the coupling coefficient, and

$\lambda_d = 2n\Lambda$ is the designed peak reflection wavelength for gratings with weak index of

refraction change ($\delta n \rightarrow 0$) [2]. For uniform gratings, κ and $\hat{\zeta}$ are constants, thus

simplifying Equations (2.6) and (2.7) into first order ordinary differential equations. The

solutions, assuming $R(0) = 1$ and $S(L) = 0$ are expressed as

$$R(z) = R(0) \left[\cosh(\alpha z) + i \frac{\hat{\zeta}}{\alpha} \sinh(\alpha z) \right] + S(0) i \frac{\kappa}{\alpha} \sinh(\alpha z), \quad (2.9)$$

$$S(z) = S(0) \left[\cosh(\alpha z) - i \frac{\hat{\zeta}}{\alpha} \sinh(\alpha z) \right] - R(0) i \frac{\kappa}{\alpha} \sinh(\alpha z), \quad (2.10)$$

where

$$\alpha = \sqrt{\kappa^2 - \hat{\xi}^2} \quad (2.11)$$

From the above equations, and taking the amplitude $\rho = \frac{S(0)}{R(0)}$ the reflectivity can be demonstrated to be

$$P = \frac{\kappa^2 \sinh^2(\alpha L)}{\kappa^2 \cosh^2(\alpha L) - \hat{\xi}^2} \quad (2.12)$$

where L is the length of the grating. The bandwidth of the grating can be derived as

$$\frac{\Delta\lambda_0}{\lambda} = \frac{s\Delta n(z)}{n} \sqrt{1 + \frac{\lambda_d}{\Delta n(z)sL}} \quad (2.13)$$

where $\Delta\lambda_0$ is the bandwidth [2]. A reflectivity profile based on the above equations is shown in Figure 2-4.

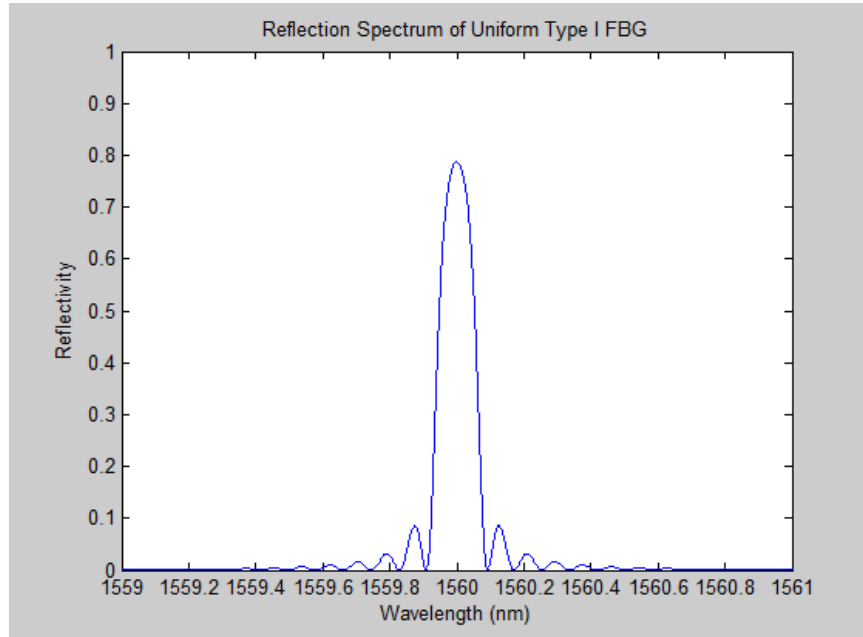


Figure 2-4. Reflection spectrum of a uniform Type I FBG.

From Equation (2.13), the bandwidth is defined as the spectral width between the zeros of the main peak reflectivity of the FBG. Equation (2.13) also states that the

bandwidth of the FBG is dominated by either the change in refractive index n or the grating length L . For weak gratings, where δn is small, the bandwidth is affected by the grating length. Conversely, for strong gratings, the bandwidth becomes more dependent on Δn . Physically, we may assume light cannot penetrate the entire length of a strong grating, thus reducing the reliance of the bandwidth on L for strong gratings.

As FBGs signals are wavelength encoded, they are practically immune to optical power fluctuations along the fiber optic. This property make FBGs an attractive choice for sensing, as the power loss associated with connections and bends in the optical fiber affect the FBG less than they do other optical sensors.

2.3.1. Strain and Temperature Sensing

The FBG sensors to be described in the later chapters of this dissertation will rely on the strain and temperature sensing capabilities of the FBG. Each of the coefficients in Equation (2.2) can be expanded to include the material properties of the FBG. Isolating the strain term in Equation (2.2), the change in wavelength can be expressed as

$$\Delta\lambda_B = \lambda_B(1 - p_e)\epsilon, \quad (2.14)$$

where

$$p_e = \frac{n_{eff}^2}{2}[p_{12} - \nu(p_{11} + p_{12})], \quad (2.15)$$

where p_e is the effective strain-optic constant, p_{11} and p_{12} are components of the strain-optics tensor, and ν is the poisson's ratio. Typically for a germanosilicate optical fiber ($p_{11} = 0.113$, $p_{12} = 0.252$, $\nu = 0.16$, $n_{eff} = 1.482$) at 1550 nm, the strain sensitivity 1.2

pm/ $\mu\epsilon$ [1]. However, when the FBG is coupled with a host material, a calibration test must be performed to ascertain the new stress-strain relationship of the FBG sensor.

Similarly, the coefficient of temperature can be expanded as

$$\Delta\lambda_B = \lambda_B(\alpha_\Lambda + \alpha_n)\Delta T, \quad (2.16)$$

where

$$\alpha_\Lambda = \left(\frac{1}{\Lambda}\right)\frac{\Delta\Lambda}{\Delta T}, \quad (2.17)$$

and

$$\alpha_n = \left(\frac{1}{n_{eff}}\right)\frac{\Delta n_{eff}}{\Delta T}, \quad (2.18)$$

where α_Λ and α_n are the thermal expansion coefficient of the fiber and the thermo-optic coefficient, respectively. For germanosilicate fibers at 1550 nm, the thermal sensitivity is about 13.7 pm/ $^\circ\text{C}$ [1].

2.3.2. Interrogation of FBGs

The previous sections explained that FBGs are modulators of wavelength, and measurements made by FBGs are coded in the form of wavelength shifts in the reflection spectrum of the FBG. These wavelength shifts must be demodulated into electronic form in order to be of use, thus forming the basis for the interrogation of FBG sensors. Interrogation methods essentially convert the wavelength signal of the FBG into measurable variations of optical intensity. The variations in the intensity are then converted to electronic signals. Practical interrogators should be sensitive to wavelength shifts across a large range while maintaining simplicity and low costs [2]. A large variety

of interrogation methods have been developed and described in the literature. Interrogation methods involving scanning optical filters are among the most widely used.

Some examples of scanning optical filters available for use in FBG interrogation include Fabry-Perot filters [3, 4], and acousto-optic tunable filters [5, 6, 7]. Even the FBGs can be used to form Bragg grating filters, as will be discussed in more detail in Chapter 6. In order to determine the wavelength from the sensing FBGs, the reflections of the sensing FBGs are passed into the scanning filter. The filter usually comprises of narrow band with a known center wavelength, and a controller sweeps, or “scans” the band through a selected range of wavelengths. The output of the filter is a convolution of the reflection spectrums of the sensing FBGs and the spectrum of the filter. Areas of the spectrum that return the highest magnitude output correlate to the wavelengths of the sensing FBGs and thus allow the demodulation of their wavelengths and any shifts thereof.

Another example of FBG interrogation involves the use of edge filters. Edge filters uniquely modulate the intensity of incoming light depending on the wavelength of the incoming light. The modulated intensity is compared to a reference in order to calculate the wavelength of the incoming light [8]. Other examples of FBG interrogations include interferometers [9], tunable lasers [10], spectrometers [11], etc., but their detailed discussion is beyond the scope of this dissertation.

Chapter 3 Contact Sensor for Ablation Catheter

3.1. Introduction

3.1.1. *Background*

The heart is incredibly durable, having to reliably sustain about 36 million pumping cycles during the lifespan of a healthy person [12]. However, various forms of heart disease compromise the functions of the heart and thus the longevity of the patient. One of the most common forms of heart disease is cardiac arrhythmia, in which the normal rhythm of the heart is disrupted by a period of disorganized contractions.

Atrial fibrillation (AF) is the most common type of arrhythmia, and is characterized by the disordered contractile activity of the atria (top chambers of the heart). In the United States, one fourth of adults over 40 years old will suffer from AF. Persons affected by AF are at a heightened risk of death, heart failure, and cardiac-related stroke [13].

A popular treatment for AF and cardiac arrhythmia in general is radiofrequency (RF) ablation. During RF ablation for AF, a catheter is passed venously into the heart, and is delivered into the left atrium through trans-septal puncture. Once contact has been made with defective tissue that caused AF, an electrode system integrated at the catheter tip transmits RF energy into the targeted tissue. Targeted cells warm up due to resistive heating and die as the temperature increases past 50 °C [14].

However, despite the usual success of RF ablation, several complications may occur, and some are life-threatening if not treated quickly. In about 2.4% of cardiac RF ablation procedures [15], the catheter is accidentally pushed through the heart wall due to

the application of excessive force. The resulting perforation in the heart wall allows the leakage of blood from inside the heart to the pericardial sac that surrounds the heart. Cardiac tamponade occurs when a sufficient amount of fluid accumulates in the pericardial sac to impair the functions of the heart. Usually, only a few minutes elapse between the start of perforation and when the life-threatening symptoms of cardiac tamponade manifest. Methods that allow detection of perforation or even a warning of impending perforation will be a valuable asset for cardiac RF ablation.

3.1.2. Literature

One of the most common techniques used to monitor cardiac RF ablation is fluoroscopy. Fluoroscopy is easily accessible and provides a visualization of catheter positions from many angles around the patient. However, fluoroscopy provides little information about the level of catheter-endocardial contact and at the same time increases the malignancy risk of both patient and physician [16-19]. Non-fluoroscopic techniques have been developed in the recent years that help to characterize the level of catheter-endocardial contact during RF ablation surgery.

Intracardiac echocardiography (ICE) was introduced to the RF ablation procedure to reduce the limitations of fluoroscopy. In ICE, an ultrasonic transducer is delivered through a 10F catheter (8F catheters are being made available) [16] to the various heart chambers. New developments (e.g., miniaturization) of this technology have lead to transesophageal echocardiography (TEE), where the probe is placed into esophagus to allow enhanced imaging of certain parts of the heart [20, 21]. The positioning of the ablation catheter within the heart can be projected onto a two dimensional plane, although fluoroscopy may be used in parallel to ensure the safe maneuver of the ablation catheter.

Non-imaging methods have also been developed to determine catheter-endocardial contact. Cao et al. investigated the use of electrical impedance between the tip electrode and the dispersive electrode to verify the contact state of the catheter [22, 23]. The electrical resistive difference between blood and endocardial tissue served as a basis that allowed the operator to gauge the insertion depth of the catheter and qualify how firmly the catheter was pressed against the heart wall [24]. Demos and Sharareh meanwhile assessed various parameters of the RF ablation operation via optical spectroscopy. Near-infrared (NIR) light was transmitted through a fiber at the tip of the catheter, and another fiber received the reflected light. The difference in the spectral characteristics of the transmitted and received light provided information such as contact level, lesion quality, char formation, etc [25].

Recently, a new type of ablation catheter (Tacticath) was developed to sense the contact force on the catheter tip. Three fiber Bragg gratings (FBGs) were integrated with a flexible unibody located near the catheter tip. As the unibody deformed, strains were transferred to the FBGs, which provided the signals needed to calculate the force vector [26, 27]. Later studies determined the force needed to perforate each chamber of an explanted porcine heart [28].

All of the above sensors and techniques enhanced the ability of the operator to ascertain the progress and quality of a cardiac RF ablation procedure. However, despite the ability to measure various parameters of the procedure (e.g., contact force, lesion formation) there has yet to be any data establishing how cardiac perforation can be reliably predicted. As seen from the current literature, the capability to predict cardiac perforation is still quite undeveloped. The following sections describe the design of new

FBG based sensor prototypes that (1) allows monitoring of the catheter-endocardial contact level, and (2) investigate signal characteristics that can predict or indicate transmural perforation of the left atrium in a living specimen.

3.2. Sensor Design

3.2.1. Sensor Construction

An FBG (15 mm) was encased inside a short (3.5 cm) stainless steel cylinder (1.587 mm OD \times 0.762 mm ID) (Figure 3-1). Two types of adhesives, epoxy (Devcon 5 min) and urethane (U1 urethane) were used separately to bond the FBG to the cylinder to test their respective strain transfer behavior. A superelastic tube (0.71 mm OD \times 0.51 mm ID) protected the rest of the fiber, while a thicker superelastic rod (0.6 mm diameter, 10 mm length) was bonded to the distal tip of the cylinder to act as a strain transfer member. The superelastic tube was inserted into the steel cylinder approximately 3 mm while the rod was inserted about 2 mm into the cylinder on the opposite side. The FBG was fully encased inside the cylinder, with the distal tip of the fiber less than 1 mm away from the superelastic rod. All components were then housed into an OFNR fiber optic jacket (2.6 mm OD \times 1.8 mm ID). As an important step to prevent blood infiltration to the components, the jacket was melted over the superelastic rod to create a blunt tip. Overall, the size and flexibility of the sensor were similar to an 8Fr ablation catheter.

Pressing of the catheter tip against a surface will produce a force vector that acts upon the superelastic rod. The force vector comprises of axial and lateral components, which correspondingly translate into compressive and tensile strains experienced by the FBG. Compressive and tensile strains correspond to negative and positive shifts in the Bragg wavelength, respectively. However, at this stage, a separation of the two forces has

not yet been implemented; in other words, the acquired data (see Results section) is the superposition of these strains. Thus, the more perpendicular the catheter is to the surface, the more the Bragg wavelength will tend to shift downwards due to the dominance of compressive forces. Buckling and high contact angles (θ in Figure 3-1 (A)) will induce lateral force components as well as encourage bending at the tube-cylinder junction and also at the cylinder itself, thus producing positive wavelength shifts during contact.

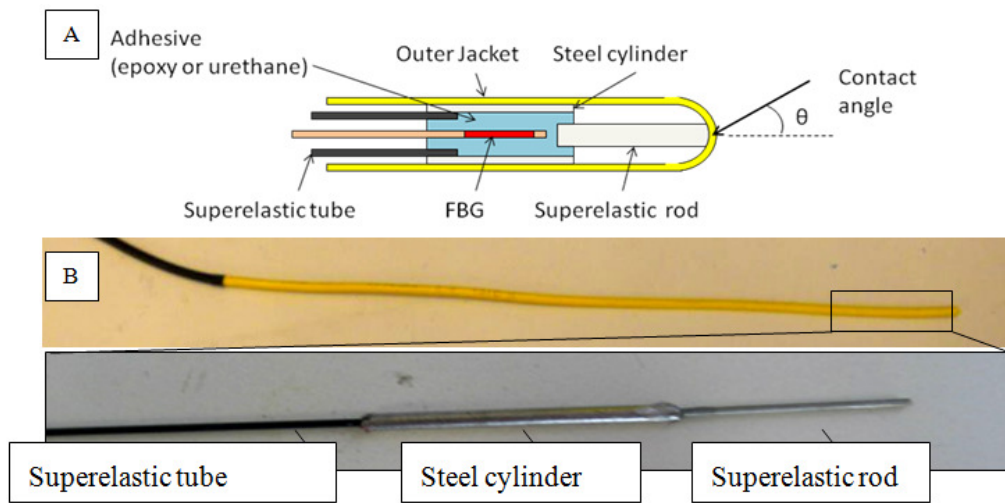


Figure 3-1. (A) Schematic of the sensor head. (B) Photos of the sensor exterior and interior.

The effect of the adhesive type on the readings of the sensors can be analyzed by the results from strain transfer studies performed by Ansari et al., Li et al., and Zhou et al. regarding FBGs embedded in host materials [29-31]. Their studies showed that a higher elastic modulus of the adhesive lead to a higher strain transfer rate along the bonded length between the FBG and the host material (i.e., the steel cylinder).

$$\alpha = 1 - \frac{\sinh\left(\frac{kL}{2}\right)}{\frac{kL}{2} \cosh\left(\frac{kL}{2}\right)}, \quad (3.1)$$

$$k^2 = \frac{1}{(1 + \mu_c) \frac{E_g}{E_c} r_g^2 \ln\left(\frac{r_m}{r_g}\right)}, \quad (3.2)$$

where α is the average strain transfer rate (percentage of strain transferred), L is the gauge length of the sensor, μ_c is the poisson's ratio of the adhesive, E_g is the elastic modulus of the fiber glass, E_c is the elastic modulus of the adhesive, r_g is the external radius of the fiber, and r_m is the external radius of the adhesive layer. Equations (3.1) and (3.2) are applicable under the following assumptions:

- 1) All materials are linear and elastic, while the host material only experiences axial forces,
- 2) The mechanical properties of the fiber core and cladding are similar,
- 3) The bonding between the fiber and the host material through the adhesive layer is perfect, without any debonding.

Table 3-1 are some estimates of the values based on manufacturer specifications (urethane adhesive was based on a similar product due to the lack of information from original manufacturer) [32, 33].

Table 3-1. Parameters used for estimation of average strain transfer.

Parameter	Value (Epoxy)	Value (Urethane)	Unit
Elastic Modulus of Fiber	7.2×10^{10}	7.2×10^{10}	Pa
Elastic Modulus of Adhesive	4.8×10^9	30×10^6	Pa
Poisson Ratio of Adhesive	0.25	0.3	
Outer Radius of Adhesive Layer	0.762	0.762	mm
Outer Radius of Fiber	62.5	62.5	μm
Length of Sensor	3.5	3.5	cm

Using the parameters in Table 3-1, the average strain transfer of the epoxy-based and the urethane-based sensor is 0.9755 and 0.6856, respectively. Thus, the stiffer epoxy adhesive allows the strain of the FBG match the strain of the steel cylinder more closely compared to the urethane adhesive. While the softer urethane has a lower strain transfer rate compared to the epoxy adhesive, the urethane adhesive, due to its flexibility will be more sensitive to axial loads as the superelastic rod will more easily push into the hollow of the steel cylinder and cause compression of the FBG. On the other hand, in accordance to Assumption 1, the strain transfer rates are valid only for the axial direction. Strain transfer behavior for lateral forces is not analyzed in detail here, but at the present it is assumed that the strain transfer rate for lateral loads has the same difference between the two adhesives as for axial loads.

3.3. Experimental Setup

3.3.1. Bench Tests

Prior to the animal tests, the sensors were used in the laboratory setting perforation tests. The first test utilized 10% ballistics gel (Permangel), and the second test utilized explanted porcine hearts. The Micron Optics sm420 interrogator was used for measurements.

3.3.2. Ballistics Gel

A 3.5 mm thick slab of ballistics gel was clamped and mounted onto a linear stage. Tension in the slab was maintained by fixing one side of the mount onto the stage and manually tensioning the other end. The constant adjustment to tension was required due to the relaxation properties of viscoelastic material (e.g., ballistics gel, biological soft tissue). The epoxy-based sensor was also mounted on the linear stage approximately 5 inches away from the gel slab, and was advanced approximately 0.5 inches/second toward the gel slab.

3.3.3. Porcine heart

The left atrium of an explanted porcine heart was punctured multiple times using both sensors. An incision was made through the outer surface of the left atrium to allow entry for the sensors. For this test, both the sensors and the heart were handled manually.

3.3.4. Animal Tests

Two live male sheep were used during the study. A thoracotomy was performed to gain direct access to the heart (Figure 3-2). The pericardial sac was partially excised to

reveal the epicardium of the left atrium. Small incisions were made on the left atrium to allow entry for sensors, and purse strings were tightened around the wound to reduce blood loss. For the initial part of the experiment, the catheter alternated between resting in the space of the chamber or perpendicularly pressing against the endocardial surface. Towards the end of the surgery, the catheters were pushed through the wall of the left atrium to induce mechanical perforation of the left atrial myocardium. Actively used sensors were grasped directly about six to nine cm from the tip, depending of the insertion depth of the sensor. Occasionally, forceps were used to grasp the left atrial epicardium and pulled back onto the sensor to facilitate perforation.

Data acquisition was accomplished through a PC laptop connected to an optical interrogator (Micron Optics, sm420 and sm130). A sampling frequency of 100 Hz (± 2 Hz for sm420) was used during the operation. Dictation from the surgeon allowed correlation of observed FBG signals with events occurring on the operating table.

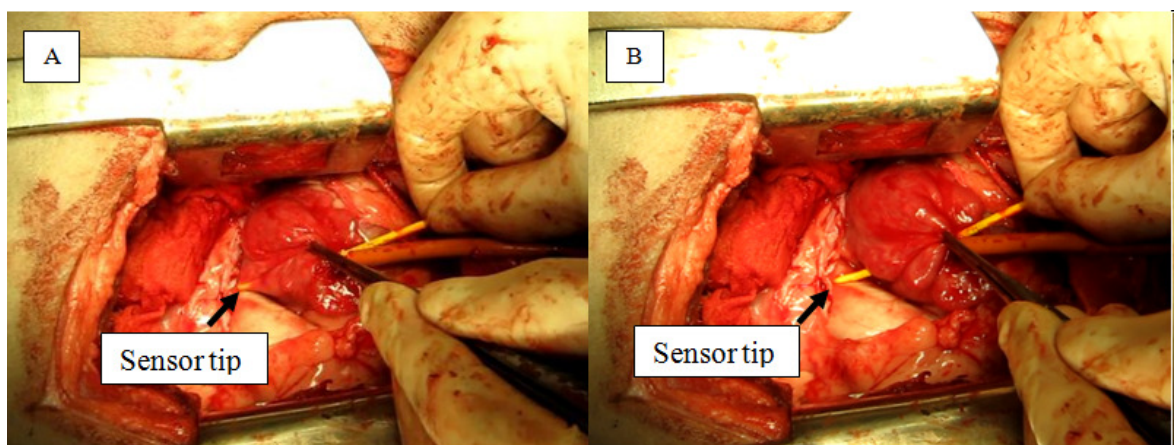


Figure 3-2. (A) Pushing of the sensor through the left atrial wall. The sensor tip is visible through thin tissue. (B) Completion of perforation. Forceps were used to assist this particular perforation.

3.4. Results

3.4.1. Ballistics Gel

Perforations, shown in Figure 3-3 and Figure 3-4, occurred over 6 s and 7 s, and had a wavelength shift of approximately 0.06 nm and 0.20 nm, respectively for the epoxy-based and urethane-based sensors. For both tests, as the sensor is pressed against the gel, a downward trend is observed, indicating the start of loading and the compression of the FBG. Perforation was marked by a rapid return to the resting wavelength, and was followed by an increase in wavelength corresponding to the manual extraction of the sensor from the gel slab.

Immediately prior to perforation using the epoxy-based sensor, a small signal reversal (0.008 nm over 1.5 s) can be seen. Most notably, this reversal occurred despite the continued advancement of the sensor against the gel slab. This reversal was not observed for the urethane-based sensor.

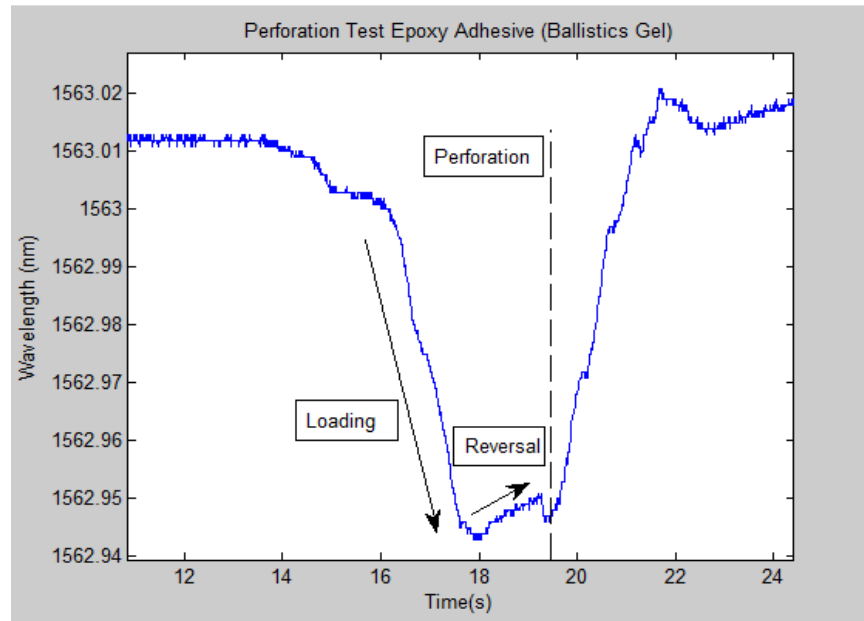


Figure 3-3. Perforation of ballistics gel slab using epoxy-based sensor.

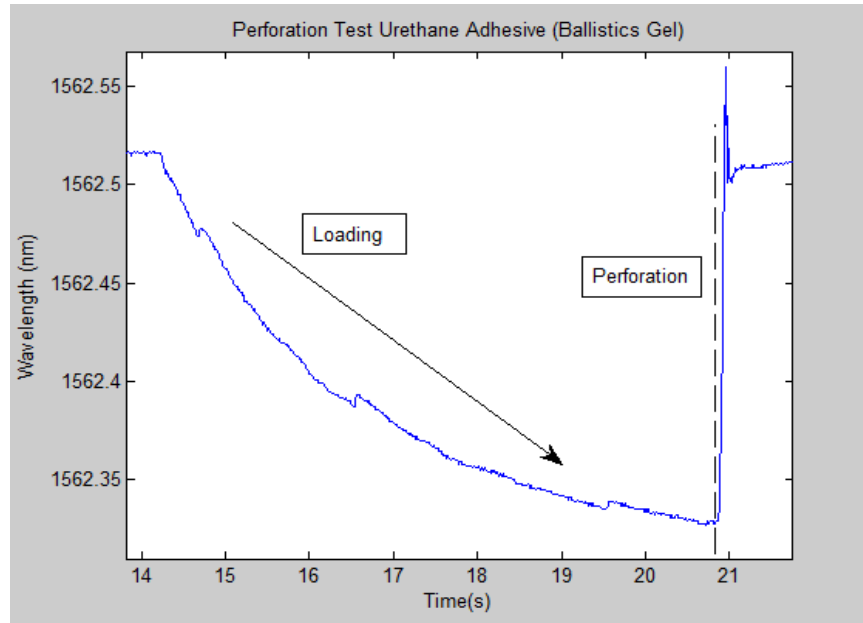


Figure 3-4. Perforation of ballistics gel slab using urethane-based sensor.

3.4.2. Porcine Heart

Perforation profiles obtained from porcine hearts were similar to the profiles obtained with the ballistics gel. Examples of perforations are shown in Figure 3-5 and Figure 3-6. The key difference is the appearance of less stable loading curves and buckling due to the transition from the use of mounts (i.e. with the ballistics gel test) and the use of manual navigation. During the test, the urethane-based sensor was noticeably more sensitive to vibrations caused by manual handling of the sensor. A brief reversal prior to perforation was observed (0.006 nm over 0.7 s) for the epoxy-based sensor.

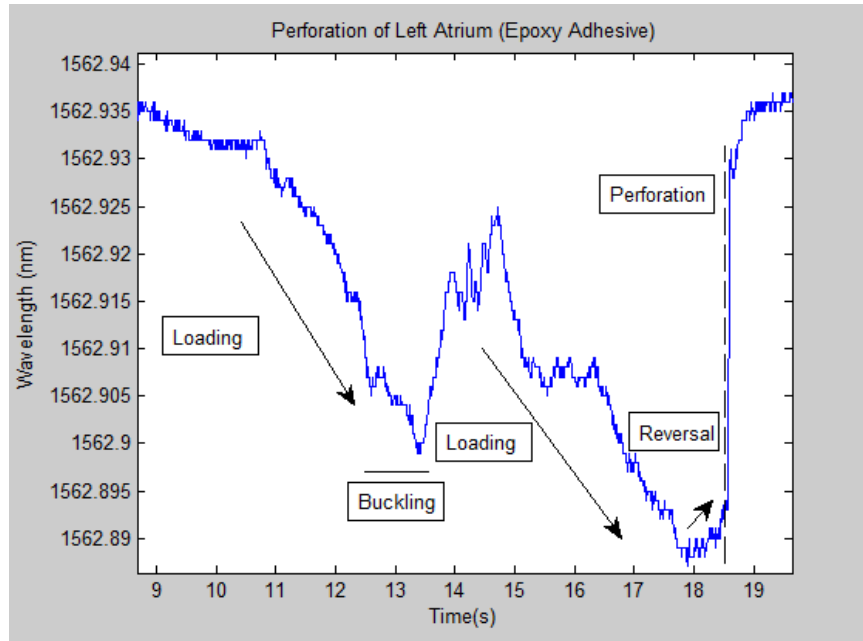


Figure 3-5. Perforation of LA using epoxy-based sensor (over 8 s, with 0.035 nm shift in wavelength).

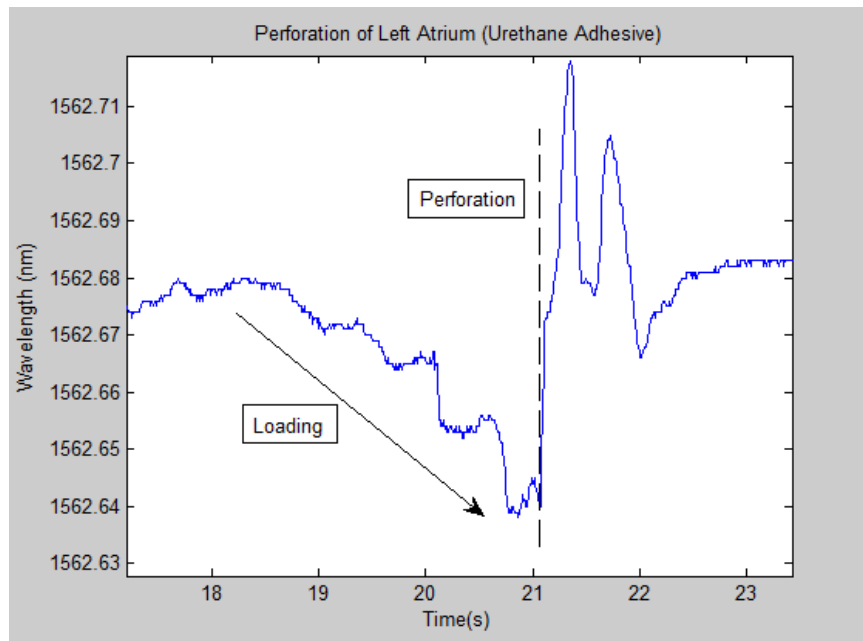


Figure 3-6. Perforation of LA using urethane-based sensor (over 3 s, with 0.04 nm shift in wavelength).

3.4.3. Animal Test

3.4.3.1. Contact

Each time the sensors were pressed firmly with the endocardial surface, clear patterns corresponding to myocardial contractions were observed. Once the sensor was retracted back into the chamber space, the patterns were diminished completely for the epoxy-based sensor and significantly diminished for the urethane-based sensor (Figure 3-7-Figure 3-11).

As seen in Figure 3-8, clear patterns in rhythm with heart beats were seen during firm contact of the epoxy-based sensor with the endocardial surface. Close observation of the contact interval show clear and defined heart-beat patterns during firm contact with the heart wall. Another example of contact with the heart wall is seen in Figure 3-9 and Figure 3-10. Although the signal was not completely flat prior to contact, the presence of the heart-beat induced pattern signified that contact was made. Similar behavior was observed for the urethane-based sensor, however, due to its higher sensitivity, contraction of the myocardium at the entry point produced weak periodic signals. Figure 3-11 shows contact monitoring using the urethane-based sensor while in the left ventricle. With stronger tissue, stronger contact can be made, which resulted in higher magnitude signals (0.3 nm in LV vs 0.08 nm in LA for the urethane-based sensor).

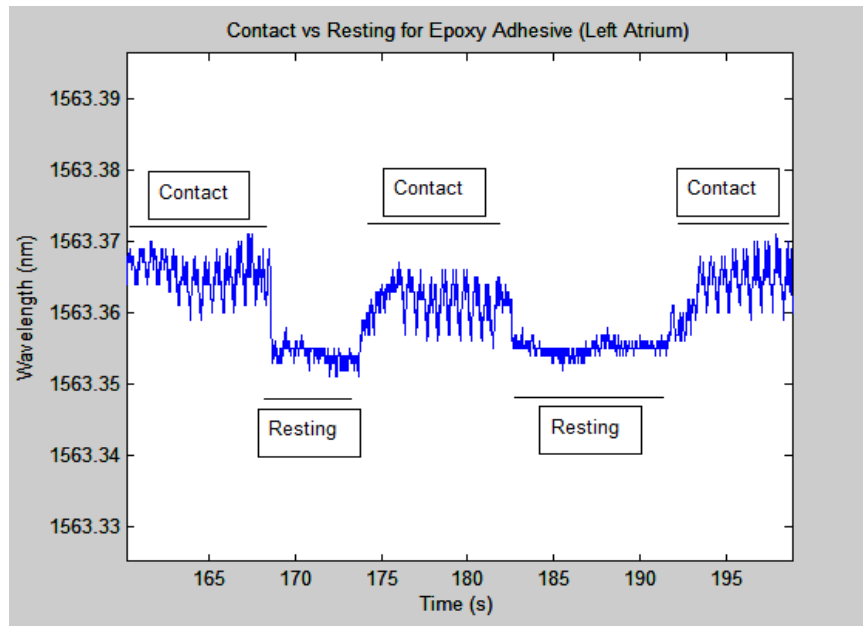


Figure 3-7 Contact of epoxy-based sensor with left atrium.

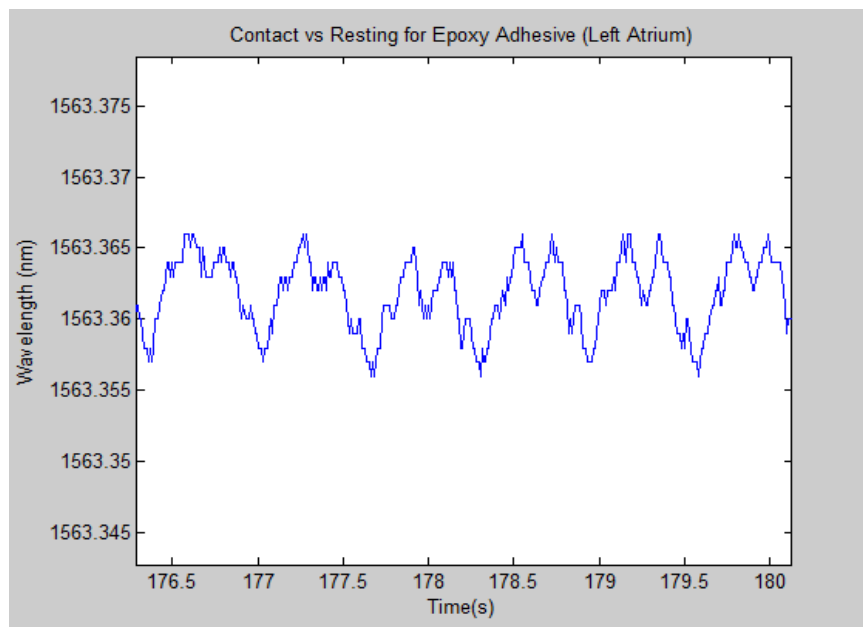


Figure 3-8. Zoom in of signals during contact.

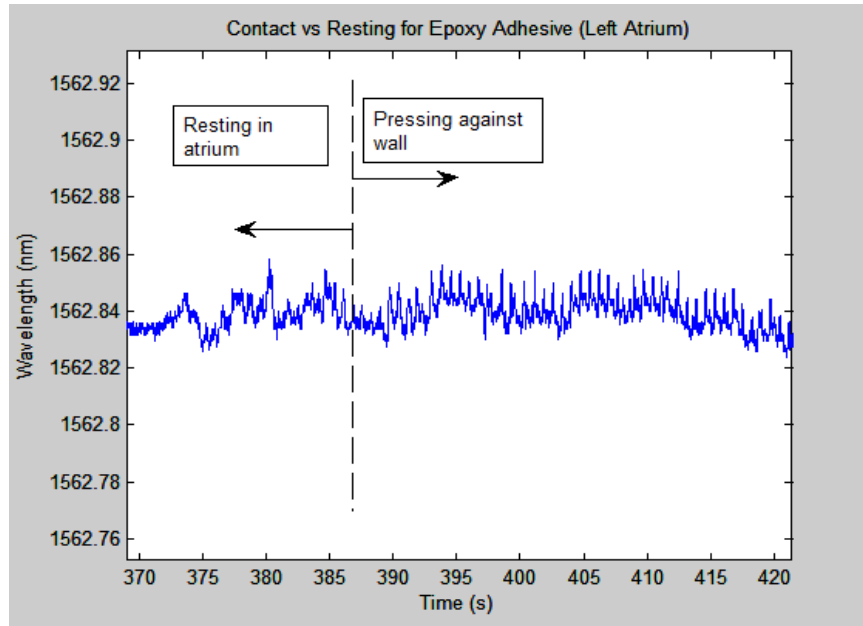


Figure 3-9 Contrast between resting and contact for epoxy-based sensor.

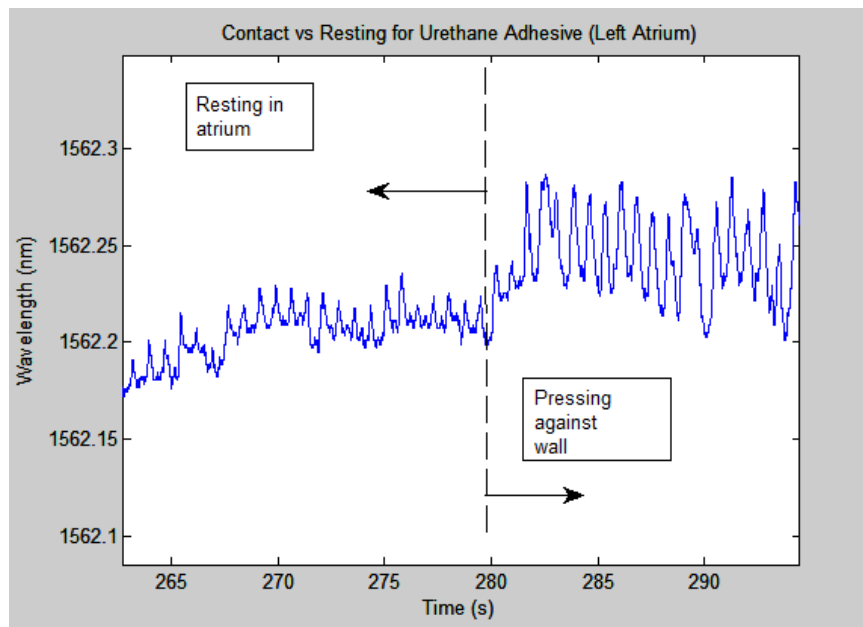


Figure 3-10. Contrast between resting and contact for urethane-based sensor.

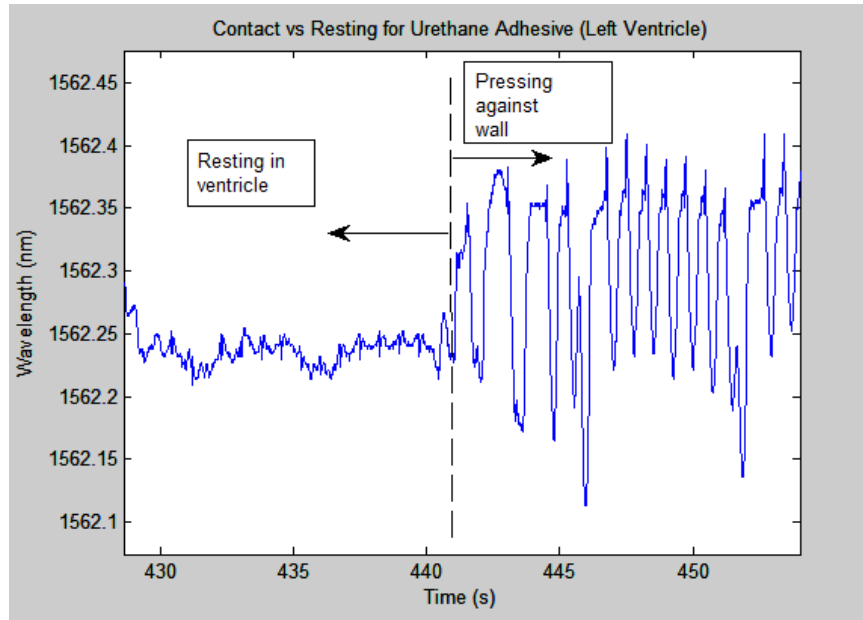


Figure 3-11. Resting and Contact inside the left ventricle for urethane-based sensor.

Generally, it was observed for the epoxy-based sensor that regular sinusoid signal patterns (contraction frequency slightly higher than 1 Hz) with an amplitude greater than or equal to 0.01 nm was sufficient to indicate firm contact with the heart wall. For the urethane sensor, the threshold was greater due to higher sensitivity, requiring amplitudes greater than 0.05 nm to ensure reasonable confidence that firm contact has been made. The higher sensitivity of the urethane-based sensor allowed whole-body vibrations and operator handling of the sensor to be mixed with the signal; and sometimes whole-body vibrations were in synchronization with contraction rhythms, thus requiring a higher contact detection threshold. Each contact event during the animal test involved firm pressure between the catheter tip and the endocardial surface, and was described often-times by the operator as being “near perforation.”

3.4.3.2. *Perforation*

Transmural perforation of the left atrium using the catheters was generally characterized by a distinct loading phase (greater than 0.07 nm change for the epoxy-based sensors and between 0.06 nm and 0.15 nm for the urethane-based sensor) and a rapid return to prior wavelength levels. The type of adhesive utilized for the FBG-steel cylinder bond led to different characteristics of the perforation signal profile. Myocardial contractions were more apparent during the loading process when the epoxy-based sensor was used.

Figure 3-12 shows the transmural perforation of the left atrial wall using the epoxy-based sensor. Note the negative loading phase and the slight reversal in signal immediately before perforation, similar to the perforation test with the explanted porcine heart. On the other hand, in Figure 3-13 is another perforation event using the epoxy-based sensor, albeit with a positive loading phase. Figure 3-14 shows an example of a quick perforation (over 2.5 s) using the epoxy-based sensor. The presence of a reversal may be mixed and distorted by heartbeat signals. Figure 3-15 and Figure 3-16 show the perforation profile of the urethane-based sensor. Similar to the epoxy-based sensors, perforation is characterized by a sudden drop preceded by a loading phase.

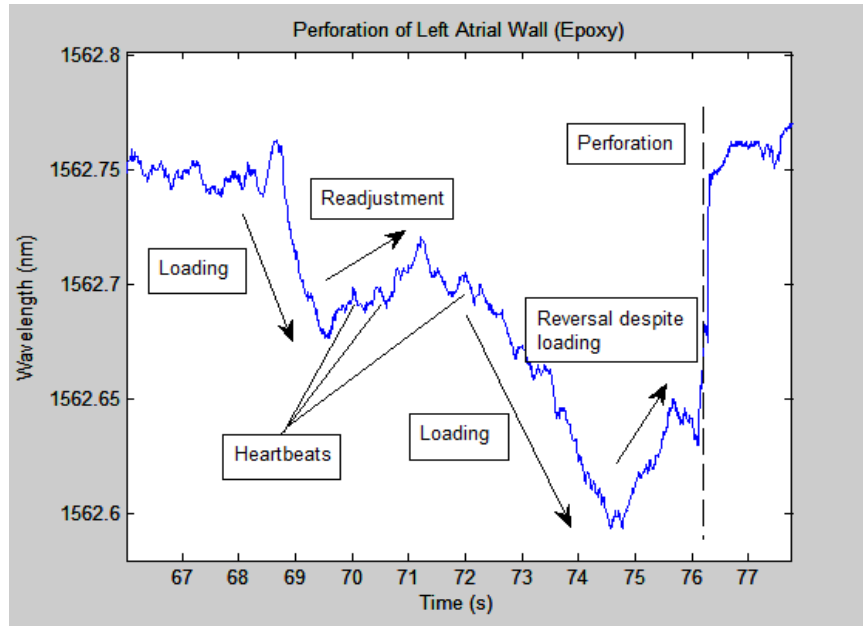


Figure 3-12. Perforation of left atrium using epoxy-based sensor.

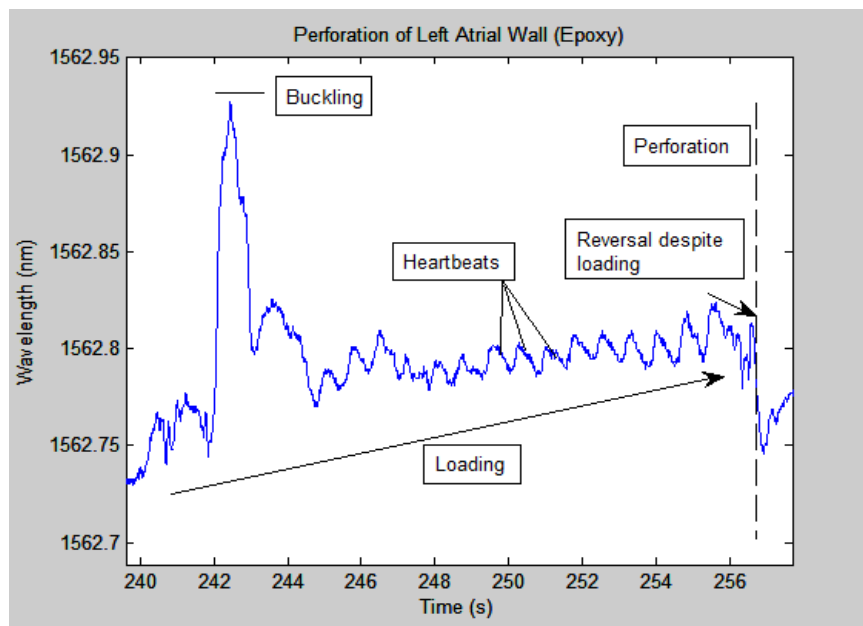


Figure 3-13. Perforation of left atrium using epoxy-based sensor with positive loading curve.

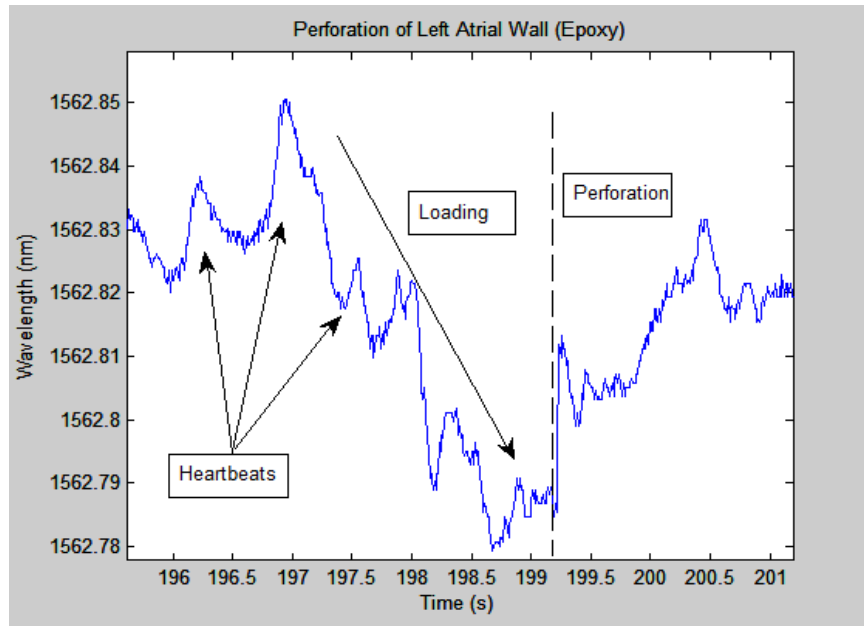


Figure 3-14 Perforation of left atrium using epoxy-based sensor.

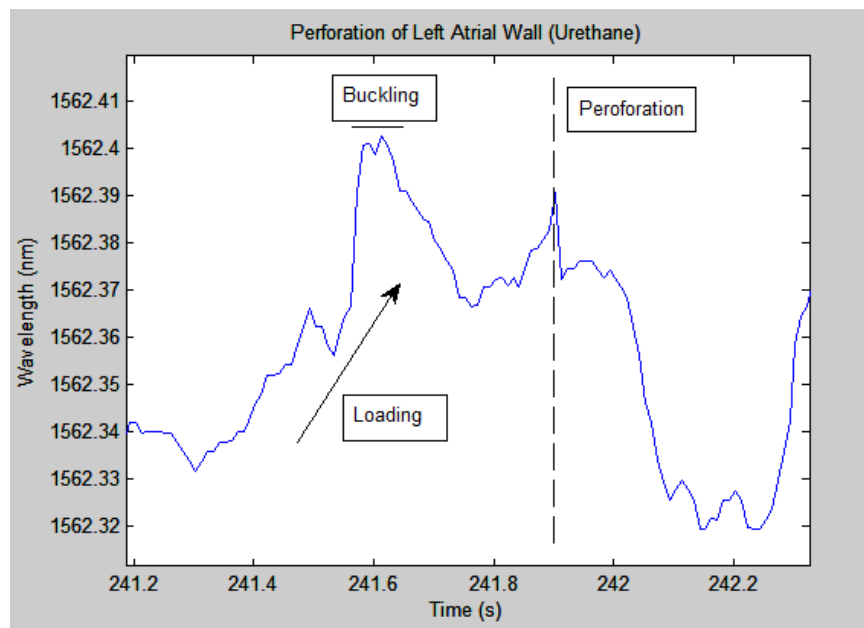


Figure 3-15. Perforation of left atrium using urethane-based sensor.

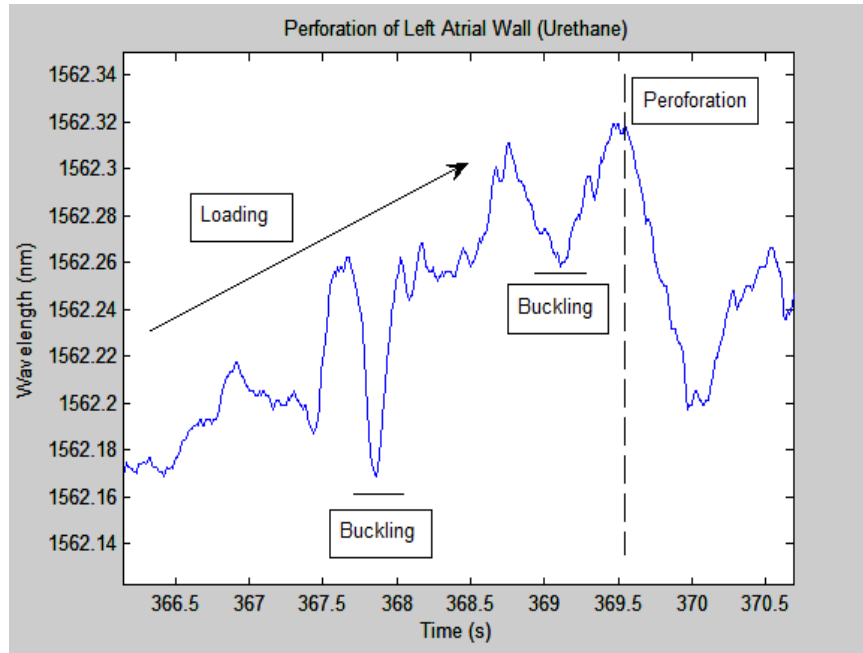


Figure 3-16. Perforation of left atrium using urethane-based sensor.

During two perforation events using the epoxy-based sensor, a reversal of the loading phase (approximately 25% and 12% of loading phase time in Figure 3-12 and Figure 3-13, respectively) occurred immediately before the onset of perforation. The loading phase spanned 8 seconds for Figure 3-12 and 16 s for Figure 3-13, while in Figure 3-14 the loading phase lasted about 2.5 s. Note that similar reversals were observed during *in vitro* lab bench testing performed prior to the animal tests. Urethane based sensors produced smoother perforation profiles in which heart beats were not readily seen compared to the rest of the signals. The signal drop-off during perforation was also more gradual compared to the epoxy-based sensor. Several peaks occurring during the loading phase of the urethane-based sensor correlated to the slight buckling of the catheter at the junction between the steel cylinder and the protective superelastic tube.

3.5.Discussion

3.5.1. Ballistics Gel

The perforation tests of a ballistics gel slab were the most controlled of all the proceeding tests in that the perforation target did not have significant movement, and the sensor advanced steadily towards slab while securely mounted on the linear stage. The main differences between the readings of both sensor types are the magnitude of response (e.g., 0.06 nm and 0.20 nm for the shown perforations) and the appearance of a signal reversal prior to perforation. Such differences are attributed to the different strain transfer characteristics provided by the different adhesives, as described in section 3.2. The occurrence of the reversal was accompanied by a visually observable thinning of the gel slab at the point of contact prior to perforation. The thinning process may explain why the sensor readings indicated a slight relaxation even though pressure continually increased. The reversal was visible with the epoxy-based sensors while the urethane-based sensor had difficulty capturing it. It is likely that the lowered strain transfer coupled with flexibility of the adhesive in the urethane-based sensor had masked the reversal.

3.5.2. Porcine Heart

Results from the perforation of the porcine heart had fundamental similarities with the results obtained from the ballistics gel test. Each perforation was preceded by a loading phase and followed by a rapid return to the baseline wavelength. Furthermore, for the same reasons seen in the ballistics gel test, a small reversal was observed for the epoxy-based sensor but not for the urethane-based sensor. Differences from the previous

test include disturbances in the sensor readings due to the manual handling of the sensors and the heart. The lower stiffness of the urethane allowed the movements of the entire fiber optic to affect the strain observed by the FBG and in effect created additional shear stresses on the FBG (i.e., in addition to the strain transferred from the steel cylinder). On the other hand, the more rigid bonding in the epoxy-based sensor in effect shielded the movements of the fiber optic cable.

3.5.3. Animal Test

As seen from the experimental data, the sensors were able to detect contact with the endocardial surface and were also able to provide a unique signal pattern corresponding to transmural perforation of the left atrium. Similar to the previous ballistics gel and porcine heart tests, the sensing ability of the sensors was greatly impacted by the type of adhesive used for bonding the FBG and the superelastic rod to the steel cylinder. Compared to urethane-based catheters, epoxy-based catheters were less sensitive to external input. This insensitivity filters out many disturbances, such as whole catheter vibrations, thus making the perforation event clearer than with urethane-based catheters. A feature unique to the animal tests is the presence of body heat and the rhythmic contractions of the heart, each superimposing more signal patterns in the measurements of the sensors.

3.5.3.1. Contact

As seen in Figure 3-7, myocardial contractions appeared as rhythmic peaks in the signal whenever firm contact was maintained and were greatly diminished when contact was absent. These peaks can serve as a sufficient indicator that catheter-endocardial

contact has been initiated. On the other hand, less information is available regarding the level of contact. Naturally, higher contact forces yield stronger signals, as seen when the catheter was passed into the left ventricle. However, while stronger tissue can withstand higher contact forces, weaker, thinner tissue such as those in the left atrium should not be subjected to similar levels of contact. Thus as a safety measure, the operator should be cautious not to push much further when the sensor signals present such peaks in the signal at or above the threshold levels (0.1 nm and 0.5 nm for epoxy-based and urethane-based catheters, respectively). Conversely, as these contact waveforms indicate firm catheter-endocardial contact, the operator should seek for their appearance before deciding on whether to proceed with ablation.

3.5.3.2. Perforation

Each perforation conducted during the study was characterized by a loading phase and a sudden, rapid return to prior wavelengths at the time of perforation. Negative loading phases correspond to axial loading of the catheter while positive loading phases correspond to the presence of lateral forces, or shearing at the catheter tip. Thus for the current sensor design, a positive wavelength change after reaching thermal equilibrium suggests that the catheter tip may not be fully perpendicular to the endocardial surface (e.g., Figure 3-13, Figure 3-15, Figure 3-16, during loading). Of note in Figure 3-12 and Figure 3-13 is the brief reversal of signal wavelength immediately prior to perforation despite continual pressure exerted by the operator, as seen in the previous tests with the ballistics gel and the porcine heart. Applying the observation seen in the ballistics gel test, an explanation of the reversal is that when the contact level started to reach perforation levels, the targeted tissue began to weaken and thin, temporarily relieving the pressure

between the catheter tip and the atrial wall. The length of the reversal was more prolonged and apparent when the perforation was carried out more slowly; in fact, as seen in Figure 3-14 the reversal may be absent when perforation was carried out quickly (2.5 s in Figure 3-14 compared to greater than 8 seconds in Figure 3-12 and Figure 3-13). Short perforation times prevented correlation of perforation speed with the observability of a reversal signal. However, sensitivity-induced competition with secondary signals such as operator handling readily reduced the prominence and clarity of the perforation signal. Therefore, it may be concluded that stiffer adhesives such as epoxy will allow exactly the right strain transfer to isolate signals unique to perforation. On the other hand, one should realize that perforations performed in this study were carried out intentionally, and during actual ablation procedures, a loading phase may not be as apparent to the operator. For load-sensing enabled RF ablation catheters, Figure 3-13 may be more representative of more realistic situations in which the magnitude of the baseline and the heart beat induced peaks slowly magnified until a sudden wavelength drop-off occurred. Thus, during RF ablation, the operator should check for alternate signs of perforation whenever a wavelength drop-off is observed after steady increases in signal waveform magnitudes.

Perforation results from this study agree with the results presented by Shah et al. [28], with both studies showing a characteristic loading phase followed by a sharp drop in contact force coinciding with perforation (seen in the current study as a quick shift in Bragg wavelength to pre-loading levels). A contact force threshold (100g) was recommended by Shah et al. to minimize the chances of perforation [28]. On the other

hand, the brief reversal as seen in Figure 3-12 and Figure 3-13 may act as an additional warning signal for operators of impending perforation.

The data acquired from this study lays the foundation for further improvements in sensor designs in subsequent studies. During the perforations shown in Figure 3-13, Figure 3-15, and Figure 3-16, the buckling of the sensor between the cylinder and the protective superelastic tube produced large peaks in the signal. Later designs will reinforce this junction to reduce the chance of buckling during loading. Furthermore, the thicknesses of the cylinders housing the FBGs were thin and thus susceptible to substantial bending stresses. Increasing the thickness will reduce the effect of bending stresses, but will impose obstacles in other aspects of the sensor, such as the size; thus a stiffer type of material may be used to lower this effect while maintaining a small size.

3.5.3.3. Effects of Temperature

As indicated by Equation (3.1), changes in temperature correlates to shifts in the Bragg wavelength but does not affect sensitivity to mechanical strain. Throughout the study, temperature changes occurred mainly from the movement of the sensor into and out of the cardiac chambers. Insertion of the sensor into the heart produced an upward shift of approximately 0.4 nm in the Bragg wavelength. Roughly 30 seconds were required for the sensor to reach thermal equilibrium once inside the heart (hence no more temperature-induced wavelength shifts). Extractions of the sensor lead to the recovery of the wavelength shift to original, pre-insertion levels.

Although temperature did not have an effect on the current results after the sensor reached thermal equilibrium within cardiac chambers, a compensating mechanism will be

necessary if the sensor is to be calibrated for force. A stress-relieved FBG sensor placed close to the sensing area will be able to measure temperature-induced wavelength shifts while at the same time be isolated from contact strains (an example of this mechanism is shown in [34], and will be further discussed in Chapter 4).

3.6. Conclusions

Sensors fabricated in similar form as an ablation catheter were able to allow monitoring of catheter-endocardial contact levels and investigate any signal behavior that helps in predicting or indicating the occurrence of transmural perforation of the left atrium. Multiple, periodic peaks were seen in the signal when contact with a living endocardial surface was made and quickly diminished in the absence of contact, thus establishing a condition indicating the presence of contact. Furthermore, perforation was identifiable by a baseline-shifting loading phase followed by a rapid return to prior wavelength levels.

For epoxy-based sensors, a short signal reversal was observed prior to the moment of perforation, and it is recommended that stiff adhesives be used when investigating the characteristics of perforation. Knowledge of these signal characteristics will help future ablation procedures regarding the application of adequate pressure and also for reducing perforation incidences.

Chapter 4 A Fiber Bragg Grating Sensor for Detection of Liquid Moisture in Concrete Structures

4.1. Introduction

Concrete structures, which help form the basic infrastructure of modern society, must be designed to withstand a range of harsh environments. The longer the concrete structure has been in service, the higher the chance that the structure has sustained damage. Many times, damage is manifested in the form of cracks, and some make their way to the surface, where it can be seen by humans. However, damage propagating within the structure, such as near or at the reinforcing rebars, may not be as evident. Such internal damage is often attributed to the invasion of pure and/or ionized water into the structure, which may cause the corrosion of the reinforcing system of the concrete structure. Water may permeate through concrete in the form of humidity, or may even flow as moisture-liquid through concrete by traveling along conduits formed by cracks [35, 36]. A sensor developed to detect the ingress of moisture and liquid water will be useful for a more complete structural health monitoring of any concrete construction.

4.1.1. Literature

4.1.1.1. Conventional Water sensors

Many sensor modalities have been developed to sense the presence of water in its different phases. A majority of such sensors were geared to measure humidity (water vapor) levels. Some examples of such sensors include mechanical hygrometers, animal hairs, psychrometers, etc. [37, 40]. These sensors have had broad applications across agriculture, weather prediction, medicine, etc. [39].

The introduction of electronics has allowed the miniaturization of humidity sensors and thus is more versatile in terms of deployment. Partly due to this increase in

versatility, most of the currently used humidity sensors are electronically based [41]. Electronic humidity sensors measure changes in electron transduction due to air humidity. Generally, these sensors can be categorized into capacitative, resistive, and gravimetric sensors [41-46].

4.1.1.2. Fiber Optic Water sensors

While the integration of electronic technologies allowed the miniaturization of humidity sensors, the development of fiber optics (FO) has opened new doors in regards to the precision, operation, low cost, and networking. FO-based sensors also have a unique resistance to water-related damage, in contrast to most commercially available electronic sensors, which may be vulnerable to circuit shorting due to contact with liquid moisture. A wide variety of fiber optical humidity sensors have already been produced, and can be divided broadly into spectroscopic, fluorescent, interferometric, and in-fiber grating sensors.

Spectroscopic FO sensors generally measure changes in the spectroscopic absorption of a humidity-sensitive chemical (e.g., cobalt chloride, Rhodamine B, crystal violet, etc.) arranged on a thin film [47-51]. Spectroscopic FO sensors can have a wide humidity range and fast response times, such as one presented by Otsuki et. al, which had a range between 0 to 95% relative humidity and respond within 2 minutes [52]. Fluorescent based FO sensors measure the fluorescence of certain dyes due to photonic excitation. Posch and Wolfbeis detailed the workings of a fiber optic fluorosensor in which the magnitude of the fluorescence emitted by a dye (e.g., perylenedibutryate) was modulated by the level of humidity [53]. Another mode of FO humidity sensing is to take advantage of materials that change refractive index based on changes in humidity. For

example plastic fiber optic coated may be coated with hydroxyethylcellulose, which swells and changes refractive index in the presence of humidity [38]. Interferometric FO sensors measure the phase difference of two light waves from the same source is compared after reflection from a mirror. Some known FO humidity sensors use Mach-Zehnder, Sagnac, or Fabry-Perot interferometric configurations [55, 56, 57].

4.1.1.3. In-Fiber Grating Sensors

In-fiber grating sensors include long period gratings (LPG) and fiber Bragg gratings (FBG). Both the LPG and the FBG possess a section of optical fiber core inscribed with periodic perturbations (grating) of refractive index (see Chapter 2). The difference between the LPG and FBG is the length of the grating (LPG: 100 μm to 1 mm, FBG: $<1 \mu\text{m}$) [1]. Signals from LPGs are seen as shifts in attenuation bands, while FBGs produce signal in the form of wavelength shifts of the backward propagating mode. Changes in the cladding of an LPG sensor lead to changes in its transmission spectrum. This property has been used to develop several humidity and liquid-moisture LPG sensors [59-61].

While LPGs can readily be used as a direct sensor for chemical/humidity changes due to the strong effects of the environment on the cladding-core mode coupling of the LPG, FBGs are less sensitive to chemical stimulation and are better suited for measuring physical parameters such as strain, temperature, and pressure [37]. In order to measure parameters such as humidity, a mechanism must be used to translate humidity into one of the aforementioned physical parameters. In the literature, this translation was accomplished using humidity sensitive polymers. In one sensor design by Kunzer et al., the polymer was coated over the FBG to measure the moisture content of soil. Swelling

of the polymer due to absorption of moisture induced a longitudinal strain in the FBG, thus shifting the wavelength and signaling the level of humidity. The sensor had a linear response between 0 to 100% humidity with a response time limited by the swelling rate of the polymer [39].

In a similar study by Yeo et al. an FBG was coated with polyimide, for which moisture-induced swelling produced tension of the FBG. The study indicated that the thickness (thicknesses between 10 to 42 μm were tested) of the polymer coating directly correlated to the response times [35, 36, 62]. Other FBG-based humidity sensors found in literature had a similar construction (polymer-induced straining of the FBG), with some modified for sensing salinity or other analytes [63-65]. It is conceivable that the above LPG and FBG sensors can detect the presence of liquid moisture (with signals saturating at 100% relative humidity representing the presence of liquid moisture).

The sensor described in the following sections bears some similarity to the aforementioned FBG sensors in that a water-swellaable polymer was used to induce strain on the FBG. However, instead of a thin coating around the FBG, which require a complicated bonding process, a separate but adjacent bead of superabsorbent polymer (to be described in detail in the next section) was used to absorb liquid moisture. Volumetric expansion of the bead translated to a bending strain of the FBG, thus shifting the reflected wavelength. This sensor detects the presence liquid moisture instead of measuring humidity levels, and lays a foundation for the development of a sensor that can measure the amount of liquid moisture.

4.1.1.4. Sodium Polyacrylate

A certain class of polymers, called superabsorbent polymer (SAP) hydrogels, can absorb water several hundred times its own mass. Originally developed by the US Department of Agriculture to increase the water holding capacity of soils [66], SAPs have been extended for uses in medicine, cosmetics, home improvement, hygiene products, etc. SAPs can be seen as a network of crosslinked polymers containing ionic functional groups (usually carboxylate anions and sodium cations). The ionic groups produce a driving force that encourages water to be absorbed and retained within the polymer network. Together with elastic forces and polymer-solvent interactions, the ionic gradient comprises the osmotic pressure of the SAP [67, 68]. The SAP behaves so that the osmotic pressure is zero [67]. A widely used low cost formula of SAP is Sodium Polyacrylate $(C_3H_3NaO_2)_n$. This particular SAP relies on the $-COONa$ functional groups to form an ionic potential that encourages the entry of water molecules into the polymer network. As more water enters the network, the functional groups become the less ionic $-COOH$ group, thus slowing down the influx of water. The swelling characteristics with respect to different environmental variables (e.g., temperature, electrolyte concentration, pressure, etc) have been studied in detail by several research groups [67, 69, 70].

The following sections describe an FBG based liquid moisture sensor that utilizes the expanding properties of SAPs to detect the presence of liquid moisture. Unlike the water sensors described in the literature, the proposed sensor will not require special coating techniques, and instead will rely on a separate package placed adjacent to the FBG. Two configurations were tested in order to examine the effects of different designs.

4.2. Sensor Design

4.2.1. Housing and transduction mechanism

A steel sensor housing was designed (SolidWorks) to accommodate and protect both the FBG and the sodium polyacrylate spheres (Figure 4-1). Small conduits at the ends of the sensor housing aligned the FBG through the longitudinal center of the housing. Parts of the fiber cable passing through the conduits can be fastened to allow adequate strain transfer between the volumetric expansion of the polymer sphere and the FBG. The FBG fiber was protected by a thin furcation tube. In order to minimize the displacement of the polymer sphere and expand the area of contact with the FBG, the polymer sphere was encased within a silicon-sealed, thin-walled package made of water-permeable material (e.g., hemp from commercially available tea packets).

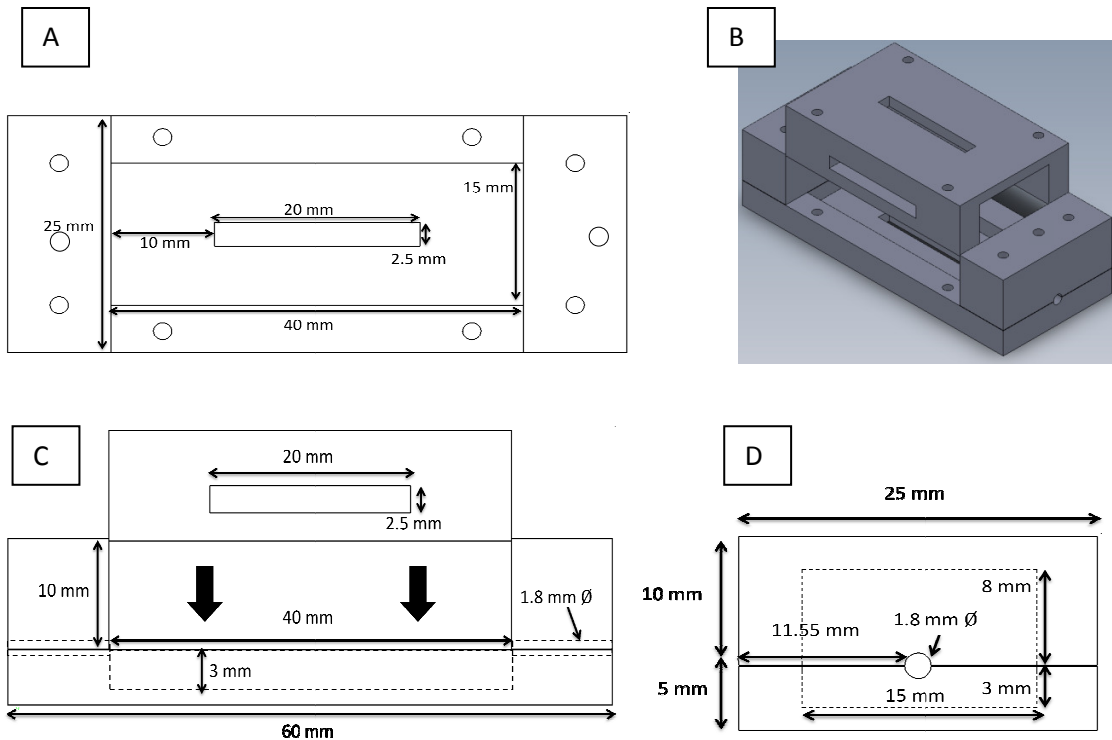


Figure 4-1. (A) Top-down view of the housing without the middle cover. (B) Overall perspective of the water sensor housing. (C) Side view of the sensor housing. (D) Axial view of the sensor housing.

Rectangular windows along the longitudinal sides of the housing allow water to enter the sensing area. Liquid water entering the windows will reach past the package via osmosis and be absorbed by the polymer sphere. The volumetric expansion of the polymer sphere due to water absorption directly tensions the FBG above itself. In order to tension the FBG and thus allow higher sensitivity, threaded holes above the conduits allow the entry of a screw that can be used to fix the FBG. In order avoid crushing and damaging the fiber optic cable, the screw was tightened only until the intensity of the FBG reflection began to drop.

It was anticipated that the presence of the FBG may induce lateral displacement the polymer during the swelling process. Thus, the following two configurations were tested: Free and Rail. The Free configuration is close to Figure 4-2 (Left), while the Rail configuration includes two thin superelastic wires (0.1 mm diameter) that run along the length of the housing with approximately 2 mm offset from the central axis (Figure 4-2 Right).

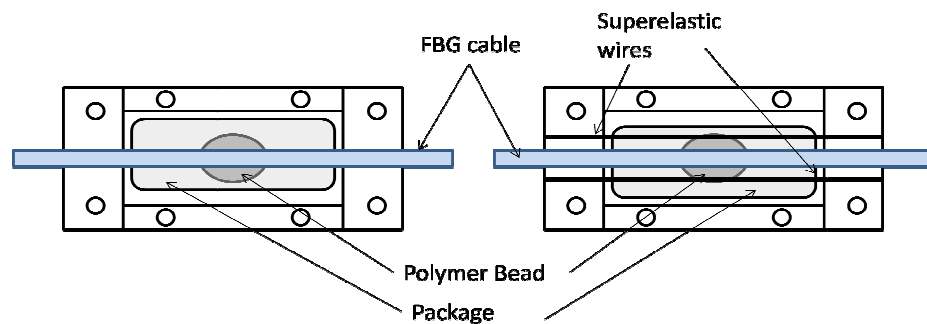


Figure 4-2. Two different sensor configurations were used. (left) Free configuration. (right) Rail configuration – wires were used to restrict lateral movement of the polymer bead.

4.3. Model/Characterization

The swelling characteristics of SAPs were of interest of researchers and theories have been developed to describe the swelling properties of the polymers.

4.3.1. Swelling Model

Several mathematical models of SAP swelling exist in the literature [59, 72-74], each pertaining to different variables that contribute to the osmotic pressure of the SAP. For the purposes of this experiment, we will only regard models relating diffusion to swelling (we assume electrolyte concentrations change negligibly during testing). Diffusion models are based on Fick's second law of diffusion, of which the one dimensional version is shown in Equation (4.1),

$$\frac{\partial c}{\partial t} = D \frac{\partial^2 c}{\partial x^2}, \quad (4.1)$$

where c is the concentration of the solute, and D is the diffusion coefficient. If convection is considered, we add an additional term to form an overall expression

$$\frac{\partial c}{\partial t} = D \frac{\partial^2 c}{\partial x^2} - \frac{\partial}{\partial x} c v, \quad (4.2)$$

where v is the convective velocity of the front of the solvent moving through the polymer. Through Fourier transform methods [71], the solution to Equation (4.2) can take the closed form of

$$c(x, t) = \frac{1}{2} \left[1 + \operatorname{erf} \left(\frac{vt - x}{2\sqrt{Dt}} \right) \right], vt > x, \quad (4.3)$$

$$c(x,t) = \operatorname{erfc}\left(\frac{vt-x}{2\sqrt{Dt}}\right), vt \leq x \quad (4.4)$$

According Porter et al., these solutions may be integrated together to form an expression of total swelling, $s(t)$ as a function of time, as shown in Equation (4.4) [71],

$$s(t) = \int_0^{vt} \frac{1}{2} \left[1 + \operatorname{erf}\left(\frac{vt-x}{2\sqrt{Dt}}\right) \right] dx + \int_{vt}^L \operatorname{erfc}\left(\frac{vt-x}{2\sqrt{Dt}}\right) dx, \quad (4.5)$$

Equations (4.1)-(4.5) are used to calculate diffusion and convection in one dimension (e.g., a film). In order to be fully used for the current water sensor, the equations must be extended to three dimensions. However, the current form of the equations is enough for the simplified model shown in following two sections.

4.3.2. FBG Model

A more detailed description of FBGs is included in Chapter 2. For convenience, the relevant equations are presented below. The wavelength change of FBGs can be described by [(4.6)]

$$\frac{\delta\lambda_B}{\lambda_B} = \alpha_T \Delta T + \alpha_\varepsilon \Delta \varepsilon + \alpha_P \Delta P, \quad (4.6)$$

where λ_B is the Bragg wavelength (center wavelength), T is the temperature, ε is the strain, P is the pressure, and α_T , α_ε , and α_P are their respective coefficients. Aside from a small temperature drop during contact with water, the temperature and pressure terms may be neglected for the purposes of this experiment. This leaves α_ε to be defined as

$$\alpha_\varepsilon = 1 - p_e, \quad (4.7)$$

$$p_e = \frac{n_{eff}^2}{2} [p_{12} - \nu(p_{11} + p_{12})] , \quad (4.8)$$

where n_{eff} is the effective refractive index of the reflected mode, p_{11} and p_{12} are the elasto-optic tensor coefficients, μ is the poisson ratio, and P_e is the photoelastic constant of the fiber (assumed to be isotropic) [1].

4.3.3. Combined Model

In order to characterize the water sensor, we need to relate the swelling of the polymer to the strain experienced by the FBG. In other words,

$$\Delta \varepsilon = p(t)s(t) \quad (4.9)$$

where $p(t)$ is a proportion function that converts swelling to strain. The determination of $p(t)$ is beyond the scope of this document. However, an alternative expression may be found by beam theory. In order to develop a better idea of the interaction between the polymer and the FBG, we can refer to Figure 4-3, which contains the most simplified graphical model of the current water sensor.

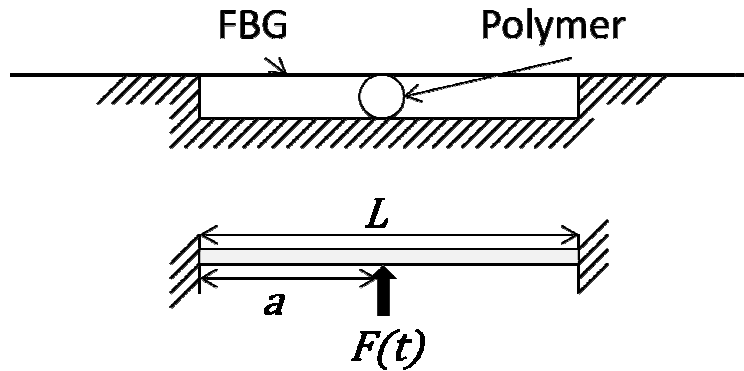


Figure 4-3. Graphical representation of the simplified water sensor.

As seen in Figure 4-3, the sensor has been approximated by a basic beam deflection problem. We assume $a = 0.5L$. The maximum deflection, δ_{max} , of the beam, which should occur at a , is given by

$$\delta_{max}(t) = \frac{F(t)L^3}{192EI} \quad (4.10)$$

where E is the Young's modulus of the beam, I is the moment of inertia, and F is the force acting at point a [74]. If we approximate the length deformation caused by the deflection ($\delta = \delta_{max}$) as seen in Figure 4-4,

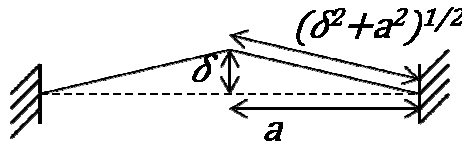


Figure 4-4. Approximation of the beam deformation due to deflection.

Then the strain can be approximated as

$$\Delta\epsilon = \frac{\Delta L}{L} = \frac{2\sqrt{\delta^2 + a^2} - 2a}{2a} = \frac{\sqrt{\delta^2 + a^2}}{a} - 1. \quad (4.11)$$

Substituting Equation (4.10) into Equation (4.11) and expressing a in terms of L , we obtain

$$\Delta\epsilon = \frac{2\sqrt{\left(\frac{F(t)L^3}{192EI}\right)^2 + \frac{L^2}{4}}}{L} - 1, \quad (4.12)$$

Equation (4.12) removes the need to find $p(t)$, however, an expression relating $F(t)$ to the concentration of water in the polymer is needed in order to relate FBG strain to water input. Hence,

$$\frac{\Delta\lambda_B(t)}{\lambda_B} = \alpha_e \Delta\epsilon = (1 - p_e) \left[\frac{2\sqrt{\left(\frac{F(t)L^3}{192EI}\right)^2 + \frac{L^2}{4}}}{L} - 1 \right] = (1 - p_e)p(t)s(t). \quad (4.13)$$

Here $F(t)$ may be seen as the expansion force of sodium polyacrylate in its spherical form. For the final model, we should assume full immersion of the sphere into water, and the input should take a form indicating the time that the sphere was exposed to water (e.g., a unit step function with a cut off time). The end result of this model is to be able to infer the amount of water absorbed by the polymer from the FBG signal. At the present, Equations (4.11)- (4.13) is a foundation for development of a beam-deflection based model. Subsequent developments will take into account the stiffness of the beam as well as the response from the nitinol rails. More importantly, the $F(t)$ term will require further investigation for a satisfactory analytical expression. Further tests relating polymer volumetric expansion and the associated expansion forces are needed. In more advanced models, the reaction of the polymer expansion behavior in the presence of mechanical obstacles (e.g., deformation of the polymer around obstacles) will be considered.

4.4. Experimental Setup

4.4.1. Polymer Swelling Characterization

The swelling limits of the polymer beads were tested. Ten measurements were made to random beads for dry and swollen measurements. Distilled water was used.

4.4.2. Sensor Cycling

Two FBGs (1560 nm and 1552 nm center wavelengths) were placed in two separate housings. Each FBG was prestrained with a positive 0.5 nm shift (tension) before fixation at the conduits of the housing. A FBG based temperature sensor was placed in the nearby area to compensate for thermal effects. Each sensor was connected to an interrogator (Micron Optics sm130), which sent data via ethernet to a PC running ENLIGHT. Data was acquired in parallel for all three sensors at a rate of 1Hz. To commence testing, a package containing one polymer bead was placed underneath the pretensioned FBG (Figure 4-5). A syringe was used to transfer drinking water from a local container to the sensors, including the temperature sensor. For the purposes of convenience, the middle section was not added, thus exposing the FBG and the package to the atmosphere. A small aluminum plate (10 mm x 40 mm) was placed underneath the package to enhance water retention within the housing, and also promote contact between the package and the FBG. Table 4-1 details the tests conducted with the sensors. At 1.0 mL input volume, in order to investigate the effects of higher sensor stiffness (i.e., FBG and rail assembly) the rail sensor received two additional wires that were situated perpendicular to the two existing wires, forming a checker pattern. It may be noteworthy that the cycling tests were done in the following order: 0.1 mL, 1 mL, 0.5 mL, 0.3 mL, and 0.7 mL. At the end of the 1 mL test, the sensor with the Free configuration required repair and the polymer bead was replaced with a new one.

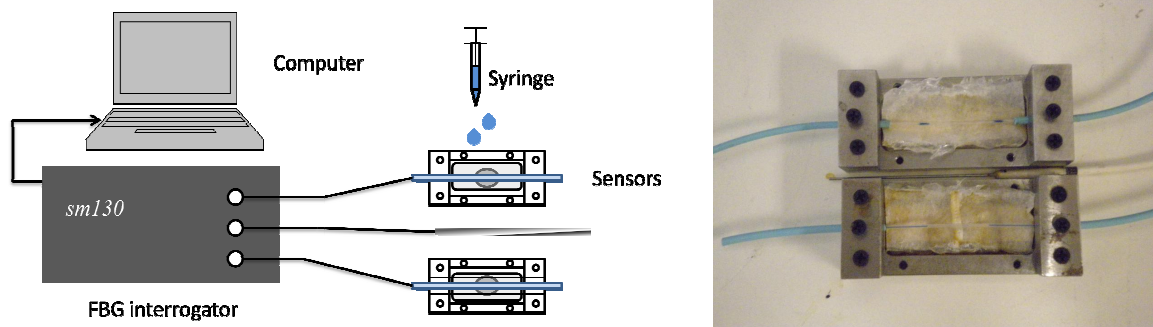


Figure 4-5. Experimental set up for testing the water sensors.

Table 4-1. Summary of the cycling experiment.

Input Volume (mL)	Number of Cycles	Sensor Configuration
0.1	6	Free
0.3	4	Free, Rail
0.5	3	Free, Rail
0.7	3	Free, Rail
1.0	4	Free, Rail (x4)

4.4.3. Flooding Simulation

In the final test, a flooding scenario was simulated by immersing the sensors into a water bath (Figure 4-6). Only two wires were used for the rail configuration during the flooding test.

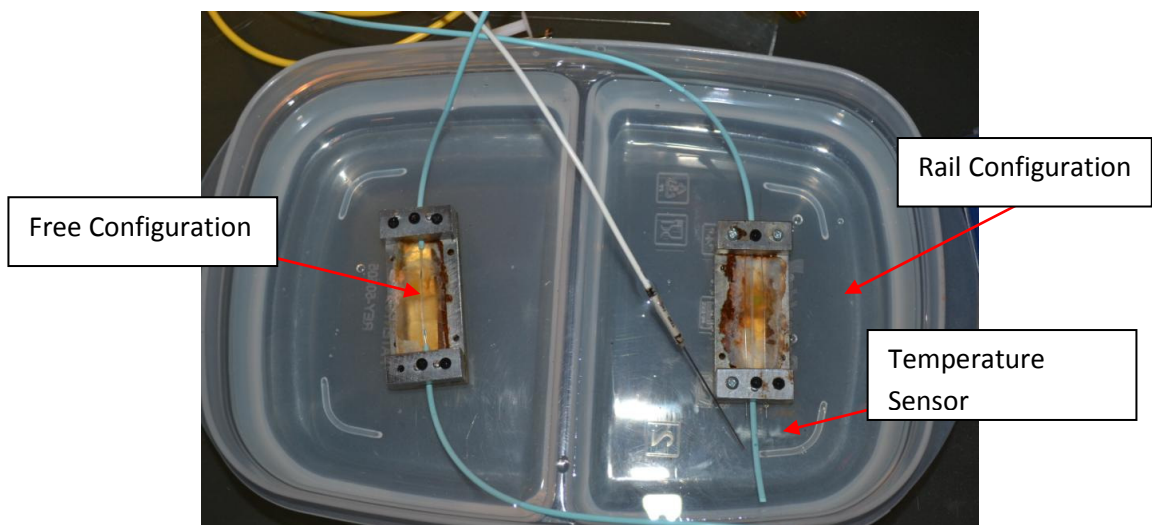


Figure 4-6. Submersion of FBG water and temperature sensor into a water bath.

4.5. Results

4.5.1. Polymer Swelling Characterization

The average dry and swollen mass of the acquired sodium polyacrylate beads were found to be $0.019 \pm 0.003\text{g}$ and $1.91 \pm 0.293\text{g}$, respectively. These values indicate the beads are able to carry an average of 1.89 mL of water (assuming a unity density of 1g/mL).

4.5.2. Sensor Cycling

It can be seen in the following graphs of the data that the water sensor had good repeatability for each of cycling. On some occasions, especially for 0.5 mL input, the lateral movement of the polymer bead in the Free configuration caused a sudden drop in signal. Varying the input volume for the Free configuration returned a proportional variation in the peak amplitude. This variation was also seen at a lower magnitude for the Rail configuration. A summary of the results is shown in Table 2. In the following graphs (Figure 4-7-Figure 4-11), the left column (Labeled A and C) shows the overall cycling and the right column (Labeled B and D) shows a zoomed in portion of a single cycle. The

temperature is shown in the plots labeled as E. Each color represents a different cycle.
The response of the temperature probe is also shown.

0.1 mL Input

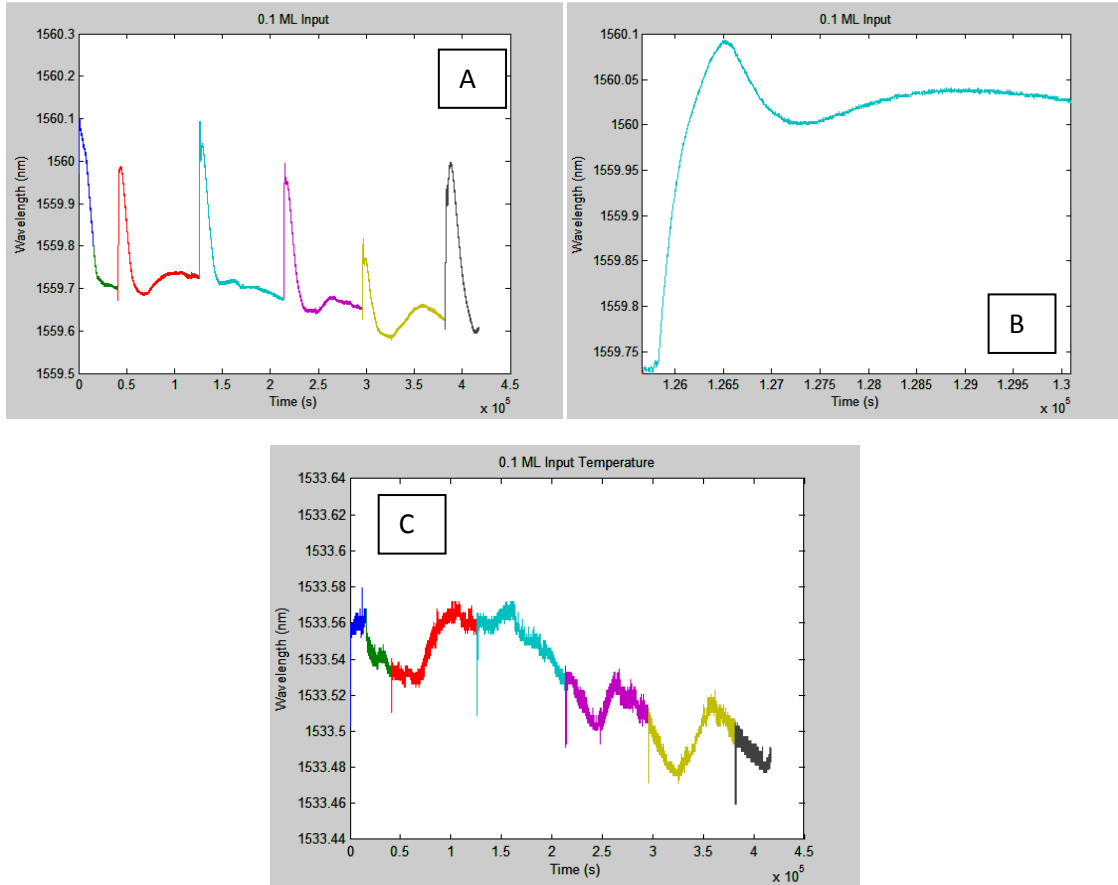


Figure 4-7. 0.1 mL of drinking water was input into the Free configuration sensor six times.

0.3 mL Input

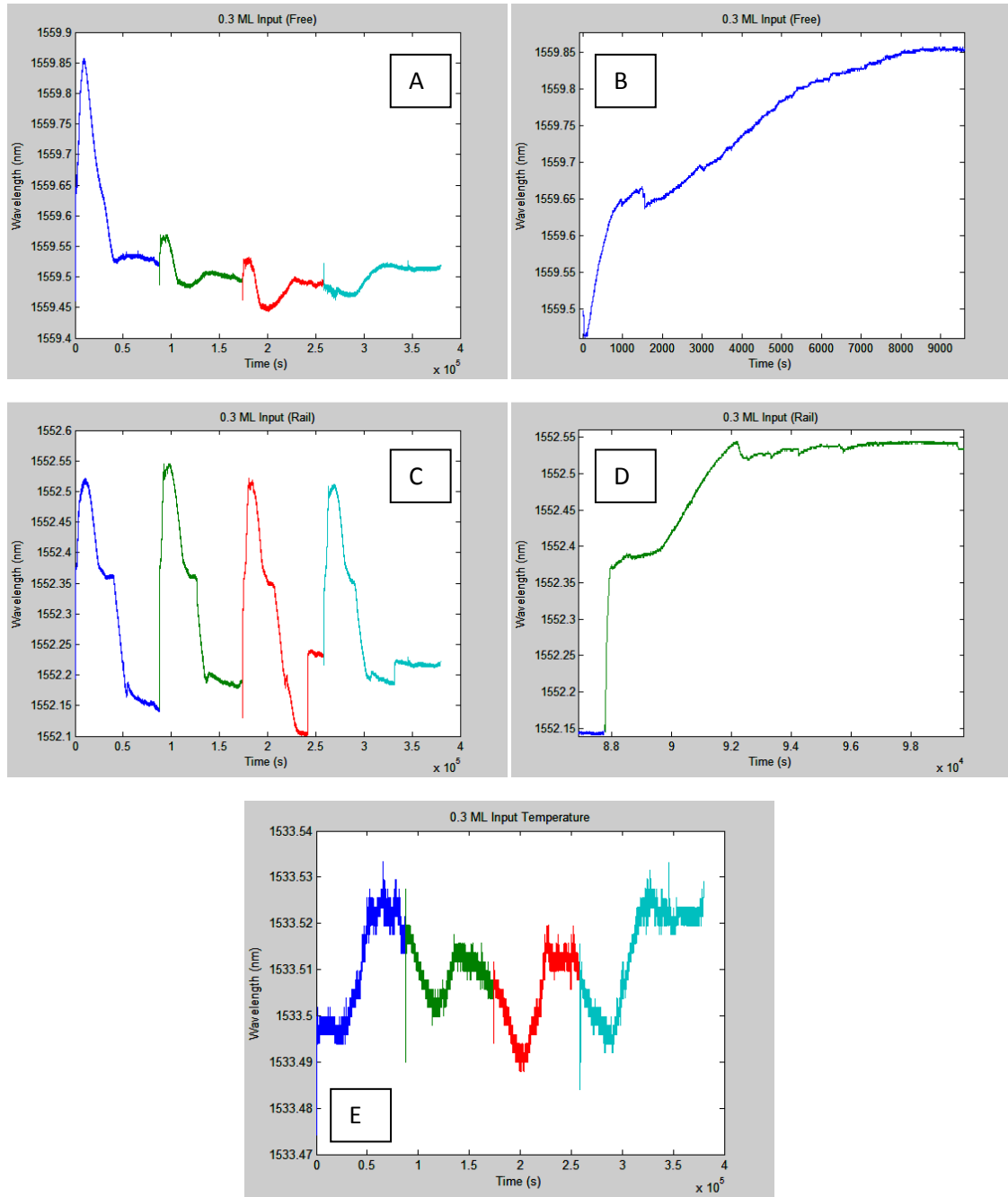


Figure 4-8. 0.3 mL of drinking water was input into the Free and Rail configuration sensor four times.

0.5 mL Input

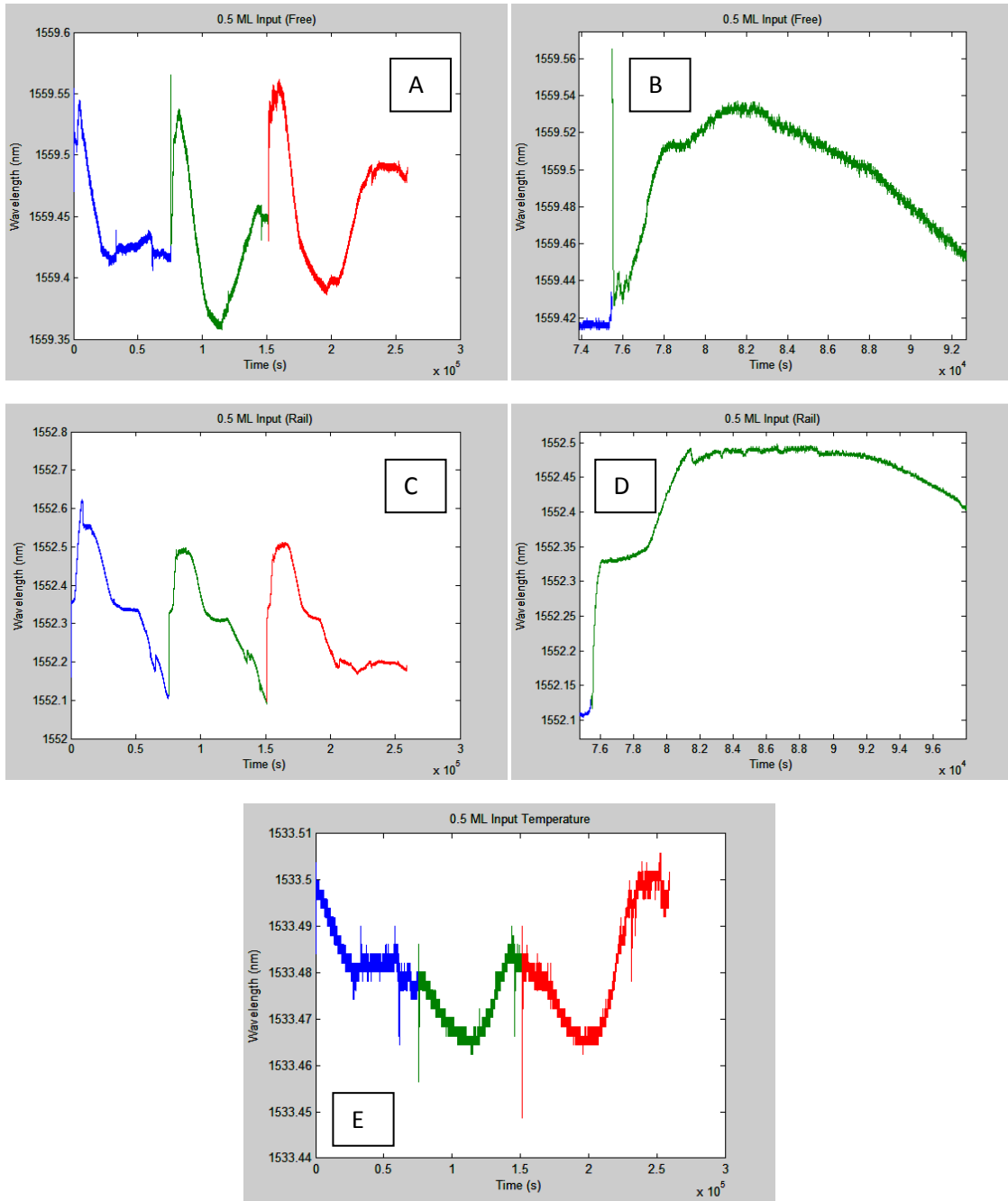


Figure 4-9. 0.5 mL of drinking water was input into the Free and Rail configuration sensor three times.

0.7 mL Input

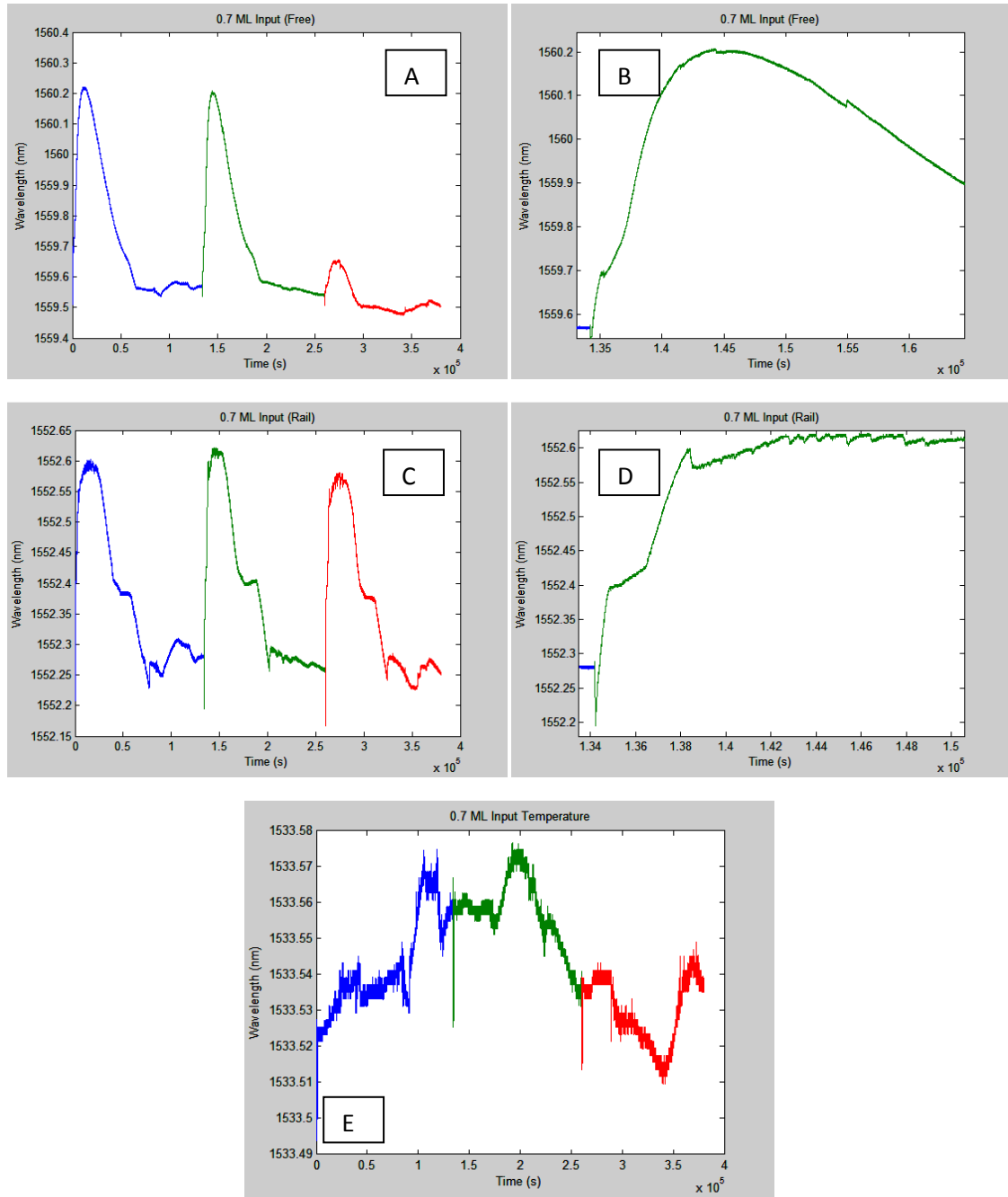


Figure 4-10. 0.7 mL of drinking water was input into the Free and Rail configuration sensor three times.

1 mL Input

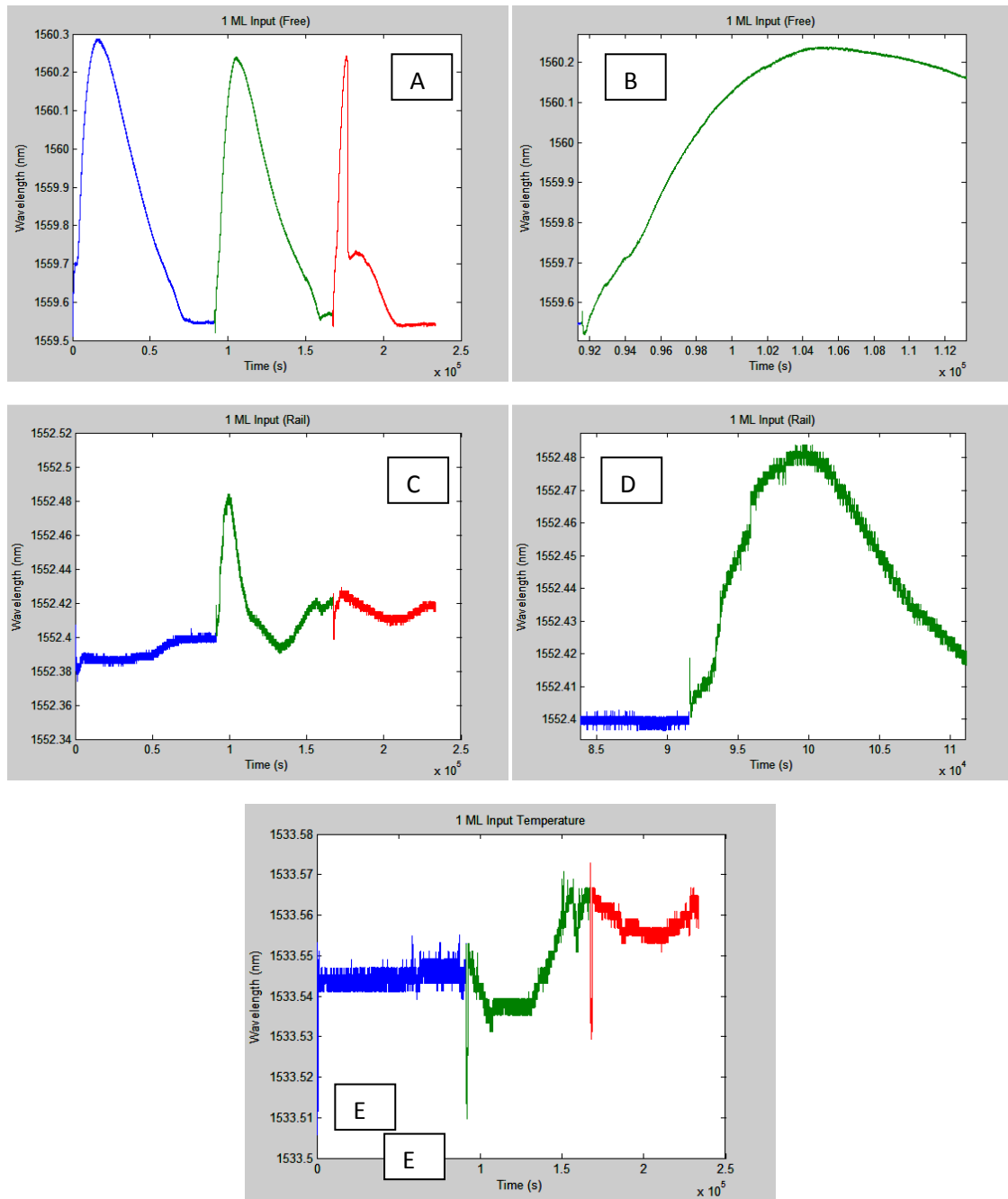


Figure 4-11. 1.0 mL of drinking water was input into the Free and Rail(x4)configuration sensor three times.

Table 4-2. Summary of cycling results for both sensor configurations.

Volume Input (mL)	Average Peak Amplitude {Free} (nm)	Average Time to Peak (s) {Free}	Average Cycle Time (hr) {Free}	Average Peak Amplitude (nm) {Rail}	Average Time to Peak (s) {Rail}	Average Cycle Time (hr) {Rail}
0.1	0.275±0.094	1109±448	5.80±1.60	/	/	/
0.3	0.397*	9251*	8.76*	0.3525±0.0495	10518±630	11.50±1.20
0.5	0.103±0.027	6107±1767	6.20±2.60	0.3953±0.172	13959±947	13.22±0.85
0.7	0.684±0.035	12323±2591	11.8±4.74	0.4107±0.166	14601±3805	15.20±1.90
1.0	0.734±0.037	12829±3512	13.2±3.60	/	/	/

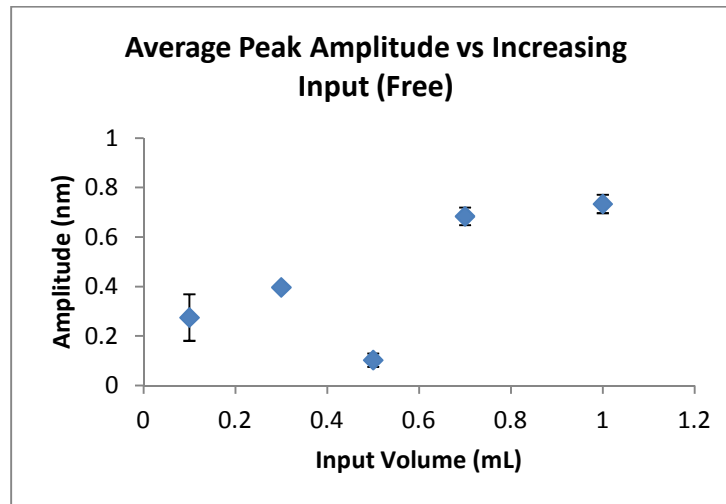


Figure 4-12. Average peak amplitude (with standard deviation) for increasing input volumes into the Free sensor configuration.

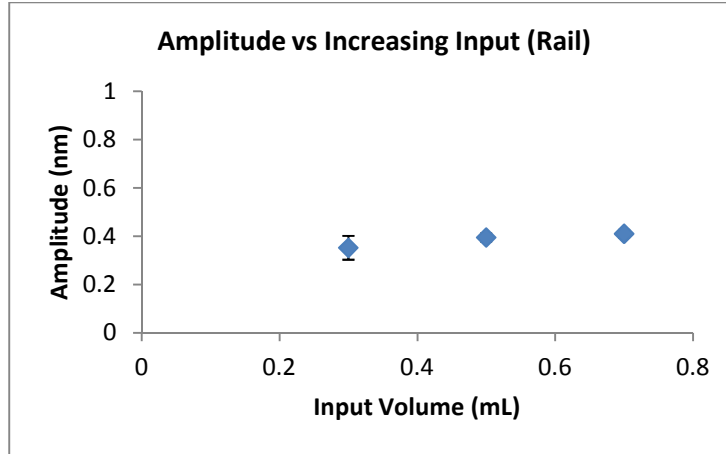


Figure 4-13. Average peak amplitude (with standard deviation) for increasing input volumes into the Rail sensor configuration.

4.5.3. Flooding Simulation

Both sensors survived flooding. Unlike last time, the packaging did not tear and the polymer did not escape into the environment. Time allowed for only two cycles. As seen in the first cycle, both sensors experienced some instability in the signal form due to the initial swelling of the polymer. The first sensor configuration had a fully expanded bead that moved out from under the FBG, and the second sensor configuration expanded to fill the whole package, but was deformed in the process. On the second cycle, the expansion and contraction was smooth.

The saturated signal for the first sensor configuration (Free) was about 0.7 nm difference from the base line. For the second sensor configuration (Rail), the signal saturated about 0.32 nm.

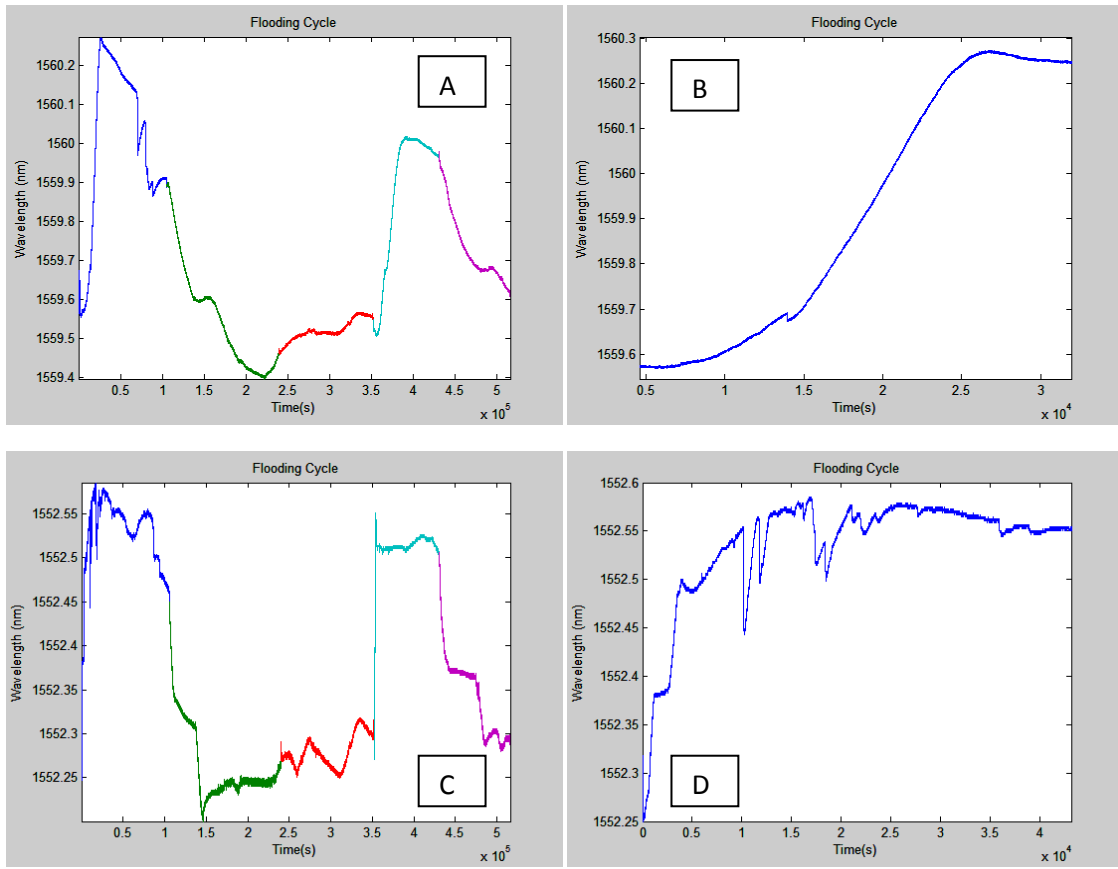


Figure 4-14. Flooding test for both sensor configurations.

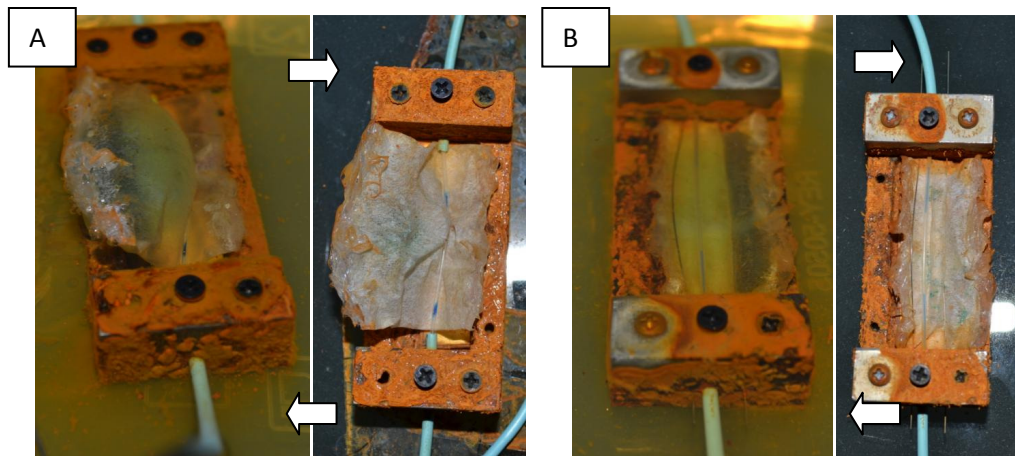


Figure 4-15. Photo of water sensors under flooding conditions. (A) (Left) Flooded situation for Free configuration, (Right) Dried sensor after flooding; (B) (Left) Flooded situation for Rail configuration, (Right) Dried sensor after flooding.

4.6. Discussion

As seen in the results, both configurations of the water sensor were able to undergo cycling. However, each cycling event had unique differences compared to other cycles within the same test. These differences can be attributed to variables such as human-induced variation during the water input, or movements and deformations of the polymer bead.

Temperature variations were reflected in the sensor readings. However, the temperature-induced fluctuations were small compared to the sensor response to water input. In application, an algorithm will be required to compensate for the temperature changes by subtracting readings from the temperature probe. For this experiment, the temperature was only shown, but not used to compensate for temperature changes in the water sensors.

Each wetting and drying cycle induced small longitudinal and lateral displacements of the polymer bead within the packet. This was most obvious for the Free configuration sensor (see Figure 4-7A-Figure 4-11A). Despite having generally stronger responses than the Rail configuration, such movements will severely hinder the reusability of the sensor during field deployments. Manual re-centering of the polymer bead was required after each cycle in Figure 4-8A, hence the large initial value seen at the beginning of each cycle. On the other hand, the Rail configuration did not face such a problem due to the motion restricting effects of the superelastic wires. However, as seen from Table 4-2 and Figure 4-13, the response of the Rail configuration sensor only had small increases in average peak amplitude with correlation with increasing input volume. The peaks although smaller, were similar in amplitude, indicating that the sensor has

reached saturation in terms of the sensible water capacity. Overall, the Rail sensor configuration sensor had a much more stable performance than the Free configuration sensor, highlighting the need for a mechanism that prevents the lateral displacements of the polymer bead.

A close examination of the initial loading profile for the rail configurations reveals that the loading curve experiences at least two slopes prior to reaching the maximum value. Figure 4-16 examines the loading curve of the rail configuration during the 0.7 mL test. Slope “A” denotes the initial expansion of the polymer bead against the FBG. Slope “B” denotes contact of the polymer bead with the nitinol wire rails. The added stiffness is reflected by the relative flatness of slope B. Slope “C” denotes that the nitinol wire rails, while still in contact with the polymer bead, have parted slightly around the bead to allow the refocusing of the expansion-induced strain onto the FBG. Thus, slope C is more similar to slope A, but is slightly flatter due to the side contact with the rails. Finally, in slope “D,” the force of expansion from the polymer bead is no longer able to strain the combined FBG and rail assembly. In order to continue expanding, the polymer bead must either deform horizontally or begin breaking up. The multiple downward peaks in slope D were caused by minor strain relief due to shifting and the formation of small cracks on the polymer bead. As seen from the multiple loading cycles, any transformations (deformation, shifting, cracks, etc.) of the polymer bead did not have noticeable effects on the repeatability of the sensor. On the other hand, the loading curve of the Free sensor configuration did not have as many events, due to the presence of a single FBG cable instead of the additional obstacles imposed by the nitinol wires.

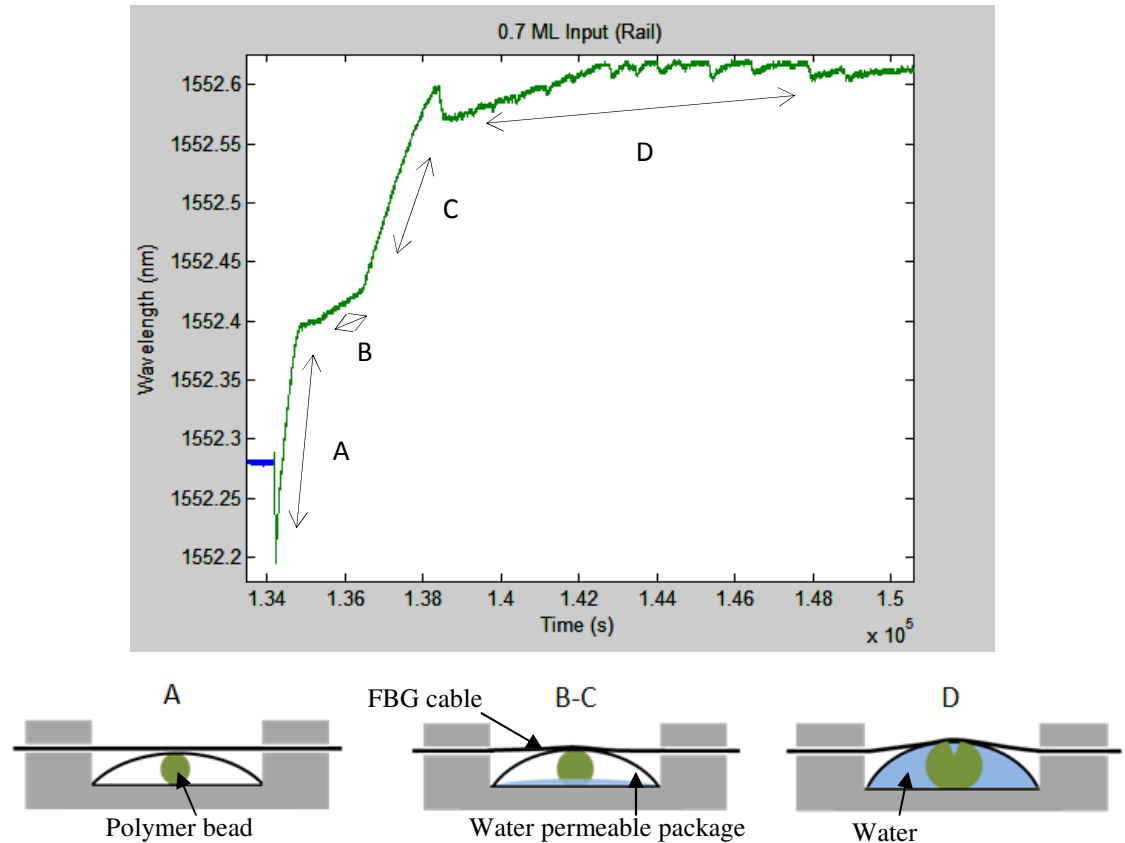


Figure 4-16 Different stages of loading for the Rail configuration sensor. A) Initial loading; B-C) Contact with rails and continued expansion; D) Saturation of sensor and cracking of polymer bead.

The continuous, repeated exertion of the polymer on the FBG may contribute to the loosening of fixture points of the fiber cable. A less secure fixture will be reflected in a diminished sensitivity of the sensor to polymer swelling. However, this loosening effect was absent or kept at a minimum for both sensors configurations as attenuation of peak amplitudes was not observed unless accompanied by displacement of the polymer bead. Another potential factor in sensor response was sensor rusting. It was observed early during the cycling tests that the metal rusted due to the presence of moisture. Discoloration of the polymer and the packet due to rust was noticeable after several cycles, and is suspected to play a minor, albeit unclear role in affecting water uptake by the polymers. For example, a small peak may be seen in the sensor response during the

early 0.1 mL test, but the peak was not as obvious during subsequent tests. The small peak has been attributed to a transient over-crosslinking in the polymer during water uptake, along with various polymer-solvent interactions [68]. The addition of rust particles may have interfered with the normal absorption process. On the other hand, during the real application (i.e., embedded in concrete), electrolytes carried by ingressing moisture will reduce the osmotic pressure experienced by the polymer and thus reduce sensor sensitivity.

During the cycling tests, the input volume during the cycling test was higher than the actual volume absorbed by the polymer bead. The loss of input volume was contributed by evaporation, absorption into the packet membrane, and leakage of the water through sensor windows. However, despite the losses, the absorption volume of the polymer beads correlated directly with increasing input volumes (Figure 4-12-Figure 4-13, disregarding the 0.5 mL input of the Free sensor configuration). This correlation is expected to plateau off as the rate of loss due to evaporation exceeds the absorption rate of the polymer bead. Thus, a theoretical maximum signal exists for intermittent inputs (i.e., not flooding), especially since the absorbing capacity of the polymer will reach a physical limit (tests show an average of 1.86 mL capacity). Another limiting factor is the presence of the FBG. Since the FBG is much more rigid and structurally stable than the polymer bead, the FBG cable will only deform/strain to a certain extent before forcing the polymer to either displace or expand (or split) around the fiber as seen in Figure 4-16.

One of the potential situations that may occur during the monitoring of water ingress in a structure is the influx of large amounts of water, leading to flooding conditions. The ability of the sensor to survive such conditions is beneficial if structural

damage allowing such flooding can be repaired; otherwise, the sensor will become unusable afterwards. From the flooding results (Figure 4-14), both sensor configurations were able to survive extended submersion into a body of water. However, for a significant deformation of the polymer bead can be observed both visually and in the data, especially for the rail sensor configuration. Similar to slope D in Figure 4-16, the sudden downward peaks in the data correspond to the deformation and breaking up of the polymer as volumetric constraints imposed by the sensor packaging force the polymer to expand irregularly.

Although several hours may be needed for the sensors to reach equilibrium levels (Table 4-2, Average Time Peak), the actual level upon which the presence of water is practically guaranteed. This threshold is typically crossed at 10 minutes, where the response reaches approximately 0.2 nm in amplitude. The recovery time (6-15 hrs, depending on input volume) was short in terms of the serviceability of most concrete structures. Therefore, for non-flooding scenarios, the Rail sensor configuration should perform adequately for liquid moisture detection at selected locations within a concrete building.

4.7. Conclusions

In order to better monitor the health of concrete structures, it is important to know if water has invaded and perhaps corroded the reinforcement system. A water sensor was designed to detect the presence of water (liquid moisture). A basic mathematical characterization of the sensor was constructed using theories available in literature. Further development of the characterization should allow inference of water levels in the water sensor. With the installation of motion restriction measures for the sodium

polyacrylate bead, the sensor had good repeatability through many loading cycles. On the other hand, the sensor design currently has some insufficiencies in dealing with flooding conditions. With stronger packet materials or smaller polymer beads, however, this problem should be solved.

Chapter 5 Dynamic Fiber Bragg Grating Sensing Method

5.1. Introduction

In designing and handling mechanical structures, one commonly encounters situations in which the measurement of high frequency vibrations plays an important role. Such high frequency measurements are valuable especially in the area of structural health monitoring. While FBGs have been well studied and understood for quasi-static strain and temperature measurements, their use for high frequency, dynamic measurements were impeded by sampling frequency limited optical spectrum analyzer components [75]. Throughout the past years, multiple intensity modulation-based methods have allowed high frequency interrogation of FBGs, some of which are discussed in Chapter 2. The use intensity modulation for the interrogation of FBGs involves the use of an optical filter that can adjust the intensity of incoming light based on the wavelength of the light. Haber et al., for example, designed a high rate FBG interrogator through the use of a fiber Fabry-Perot tunable filter [76]. Cusano et al. used an asymmetric FBG as an optical filter that preceded a single photodetector. The method was used to demonstrate measurement of signals up to 50 kHz [77]. Another intensity based FBG interrogation method is the use of arrayed waveguide grating (AWG). The AWG, which consists of an array of narrow-band optical filters, allow dense multiplexing of FBGs (theoretically up to 128 FBGs) [78, 79, 80]. Recently, a method developed by Betz et al. made use of an extremely narrow band laser source and a regular FBG for the dynamic detection of high frequency events. By tuning the laser source at the spectral full width at half maximum (FWHM) of a highly apodized FBG, any wavelength shifts of the FBG will be translated to intensity fluctuations in the reflected spectrum. Their system demonstrated the measurement of ultrasonic vibrations [81, 82]. Tosi et al and Isago et al. later performed

high frequency FBG interrogation using a similarly narrow band laser source [83, 84]. The above methods are especially suitable for use in structural health monitoring, and are gaining popularity for use in cases where dynamic signals can point to structural damage. As seen in the literature, high frequency FBG interrogation methods utilizing similar principles as in the above were used to analyze the effects of impact on various structures, as well as for monitoring of structural changes over time (e.g., delamination) [85-89].

The intensity modulation methods described above require the use of special filters or laser sources. A separate class of such methods exists in which regular FBGs can be used as the filter, thus potentially driving down costs and simplifying the system. For instance, Ribeiro et al. and Wang et al. proposed similar set ups in which the signals of a sensing FBG could be measured without the use of additional filtering or interrogation techniques [90,91]. In their methods, the reflection spectrum of two wavelength matched FBGs are compared by a photodiode. The more overlap there is between the center wavelengths of the two FBGs correlate, the higher the amount of power received by the photodiode [90,91]. If the FBGs are placed adjacent to each other at close proximity, the effects of thermally induced strain can be minimized. Thus, although these wavelength-matched methods require dual FBGs per sensor and may need additional equipment for multiplexing (e.g., switches), the methods free the user from the cost and sampling frequency related limitations of specialized components, such as scanning optical filters.

In the following sensor development, an alternate wavelength matched set up using regular FBGs is described that is also able to measure dynamic signals such as acoustic vibrations. While Ribeiro et al. and Wang et al. utilized the reflection of two

FBGs, the following set up utilizes the transmission spectrum of one FBG and the reflection spectrum of the other. The immediate benefit of this approach is the inclusion of fewer optical couplers, which can be a source of optical power loss in previous systems, and as will be seen can thus increase the sensing range of the system.

5.2. System Design

The proposed dynamic FBG sensor system takes advantage of the power fluctuations due to the intersection of the reflection and transmission spectrums of two FBGs (Figure 5-1). A laser with a broad band spectrum is injected into an optical circuit containing two wavelength matching FBGs, a coupler, and a power meter (e.g., photodiode).

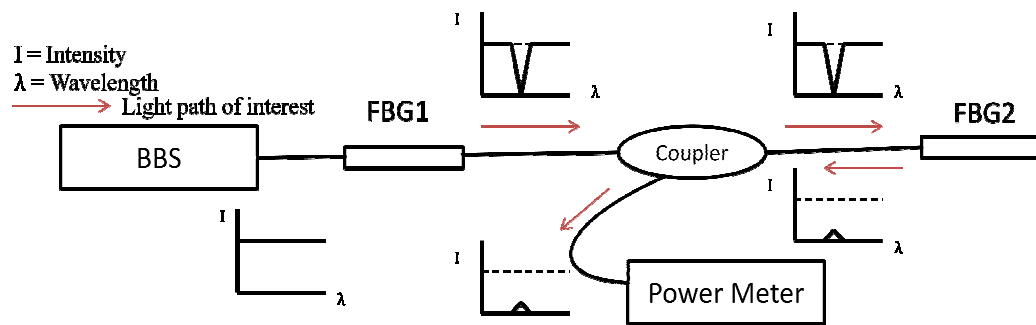


Figure 5-1. Optical circuit of the wavelength-matched dynamic FBG sensing system.

As seen in Figure 5-1, the first FBG filters out most of the optical power in the incident spectrum. The transmitted portion of the spectrum crosses the coupler to reach the second FBG. At this point, any remaining energy correlated with the FBG's central wavelength will be reflected back towards the light source and a power meter. If the two FBGs are exactly wavelength matched, a minimum amount of energy will be detected by the power meter. Any mismatch between the central wavelengths of the two FBGs will

cause in increase in energy until the reflection spectrum of the FBGs no longer overlap. The mismatch may be caused by the measurand, such as vibrations. Once the reflection spectrum no longer overlaps, the reading from the power meter will appear saturated.

5.3. Calculation of spectral width

The intensity of the vibrations determines how far the reflection spectrums of the two FBGs move relative to each other. As discussed before, saturation occurs when the vibration intensity moves the reflection spectrums out of the overlapping region. The following is an examination of the spectral width and potential optimization methods.

The spectrum of the BBS may be approximated by Equation (5.1) [90],

$$S(\lambda) = I \exp \left(-4(\ln 2) \left(\frac{\lambda - \lambda_0}{\Delta\lambda_0} \right)^2 \right), \quad (5.1)$$

where $\Delta\lambda_0$ is the FWHM of the BBS, λ_0 is the center wavelength, and I is the peak power.

I is defined by

$$I = \frac{P_0}{\Delta\lambda_0} \left(4 \ln \left(\frac{2}{\pi} \right) \right)^{\frac{1}{2}}, \quad (5.2)$$

where P_0 is the total power injected into the system from the BBS. The ideal BBS should be smooth and flat in the operating region of the FBG.

As described in Chapter 2, the reflectivity of a simple FBG can be described by

$$P = \frac{\kappa^2 \sinh^2(\alpha L)}{\kappa^2 \cosh^2(\alpha L) - \xi^2}, \quad (5.3)$$

The use of Equation (5.3) involves the use of many parameters, and can be cumbersome to use. However, an alternative equation can be used instead of equation 3 for the convenience of modeling. The reflectivity of the FBG (indexed by i) can be alternatively described as a Gaussian distribution (Equation (5.4)) [90]

$$D_i(\lambda) = A_i \exp\left(-4(\ln 2)\left(\frac{\lambda - \lambda_{Bi}}{\Delta\lambda_{Bi}}\right)^2\right), \quad (5.4)$$

where $D_i(\lambda)$ is the Gaussian approximation of the FBG reflectivity, A_i is the maximum reflectivity of the FBG, λ_{Bi} is the center wavelength of the FBG, and $\Delta\lambda_{Bi}$ is the FWHM of the FBG. For the purposes of this experiment, the FBG closest to the BBS is indexed by $i = 1$, and the matching FBG is indexed by $i = 2$. Figure 5-2 compares the exact model and the Gaussian model of the FBG reflectivity.

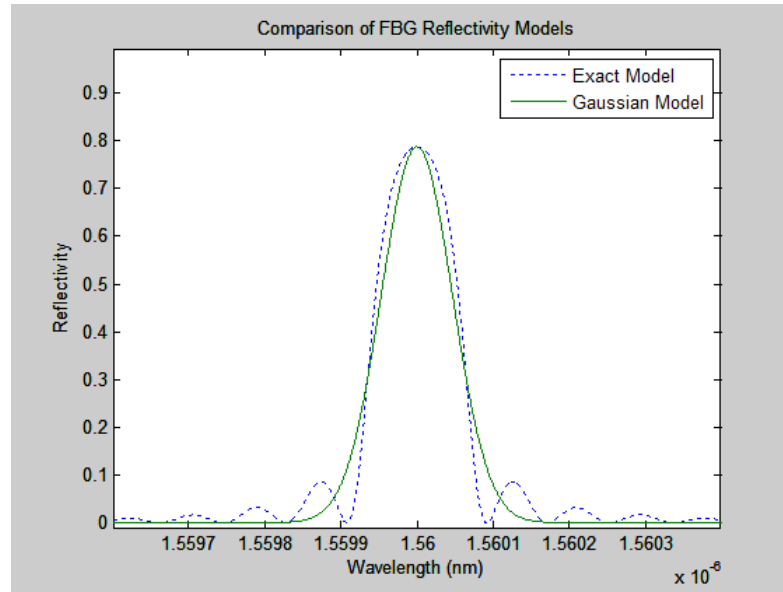


Figure 5-2. Comparison of FBG Reflectivity Models.

Consequently, the reflection spectrum $T(\lambda)$ of FBG1 due to the input of the BBS is

$$E_1(\lambda) = S(\lambda_B)D_1(\lambda) , \quad (5.5)$$

where λ_B is the center wavelength of the wavelength-matched FBGs and $S(\lambda_B)$ gives the amplitude of the lamb in the spectrum of the BBS. The transmission spectrum of the first FBG is

$$T(\lambda) = S(\lambda_B)(1 - D_1(\lambda)) . \quad (5.6)$$

Thus, the spectral distribution observed received by the photodetector is

$$E_2(\lambda) = T(\lambda)D_2(\lambda) . \quad (5.7)$$

The energy profile of the optical path is traced in Figure 5-3.

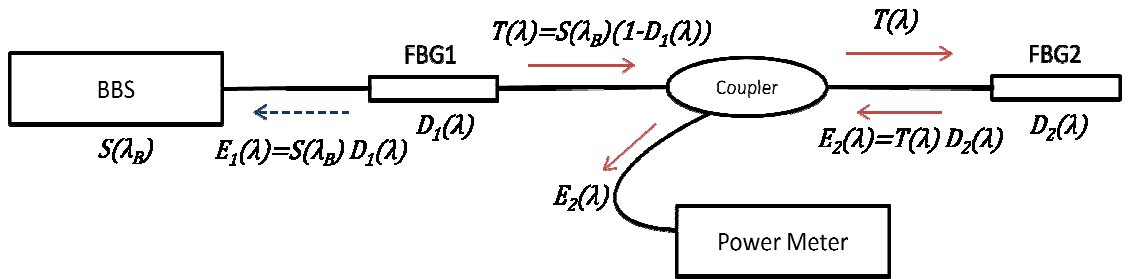


Figure 5-3. Tracing of the optical power along the sensor system's optical circuit.

The reflection (E_1) and transmission (T) spectrums of FBG1 and the reflection spectrum (E_2) of FBG2 (the spectrum seen by the photodetector) is shown in Figure 5-4, as calculated by Equations (5.1)-(5.7) assuming $A_{1,2} = 90\%$ and $\lambda_{B1,B2} = 1560$ nm.

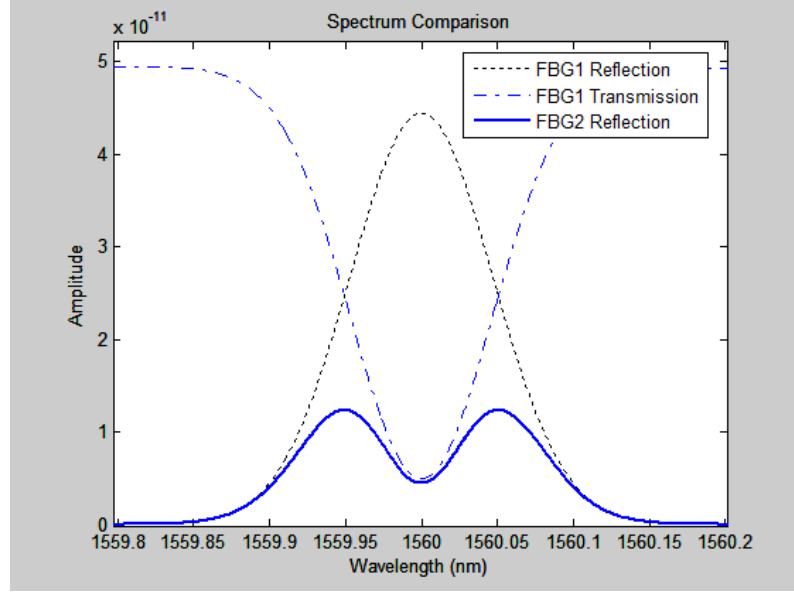


Figure 5-4. Comparison of the relevant spectrums of FBG1 and FBG2.

The total power received by the photodetector is

$$W = k^2(1-k)^2 \int_{-\infty}^{\infty} T(\lambda) D_2(\lambda) d\lambda, \quad (5.8)$$

$$W = k^2(1-k)^2 S(\lambda_B) \int_{-\infty}^{\infty} D_2(\lambda) - D_1(\lambda) D_2(\lambda) d\lambda, \quad (5.9)$$

$$W = k^2(1-k)^2 S(\lambda_B) \int_{-\infty}^{\infty} A_2 \exp\left(-4(\ln 2) \left(\frac{\lambda - \lambda_{B2}}{\Delta\lambda_{B2}}\right)^2\right) - A_1 A_2 \exp\left(-4(\ln 2) \left(\frac{\lambda - \lambda_{B1}}{\Delta\lambda_{B1}}\right)^2 - \left(\frac{\lambda - \lambda_{B2}}{\Delta\lambda_{B2}}\right)^2\right) d\lambda. \quad (5.10)$$

Using the relationship

$$\int_{-\infty}^{\infty} A \exp(-ax^2 + bx + c) dx = A \sqrt{\frac{\pi}{a}} \exp\left(\frac{b^2}{4a} + c\right), \quad (5.11)$$

and assuming $\Delta\lambda_{B1} = \Delta\lambda_{B2}$ (both FBGs have the same FWHM), the following expression can be obtained

$$W = k^2(1-k)^2 P_0 A_2 \beta(\lambda_{B1}) \frac{\Delta\lambda_B}{\Delta\lambda_0} \left(1 - \frac{A_1 \alpha(\lambda_{B1}) \sqrt{2}}{2}\right), \quad (5.12)$$

where

$$\alpha(\lambda_{B1}) = \exp\left(-2(\ln 2)\left(\frac{\lambda_{B1} - \lambda_{B2}}{\Delta\lambda_{B2}}\right)^2\right), \quad (5.13)$$

and

$$\beta(\lambda_{B1}) = \exp\left(-4(\ln 2)\left(\frac{\lambda_{B1} - \lambda_0}{\Delta\lambda_0}\right)^2\right). \quad (5.14)$$

From Equations (5.12)- (5.14), it can be seen that the minimum optical power occurs when the center wavelengths of FBG1 and FBG2 overlap exactly (Figure 5-5). Different FBG FWHMs are plotted simultaneously in Figure 5-4, and from comparison shows that a higher FWHM produces a larger range before saturation occurs. The specification of the FBG FWHM is established during the FBG fabrication stage, which is beyond the scope of this discussion. However, there are various types of FBGs that have unique reflectivity profiles that effectively expand the FWHM. For example, chirped FBGs have much wider spectral widths than type 1 FBGs.

On the other hand, a consideration of the power versus wavelength mismatch in Figure 5-5 reveals that in order for signals to have a unique power output for a certain amount of strain, the wavelength mismatch must remain within either half of the power profile. As will be seen in the simulation and results, an overly large strain input will cause the wavelength mismatch to produce saturated or non-unique power outputs from the photodetector. Optimally, one FBG should be carefully tuned so that the initial or resting wavelength mismatch is in the center of one of the two slopes consisting the power profile. For example, if the width of the power profile is ± 0.4 nm, the linear regions will approximately be between -0.38 to -0.02 nm and +0.02 to +0.38 nm (in terms

of wavelength mismatch), and the initial wavelength mismatch should be tuned to either -0.20 nm or +0.20 nm to maximize the amount of linearity in the sensor system response in either direction.

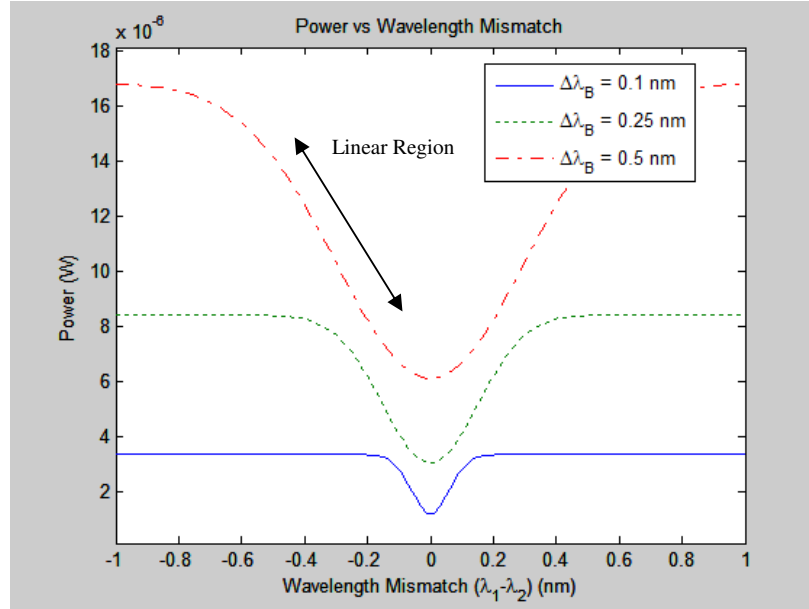


Figure 5-5. Photodetector power versus wavelength mismatch between FBG1 and FBG2.

Any strain on either FBG1 or FBG2 will cause a deviation between their center wavelengths and thus an increase in the optical received at the photodiode. For a sensor system with parameters $k = 0.5$, $A_{1,2} = 0.9$, $\Delta\lambda_B = 0.1$ nm, $P_0 = 0.0501$ W (17 dbm), and $\Delta\lambda_0 = 80$ nm (lowest profile shown in Figure d4), the full spectral width of the power profile is about ± 0.17 nm, corresponding to a detection of ± 141.67 $\mu\epsilon$, according to an assumed bare FBG strain sensitivity of 1.2 pm/ $\mu\epsilon$. Strains outside the range will cause a saturation of the optical power.

5.4.Experimental Setup

Two experiments were performed using the setup shown Figure 5-6. The first experiment had one FBG sensor directly bonded to a piezoelectric (PZT) actuator, and

the second experiment had one FBG sensor bonded at a distance away from a PZT actuator. In both experiments, FBGs with at least 90% reflectivity were used. Connection between the FBGs and the photodiode was allowed using a 3 dB optical coupler. The FBGs had approximately 0.15 nm mismatch, as assisted by a linear stage and a custom FBG interrogator.

5.4.1. Experiment 1 – FBG sensor directly bonded to PZT actuator

Two Type I FBGs with matching wavelengths at 1560 nm were used in the experimental setup as shown in Figure 5-6. One of the FBGs (FBG1) was bonded via cyanoacrylate onto a 2.5” x 1” PZT wafer while the other (FBG2) was mounted on an adjustable linear stage. An waveform generator (Agilent 33120A) was used to drive the PZT wafer. The FBGs were illuminated using an broad band source (BBS) (ASE laser in the C band), and the power level at the overlapping wavelength was measured by a PIN photodiode (InGaAs, ETX 75HB). The voltage across a parallel resistor (51.1 kOhms) was recorded by an NI board (X series 6353).

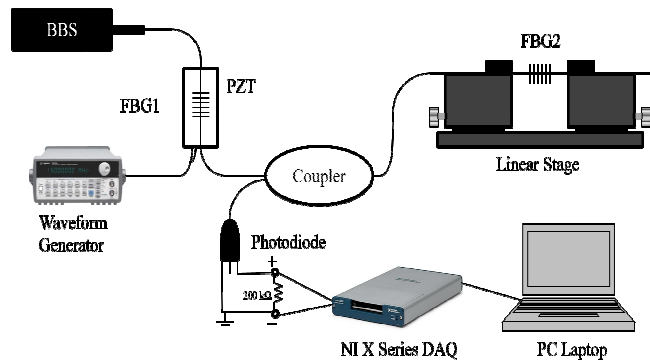


Figure 5-6. Set up of Experiment 1.

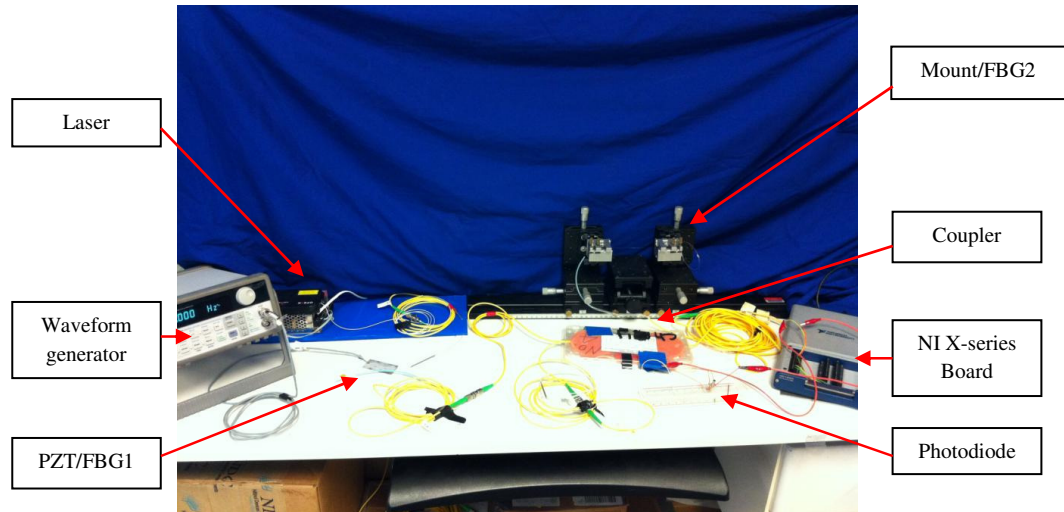


Figure 5-7. Set up of Experiment 1 (photo).

A sweep sine from 0 to 100 kHz over 4 seconds at 10 V was input into the PZT in order to examine the frequency response of the system. The sampling rate was set at 500 kHz. Frequency domain results were processed with the `pwelch` command from MATLAB using a hanning window of 5000 points (corresponding to a lower end window frequency of 100 Hz) with 50% overlap.

5.4.2. Experiment 2 – FBG sensor bonded at a distance away from PZT actuator

In the second experiment, an FBG strain sensor (see Chapter 4) with a sensitivity of $2.2 \text{ pm}/\mu\epsilon$ was bonded via cyanoacrylate to a model wind turbine blade while another FBG with a matching wavelength at 1568 nm was mounted on a linear stage for precise wavelength adjustment (Figure 5-8). In regards to Figure 5-8, the set up of Experiment 2 is the same as Experiment 1 except that the FBG was bonded onto a wind turbine blade instead of a PZT wafer. Additionally, a 1 cm x 1 cm piezoelectric patch was bonded using epoxy about 9 cm away from the FBG strain sensor.

A sweep sine from 0 to 100 kHz over 4 seconds at 10 V was input into the PZT in order to examine the frequency response of the system. The sampling rate was set at 500

kHz. In order to examine the impulse response of the turbine blade, an impulse (manually controlled impact) was input at the middle of the wind turbine blade. To better capture transient responses, the impact test was sampled at 1 MHz for 12 seconds.

Using a PZT patch (same as the PZT patch used in the sweep sine test), the impact test was repeated in order to serve as a comparison to the FBG sensor system.

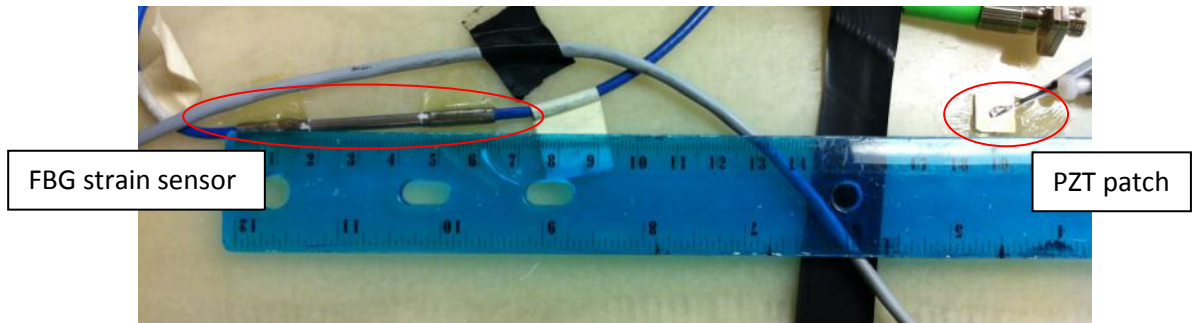


Figure 5-8. Relative location between the FBG and the PZT patch.

For both experiments, the reflection spectrums of all FBGs were uniform, and were not affected by the bonding conditions. The same data processing technique used in the first experiment was applied to results of the second experiment.

5.4.3. Simulation

Using Equations (5.12)- (5.14), the response of the FBG sensor system was simulated in MATLAB/Simulink. The data acquired from the previous impact tests were used to construct a second order transfer function describing the wind turbine blade. The parameters used for simulation were parameters $k = 0.5$, $A_{L,2} = 0.9$, $\Delta\lambda_B = 0.2$ nm, $P_0 = 0.0501$ W (17 dbm), and $\Delta\lambda_0 = 80$ nm.

5.5.Results

5.5.1. Experiment 1 – FBG sensor directly bonded to PZT actuator

As seen in Figure 5-9 and Figure 5-10, the sweep sine excitation caused a change in the DC component of the signal at many parts of the excitation. The response of the sensor system reached a maximum of about -0.7 V. This peak corresponded to the 18-23 kHz region in the frequency spectrum, which had a relatively raised power density. It was observed that violent shaking of the PZT wafer occurred during this frequency range. The rest of the sensor response was less eventful, with a few noticeable peaks in the 40 and 60 kHz ranges.

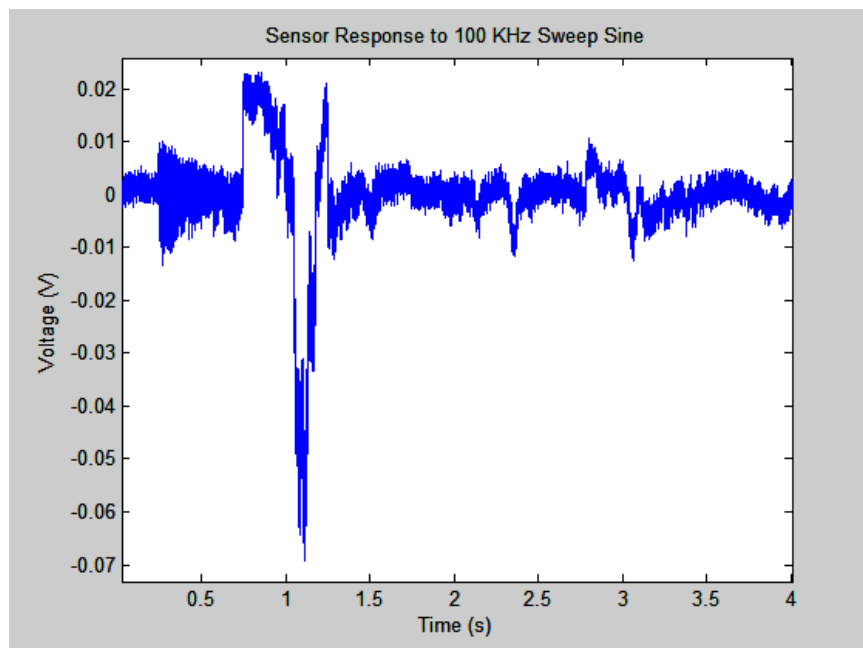


Figure 5-9 Time domain response of the FBG sensor to a sweep sine excitation (bonded to PZT wafer).

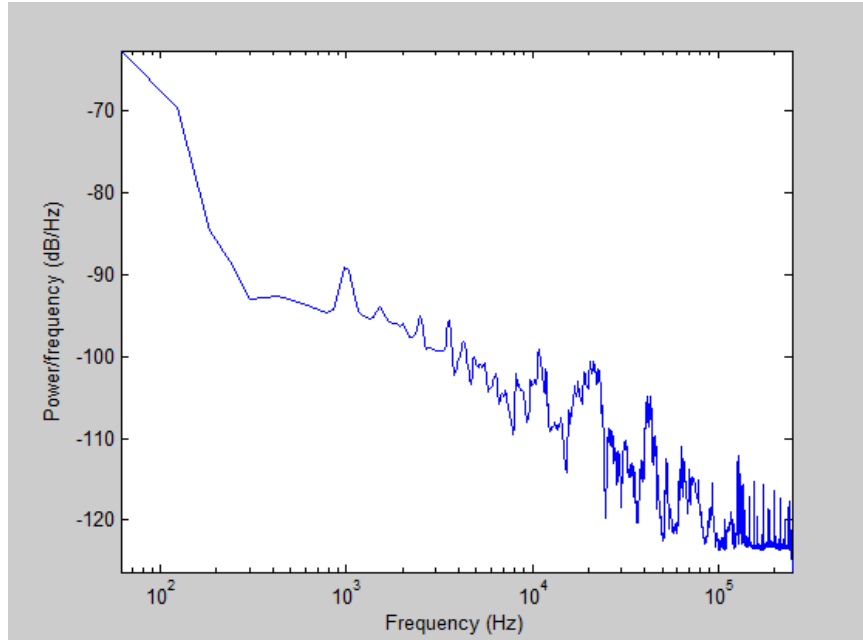


Figure 5-10. Power spectral density of the sweep sine response (bonded to PZT wafer).

5.5.2. Experiment 2 – FBG sensor bonded at a distance away from PZT actuator

5.5.2.1. Sweep Sine Test

From Figure 5-11 and Figure 5-12, the readings of the FBG system indicate the ability to sense the acoustic vibrations of the PZT despite the distance and the steel strain gauge housing. The frequency response across the excitation region was quite stable with minor fluctuation seen after 70 kHz. A multitude of frequency peaks are seen for the lower range of frequencies (<10kHz). Another noteworthy characteristic of the sweep sine response is a large peak at the 54 kHz frequency is seen in the power spectrum.

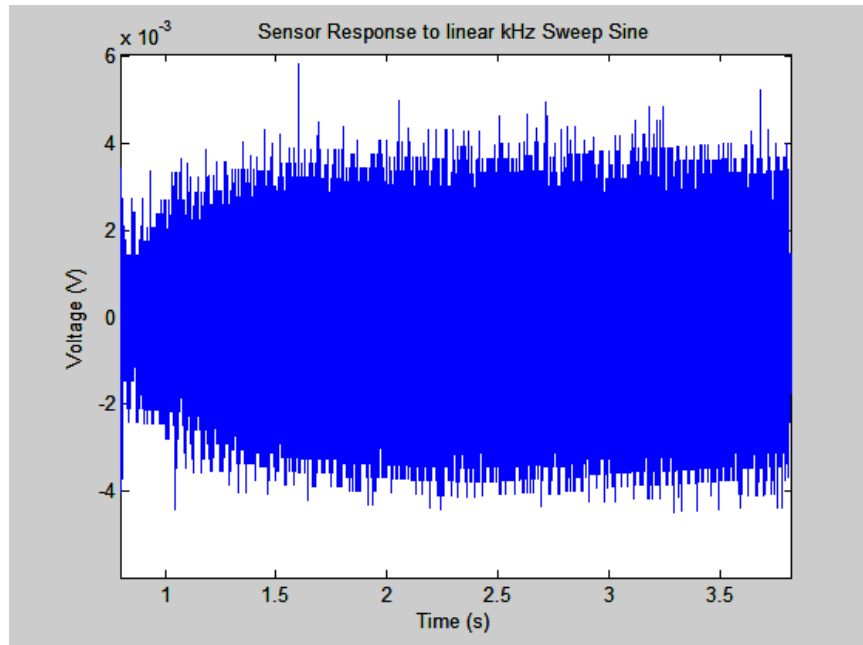


Figure 5-11. Initial portion of the sweep sine result.

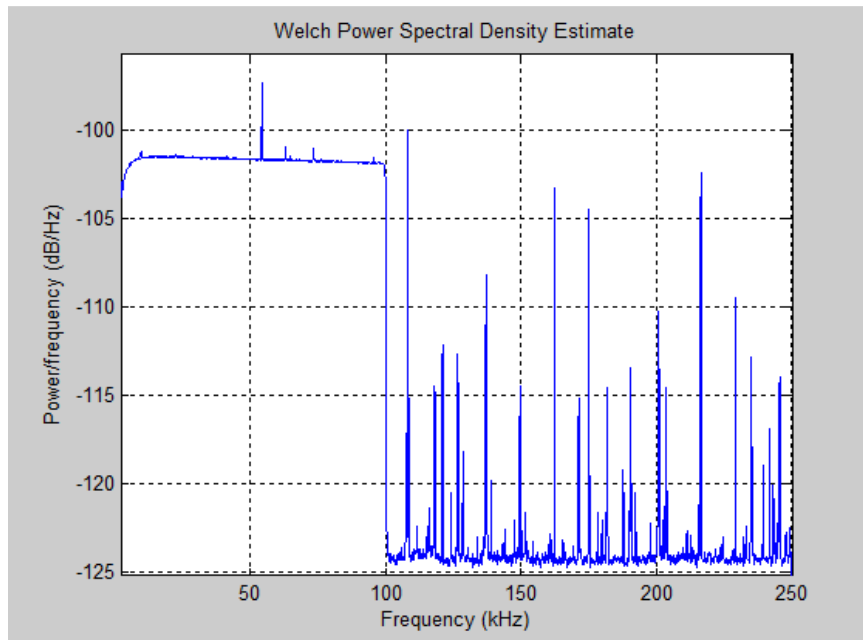


Figure 5-12. Power spectral density of sweep sine response.

5.5.2.2. Impact Test

During the impact test, the fundamental modes of the turbine blade were excited (the first three modes were measured at 5.96 Hz, 11.68 Hz and 17.6 Hz) (Figure 5-14). In

order to avoid artifacts created by saturation nonlinear effects, only the signals obtained from the linear region was used for frequency analysis. The turbine blade settled around 10 seconds after impact. During the initial 1.5 seconds, a small amount of saturation was observed (upper bound was 0.115 V, and the lower bound was -0.02 V) along with the nonlinear effects of entering the other lobe of the power profile (see Figure 5-5) before the vibrations gradually attenuated (Figure 5-13).

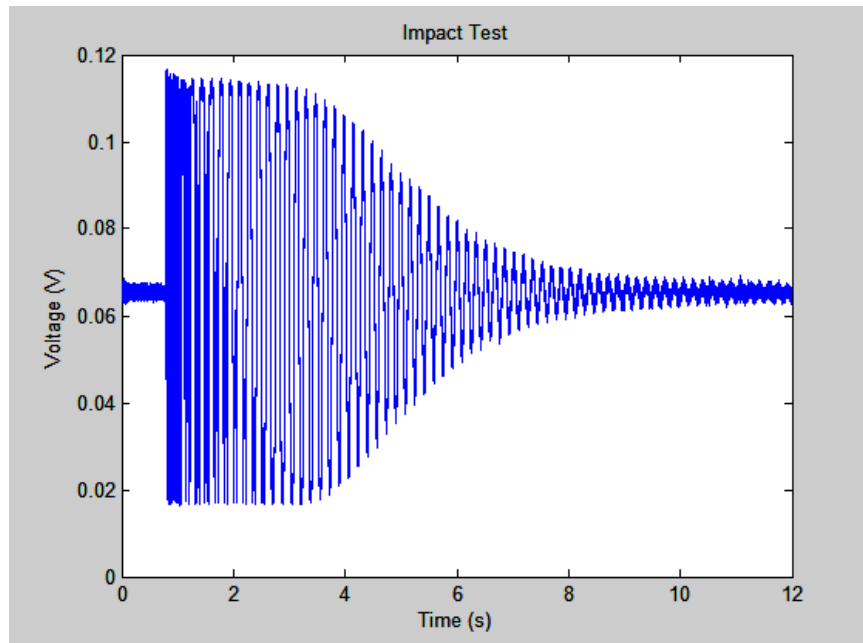


Figure 5-13. Impulse response of the turbine blade as sensed by the FBG sensor system.

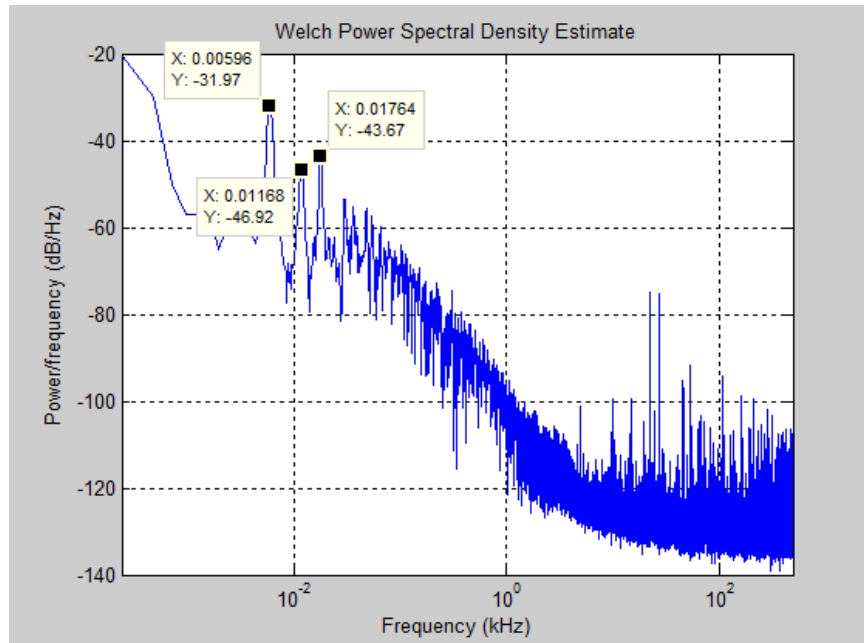


Figure 5-14. Dominant natural frequencies of the turbine blade as measured by the FBG sensor system.

Apart from the absence of saturation due to the wider sensing range (~ -1.1 V to 0.9 V) of the PZT patch, the other signal behaviors were similar with the FBG sensor system (Figure 5-15). The modes sensed by the PZT patch were identical to the first and third modes sensed by the FBG sensor system (5.96 Hz and 17.64 Hz), thus verifying the results obtained from the FBG sensor system (Figure 5-16).

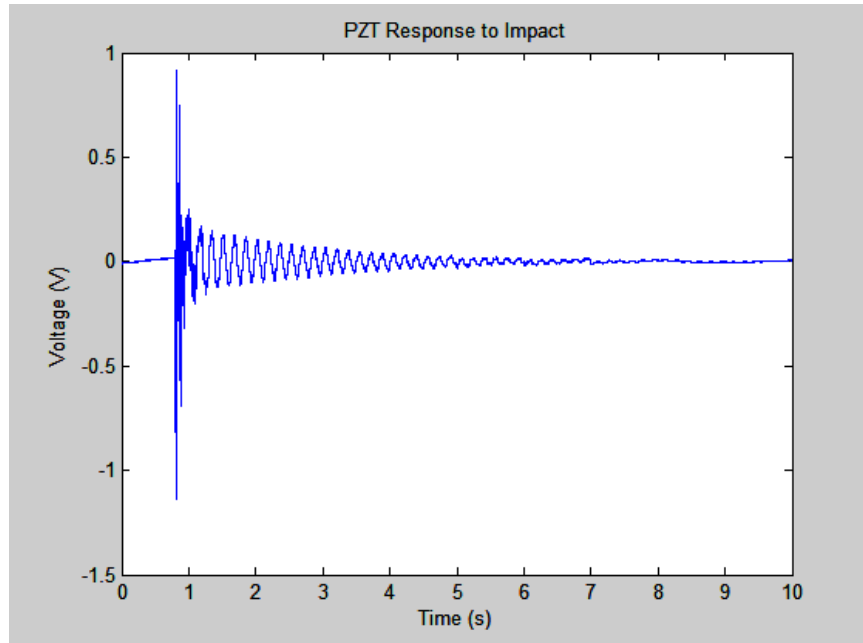


Figure 5-15. Impulse response of the turbine blade as sensed by the PZT patch.

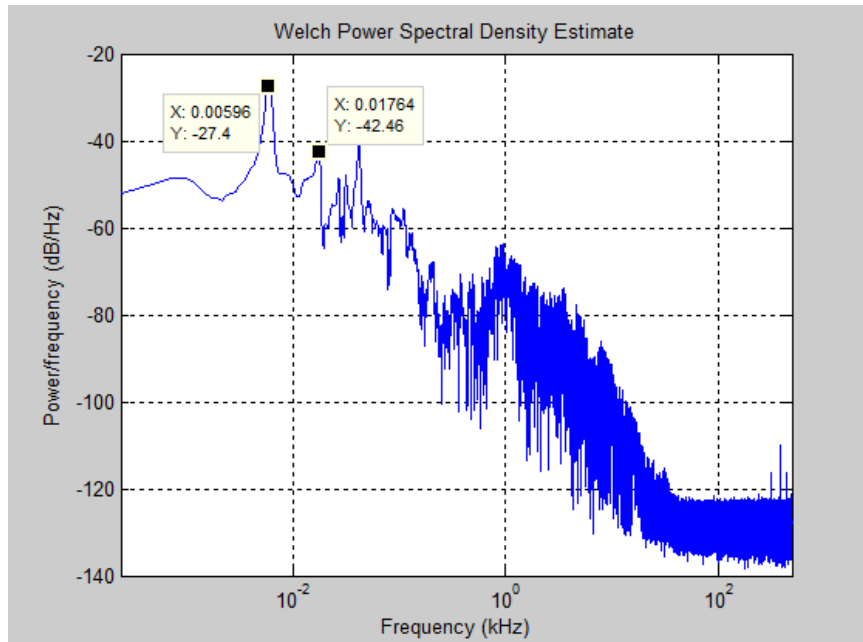


Figure 5-16. Natural frequencies of the turbine blade as measured by the PZT patch.

5.5.2.3. Simulation Results

Based on the impact test results, a second order approximation of the transfer function ($TF(s)$) with respect to strain of the sensor on the wind turbine blade is

$$TF(s) = \frac{\omega_n^2}{s^2 + 2\zeta\omega_n s + \omega_n^2} = \frac{1288}{s^2 + 1.27s + 1288}, \quad (5.15)$$

where the dominant natural frequency was 5.72 Hz (35.9 rad/s) and the damping ratio according to the log decrement method was 0.0178. The output of the transfer function was used as the strain input to the FBG sensor system model. The overall shape and the signal behavior closely matched that of the experimental impact test result. Differences include an approximately 0.01 V bias in the vibrating portion of the signal (i.e., the resting voltage was matched by introducing a bias in simulation, but the experimental results is weighted more positively). The bias was most severe in the beginning, but began to decrease as both simulation and experimental signals converged towards the resting voltage of 0.65 V. A closer inspection of the vibrations reveals a phase variation of the experimental data with respect to the simulation (Figure 5-18).

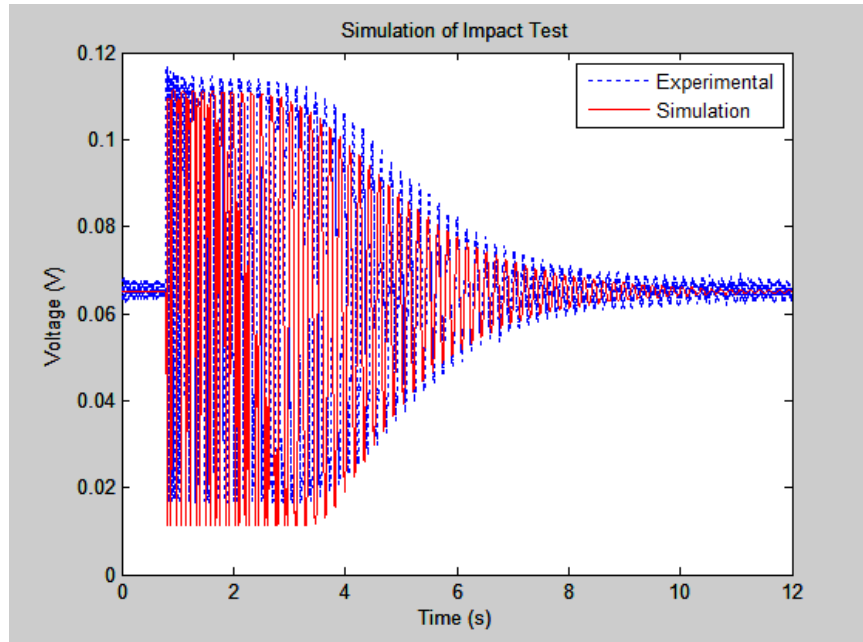


Figure 5-17 Comparison of the experimental and simulation results.

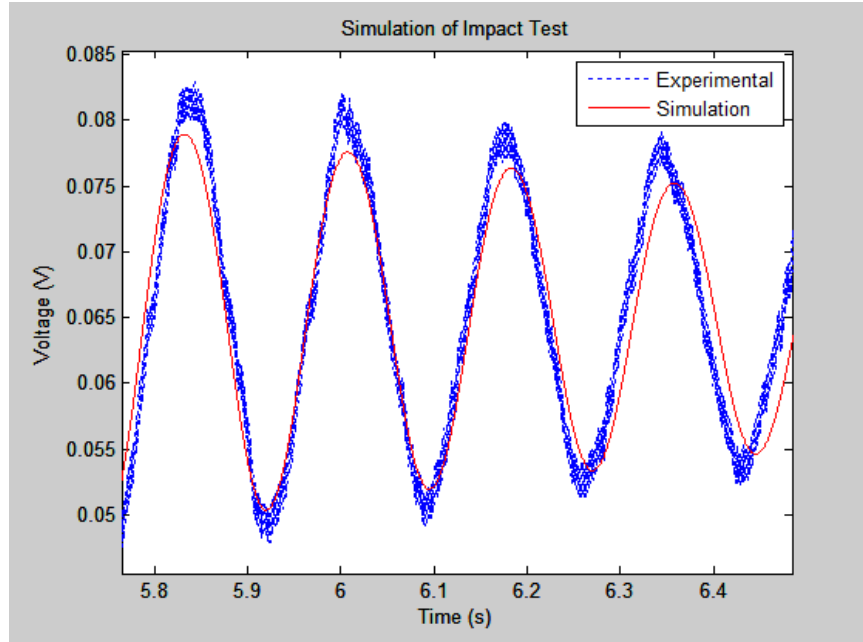


Figure 5-18. Zoom in of the data showing slight discrepancies between the results.

5.6.Discussion

The objective of the work in this chapter was the design and verification of an FBG-based sensor system able to measure dynamic signals without the use of expensive and sometimes bulky components such as optical scanners, spectrum analyzers, etc. Several tests were performed to demonstrate the ability of the sensor system to measure dynamic signals. As seen in the results, the sensor system was able to measure high frequency vibrations through the vibration induced optical power fluctuations observed by the photodetector.

In the first experiment, FBG1 was directly bonded to the PZT wafer. Unlike the corresponding portion of the second experiment, the sweep sine inputted into the PZT wafer did not produce a completely sine wave output from the sensor system, and instead introduced a bias at certain frequencies (18-23 kHz). The appearance of the bias suggests

an uneven bondage of the FBG on the PZT wafer or an uneven contraction of the PZT wafer along the bonded length of the FBG (i.e., the additional stiffness provided by the cyanoacrylate and the FBG on one side may have caused the contractions to favor one side over the other). On the other hand, since the FBG was directly bonded to the PZT wafer, the signals received were stronger than the signals in the second experiment.

Unlike the first experiment, the sensing FBG and the vibration sources were not only farther apart (9 cm), but were separated by different layers of material (surface, bonding agent, steel casing, etc.). During the second sweep sine test, the voltage measured from the resistor was one order magnitude smaller than what was observed in the first sweep sine test. However, the output shape and frequency response of the FBG system matched the sweep sine input transmitted by the PZT patch much more closely. The ability of the sensor system to measure such vibrations despite environmentally induced dampening effects (e.g., distance, material mismatch, etc.) implies the possibility of using the sensor system for structural health monitoring. Furthermore, interchangeability of system components grants the system mobility and adaptability, which are advantageous for field deployment. As such, any FBG sensor, even those already installed or embedded in the field, can be converted into a similar dynamic sensor system. For example, Song et al. have used smart aggregates to perform the health monitoring of various concrete structures [92, 93], and a concurrently installed FBG sensing system (see for example Chapter 4) may be used as a complementary acoustic wave sensor by selecting one of the FBGs and applying the set-up described in this chapter. The range of strain levels readable by the FBG sensing system, however, is

limited compared to the inherent strain sensing ability of the FBG sensors themselves ($>4000 \mu\epsilon$) [2].

As seen in Figure 5-14, some saturation can be seen at the beginning of the vibrations, where the amplitude of the vibrations did not exceed 0.02 and 0.11 V for the first 1.8 seconds after impact. In this scenario, the strain of the FBG caused enough of a wavelength mismatch that the power levels received at the photodiode swept between the two lobes of the profile as well as progressing into the flat regions seen in Figure 5-5. Noted in the results section were some differences between experimental and simulation results. These differences included a bias present during vibration and a phase variation in the experimental data. Factors that may account for the differences may arise from several areas. First, the Gaussian model utilized in the modeling is a simplification and idealization of the more complex FBG reflectivity profile. The actual FBG reflectivity profile may have imperfections due to manufacturing and installation conditions (e.g., profiles may be skewed, incompletely apodized, split, etc). Secondly, the transfer function of the turbine blade did not include the higher order dynamics than the turbine blade. Thus, the simulation would not have predicted the transient effects of higher order excitation that may have contributed to the phase variation.

On the other hand, by taking the power density spectrum of the linear portion of the signal, the dominant natural frequencies of the turbine blade could be discerned. A frequency analysis of the PZT response confirmed the measurements of the FBG sensor system.

The total cost of the system, not including the DAQ, the mount, and the computer, is less than \$3000 (including laser source, power supply, two FBGs, one coupler, and one photodiode). Traditional FBG wavelength interrogation schemes that employ special optical filters can raise the additional expenses about \$1000-\$2000. For commercially available interrogation packages, the costs may go up to \$10,000 per channel.

Future development of this FBG sensor system points toward the construction of a highly portable unit that can be adapted to existing FBG sensor installations. Although not directly discussed in this chapter, the FBG sensor system has the capability of being multiplexed. Multiplexing can be accomplished by repeating the set-up in series after FBG2. The main concern with multiplexing in this system is the attenuation of the optical power emitted from the laser source, the use of additional photodiodes, and the requirement for matching FBG center wavelengths. However, the use of low-attenuation coupling components (e.g., optical circulators) and high frequency electrical switches (for sampling between photodiodes using minimal DAQ channels) may help to mitigate such obstacles.

5.7. Conclusions

A new method for using wavelength matched FBGs in dynamic sensing was presented in this chapter. The theoretical investigation of this new sensor system revealed the dependence of the system's operating range on the FWHM of the FBGs and the optimal initial wavelength mismatch to maximize the range in which wavelength mismatch linearly correlates to photodiode power levels. Subsequently, experimental results verified the ability the system in measuring high frequency vibrations (up 100 kHz was measured).

Chapter 6 Fiber Grating Sensor Network for the Structural Health Monitoring of a Medium Scale Grout Structure

6.1.Introduction and Literature Review of FBGs in Structural Health Monitoring

Civil infrastructures are vital to the function of society and are present in all modern civilization. The wellbeing of, and even the identity and culture of a society is heavily dependent on its infrastructure. Any malfunction of the infrastructure can lead to serious consequences, whether in regards to human life, to the environment, or to the economy. Thus, it is imperative that civil structures be well maintained and regularly checked for potential problems. Problems in civil structures can originate from many sources. As structures are built and used, they are continuously subjected to loading. Whether the loading originates from environmental (e.g., storms) or from intended (e.g., people) sources, the structural integrity will be taxed. By monitoring whether the structural integrity has been compromised from such loads, we can maximize the time for which the structure has continued function and safety. Thus, the need for the continuous inspection of a structure's integrity has given rise to the field of structural health monitoring (SHM). The following overview of SHM will serve as a general background for chapter four and chapter five, both of which focus on the use of FBGs for SHM.

Structural health monitoring (SHM) involves the measurement of critical parameters such as strain at strategic locations within a structure for the purposes of detecting any structural anomaly that suggests the onset of failure [94]. The parameters relevant to structural integrity can be divided into mechanical, physical, and chemical types, as seen in Table 6-1 [95]. For the purposes of this dissertation, only mechanical and physical parameters will be considered.

Table 6-1. Parameters relevant to SHM [95]

Type	Example Parameters
Mechanical	Strain, displacement, cracks, stress, loading
Physical	Temperature, humidity, pore pressure
Chemical	Chloride, sulfate, and carbonation penetration, pH, oxidation of rebar and steel, wood decay

Recently, fiber optic sensors have been popularly used as an instrument for measuring the needed parameters for SHM. Fiber optic sensors possess excellent properties, such as high resolution, electromagnetic immunity, and small size, which are suitable for applications in SHM. In particular are fiber Bragg gratings (FBGs) which are intrinsic, wavelength based sensors that are robust against power fluctuations within the optical cable. Along with the ability to be multiplexed and comparatively lower costs, FBGs are becoming a prominent fiber-optic based sensor for SHM [96, 97].

For the use of FBGs in civil structures, one must first address the fragility of fiber optic cables with respect to the environment. Large forces and the requirement for long service times necessitate protective measures for the FBG sensor. Some examples of protected FBG sensors for the measurement of strain can be found in the literature. A number of FBG strain sensors consist of a bare FBG enclosed by a narrow steel or fiber reinforced plastic (FRP) cylinder, often with mounting discs or brackets at either end of the cylinder as the indicator for the gauge length [98, 99, 100]. The FBG is bonded to the enclosure at each end. The relative deformation between the mounting parts at both ends of the cylinder produces a uniform strain along the FBG sensor. Such enclosed FBG strain sensors may be embedded or mounted on the surface of a structure.

Other encapsulation methods involve using certain parts of the structure itself as protection. For example, Chung and Kang through the use of epoxy installed multiplexed FBGs within a groove made along the length of a rebar [101]. However, cases in which the FBG is directly bonded to the host structure, the sensors should be recalibrated for accuracy due to coupling-induced changes in sensitivity [96].

Some situations in which the structure to be monitored may discourage or even preclude the installation of such enclosed FBG sensors. For instance, structures made of certain materials such as glass fiber reinforced plastic may not lend themselves to the direct embedment of enclosed FBG sensors without disruption in either the construction process or the structural integrity after construction. Researchers have undertaken an effort to allow the use of FBG strain sensors for structures made of such materials. Dawood et al. described a procedure in which FBG sensors could be safely embedded into foam core GFRP sandwich composite material using the vacuum infusion process. Verification tests showed repeatability and accuracy of the FBG sensors in measuring strain after embedment [102].

On the other hand, as mentioned in Chapter 2, FBGs exhibit cross sensitivity between strain and temperature, and this cross sensitivity can be a source of problems when the operator only wants to measure only strain or only temperature. The cross sensitivity can be compensated in a variety of ways. In one method, the encapsulation of a strain sensing FBG is design so that the thermal expansion of the FBG and the encapsulation cancel each other out, thus compensating for thermal drift [103]. Alternatively, strain-free FBGs can be placed near FBG strain sensors in order to compensate any temperature-induced wavelength shifts of the strain sensors. Like the

strain sensors, the temperature sensors must also be protected from the environment. Moyo et al. devised a temperature compensated strain sensor through the assembly of two FBGs into a dumb-bell shaped package. Within the package, a strain-free FBG sensor is protected by a metal tube while the FBG strain sensor placed next to it is coupled to the package, thus receiving any strain experienced by the package [104].

The strain and temperature sensing methods discussed in the above form a basis in which FBGs are applied for the SHM of civil structures. Some examples of FBG in SHM include the installation of FBG strain sensors for the monitoring of the Tsing Ma Bridge in Hong Kong [106], and the all-fiber reinforced composite West Mill Bridge [107]. Many other instances of FBG-enabled SHM of civil structures exist in the literature, showing the increasing prevalence of FBG in SHM [96, 97, 100, 108-112]. In the next section, a brief discussion will be given regarding the FBG sensors that were used for both chapter four and chapter five.

6.1.1. Strain sensors

The FBG strain sensors used in the following SHM-related chapters utilize a similar enclosure principle as described in the previous section. A schematic of the strain sensor is shown in Figure 6-1 [113].

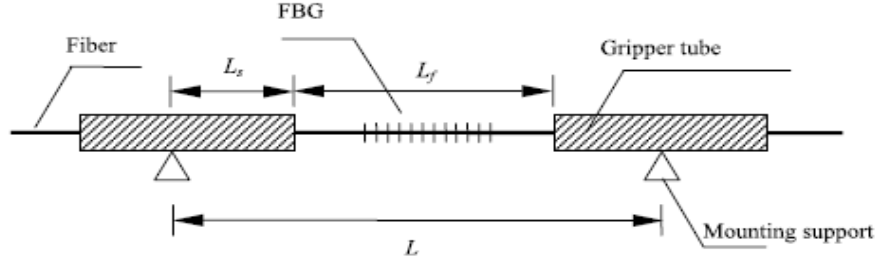


Figure 6-1. Schematic of FBG strain sensor.

The sensor consists of a fiber optic passing through two gripper tubes with the FBG sensing portion centered between the tubes. Epoxy resin is used to bond the FBG to both gripper tubes. As the tubes move relative to each other, the FBG will experience strain. Since the FBG sensing portion is not directly bonded, the problem of split peaks due to nonuniform bonding is avoided [113, 114]. The relationship between the strain of the FBG and the deformation of the strain sensor enclosure becomes that of a beam being longitudinally deformed. The relevant equations are [113]

$$\Delta L_g = \frac{P_g L_g}{E_g A_g}, \quad (6.1)$$

$$\Delta L_f = \frac{P_f L_f}{E_f A_f}, \quad (6.2)$$

where the subscripts g and f refer to the gripper tube and the FBG, respectively; A is the cross sectional area, L is the length (fiber and distance between mounting supports), E is the young's modulus, and P is the tension acting on the gripper tube and the fiber. With $P_f = P_g$, the strain ratio between the fiber and the gripper tube becomes [113],

$$\frac{\varepsilon_g}{\varepsilon_f} = \frac{\Delta L_g / L_g}{\Delta L_f / L_f} = \frac{E_f A_f}{E_g A_g} \quad (6.3)$$

Assuming $E_f = 72 \times 10^9$ Pa, $E_g = 210 \times 10^9$ Pa, $A_f = 0.00196 \text{ mm}^2$, $A_g = 0.0804 \text{ mm}^2$,

the strain ratio becomes $\frac{\varepsilon_g}{\varepsilon_f} = 0.0084$, indicating that the fiber bears most of the strain in

the strain sensor assembly. The center wavelength of the FBG shifts according to the following relationship [113]:

$$\varepsilon = \frac{L_f}{L} \varepsilon_f = \frac{L_f \Delta \lambda_B}{1.2L} \quad (6.4)$$

Thus, the strain sensitivity of the FBG strain sensor depends on the ratio between L and L_f .

The relationship between strain and wavelength change is linear for FBGs (shown in the appendix is an example of the calibration of a FBG strain sensor). However, when encased in a protective package as is the case for the FBG strain sensor, some nonlinear regions or saturation may occur due to the properties of the package. For the FBG strain sensor packaging based on Figure 6-1, some pretension, either in the fiber or in the package, may be required to ensure that the sensor operates in the linear region. The pretension is especially required if the structure hosting the sensor will undergo equal amounts of tension and compression. Usually, a positive wavelength shift of 0.5 nm is adequate.

6.1.2. Temperature sensors

The design of an FBG temperature sensor must prevent the FBG sensing portion from receiving any strain from the environment while simultaneously protecting the FBG from damage. Figure 6-2 is a schematic of the temperature sensors used in the proceeding chapters [115].

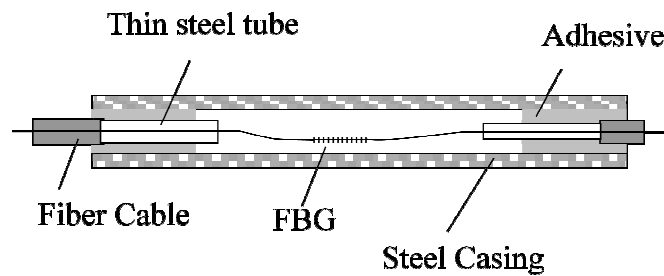


Figure 6-2. Schematic of FBG temperature sensor.

As seen in Figure 6-2, the fiber cable passes through a protective steel casing and steel tubing on both ends of the sensor package. Since the FBG is not bonded to anything, strains from the environment will not interfere with the temperature readings of the FBG. Without the mechanical coupling effect, the thermal sensitivity of the FBG remains unaffected ($13.7 \text{ pm}/^{\circ}\text{C}$). However, it is expected that the packing material and the air cavity surrounding the FBG inside the package may act as a thermal insulator and thus causes the FBG temperature sensor to have a small delay. However, for most cases in SHM applications, thermal fluctuations are generated by the weather and delay will be insignificant compared to the slow rate of change in the ambient temperature.

6.1.3. Water sensors

Another important aspect regarding the continued health of civil structures, with concrete structures in particular is the invasion of water within the walls and supporting skeleton of the structure. Water and any chemical agents carried by the water can cause corrosion that can severely compromise structural integrity. Figure 6-3 is the schematic of a FBG-based water sensor [116].

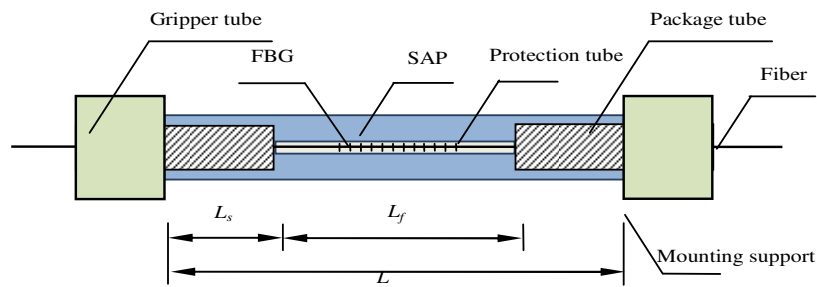


Figure 6-3. Schematic of FBG water sensor.

Similar to the FBG temperature sensor, the FBG sensor within the package should be strain-relieved with respect to the surroundings. Within the package, the FBG sensor is coated with super absorbent polymer (SAP) that swells up several times its size when exposed to liquid water. A thin layer of water permeable material prevents the SAP from spilling out of the package and at the same time maximizes the strain induced by the swelling of the SAP. The expansion of the SAP induces a strain on the FBG, thus indicating the presence of water. This design was the precursor of the sensor described in chapter four, with the difference being that this precursor design is only able to perform for one loading cycle.

6.2.Application of FBGs in the SHM of Nuclear Containment Facilities

All structures at the end of their functional lifetimes require either rehabilitation to renew their usage, or shut down and deconstruction. For structures containing substances that may harm the local environment and population, this end-of-life closure process becomes important. In particular are nuclear power plants or other nuclear containment structures, which have special decommissioning procedures in order to minimize the possibility of radioactive contamination of the structures local area. Three internationally accepted decommissioning options include immediate dismantlement (DECON), safe enclosure (SAFSTOR), and entombment (ENTOMB). In immediate dismantlement, parts of the facility that contained radioactive agents are either removed or decontaminated to acceptable levels. The rest of the structure can then be recycled safely for other uses. In the case of safe enclosure, the dismantlement of the facility is delayed until the radioactive components have decayed to allowable levels (within 40-60 years). Meanwhile, the facility is closely monitored and maintained. Finally, in entombment, the facility is permanently encased in a durable material such as concrete and continuously monitored until radiation levels have dropped sufficiently [117, 118].

In the case of safe enclosure and entombment, long-term monitoring of the nuclear facility is required. The walls of the facility and the possible enclosing shell function to barricade the contents of the plant from harming the environment. Constant monitoring of the containment walls will be beneficial in knowing structural integrity has been compromised and if corrective action should be taken. Sensors that can simultaneously function efficiently while embedded within a structure and at the same

time not affect the structural integrity appreciably will be desirable for the enablement of SHM in such scenarios.

Various types of fiber optic sensors have been applied to nuclear power industry in general, however the amount of documented cases of such application is limited perhaps due to the relative youth of both the nuclear power industry and the fiber optics. Extrinsic fiber optic sensors applied in the nuclear power industry include Raman spectroscopy for the measurement of hydrogen levels [119] and luminescence-based sensors for the measurement of radiation levels [120]. Intrinsic sensors include interferometric sensors for the measurement of voltage and current [121, 122, 123] and Bragg grating-based sensors for the measurement of strain, displacement, pressure, and temperature. All of the above measurement parameters can be applied to different vital parts of a nuclear power plant. For example, surface mounted FBG-based extensometers were used to monitor the thick concrete nuclear shield of a reactor [124]. The steam pipe system of a nuclear power plant serves to regulate temperature of reactors. In order to prevent boiling, the water inside the pipes is kept under high pressure, and such high pressure leads to vulnerable areas in the joints of the piping system. Temperature compensated FBGs were used to monitor the local strains of the vulnerable spots [124]. Finally, FBGs were proposed to be used to monitor the strain and temperature of repositories designed to contain nuclear wastes [124]. The lack of literature regarding fiber optic sensors (FBGs in particular) for use in nuclear facilities further show the youth of the research in the use of FBGs for SHM in the nuclear industry.

In the following experiment, a distributed FBG sensor network was used to monitor a medium-scale grout structure that emulates the wall of a nuclear containment structure.

6.2.1. Sensors

Strain, water, and temperature FBG sensors were used in the experiment (Table 6-2). Strain sensors were comprised of bare FBGs encapsulated within a thin, stainless-steel cylinder. Loads experienced by the cylinder are measured as strain by the FBG. Water sensors were assembled by coating the FBG with a layer of SAP. A calibration test of the water sensor indicated a shift of 0.1 nm suggested the presence of water in the sensor. Each water sensor was encased within a small grout enclosure to prevent the unintended detection of the hydration during the initial grout pouring and curing process.

In order to compensate for the cross sensitivity of FBGs between strain and temperature, strain relieved FBGs were planted alongside the other sensors to act as temperature sensors. As a method of temperature compensation, the wavelength shift of the temperature sensors were subtracted from the wavelength of the other sensors.

6.2.1.1. Calibration

The responses from each sensor were characterized prior to deployment and were used for sensor calibration. Strain sensor calibration consisted of mounting the sensor on an aluminum beam and recording the wavelength change as loads increased at the end of the beam. Temperature sensors were calibrated by submersing the sensor in a temperature controlled water bath and recording wavelength change as the temperature changed. Figure 6-4 shows the calibration set up for strain and temperature sensors.

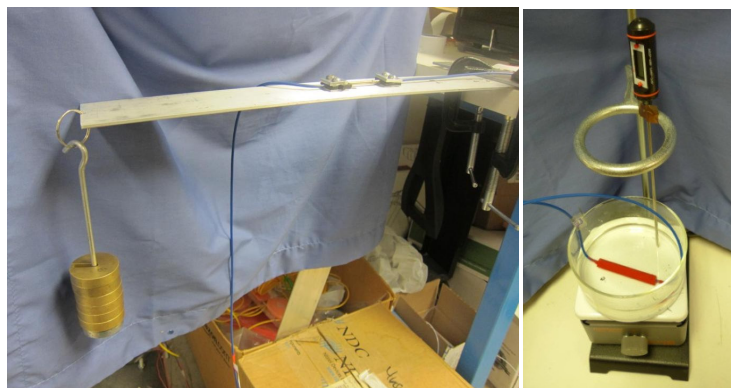


Figure 6-4. Calibration for FBG sensors (Left) Strain sensor, (Right) Temperature sensor.

Water sensors did not require calibration. However, their response to an input volume of water (<0.5 mL) was examined. A 0.1-0.15 nm wavelength shift was established as an indicator for the presence of water (Figure 6-5).

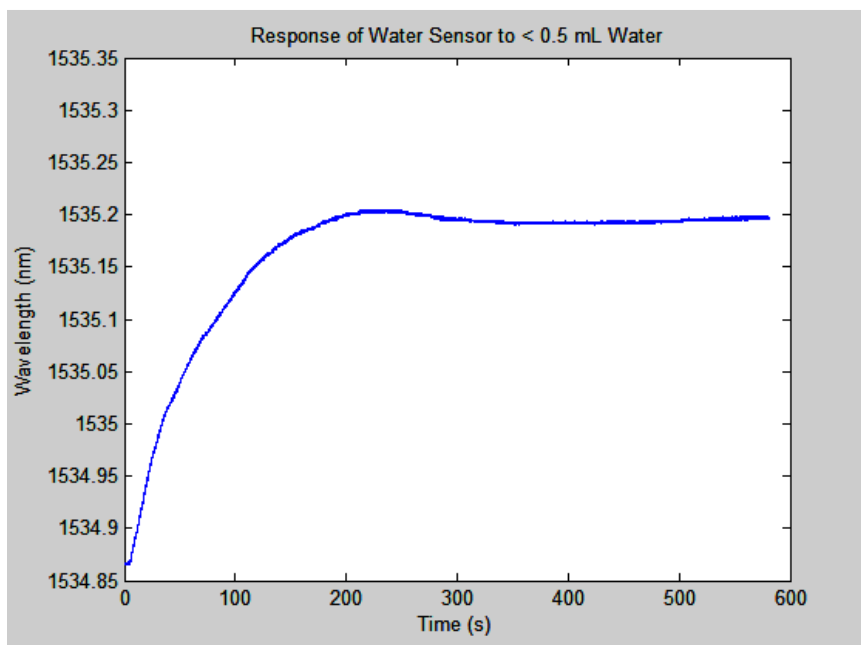

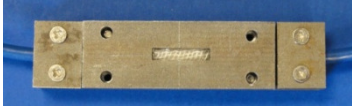



Figure 6-5. Response of water sensor to <0.5 mL volume of water.

Examples of the calibration data and equations are available in the appendix.

Table 6-2 Sensors used during the SHM experiment.

Type	Picture	Size (inch)	Weight (oz)
Temperature		2.8 x 0.42 x 0.18	0.9
Water		2.4 x 0.55 x 0.35	1.85
Strain		Diameter: 0.15 Length: 7.2	0.6

6.2.2. Experimental Setup

6.2.2.1. Test Structure

A 10 ft x 10 ft x 10 ft grout cube was constructed using grout. Nine 8 ft x 10 ft barred (0.5 in diameter) panels for sensor installation were embedded at equal intervals of 1ft within the cube (Figure 6-6 Left). The panels are labeled from P1 to P9, each containing 9 vertical steel rods for supporting sensors (Figure 6-6 Right).

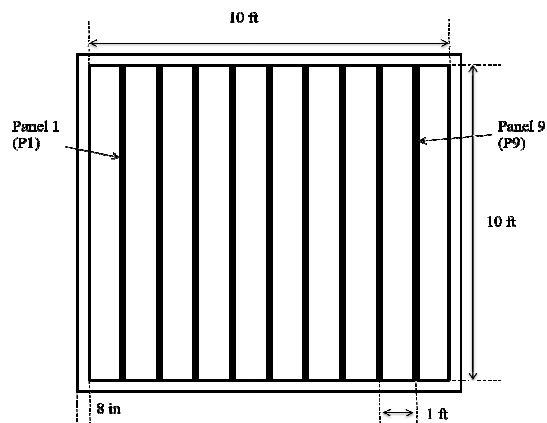


Figure 6-6 (Left) Top-down view of grout cube schematic, (Right) Photo of sensor panel.

6.2.2.2. Sensor Installation

A total of eight strain sensors, eight water sensors, and eight temperature sensors were installed in the grout cube. The sensors were grouped into clusters of three (total of eight clusters), each cluster containing one strain sensor, one water sensor, and one temperature sensor (Figure 6-7 Right). Each strain sensor was prestrained to have about a positive wavelength shift of 0.5 nm. All sensors were multiplexed into one of four branches. Care was taken to prevent overlap of FBG wavelengths within a branch. However, each sensor had connection cables reaching out of the grout cube, thus allowing for easy interchangeability in the sequence of FBG sensors along or between branches. A four channel interrogator (sm130, Micron Optics) interfaced with ENLIGHT software was used to acquire data from each of the four branches (1 Hz sampling frequency) (Figure 6-7 Left). Grout was poured on January 13, and data was acquired from January 17 to March 3, 2012.

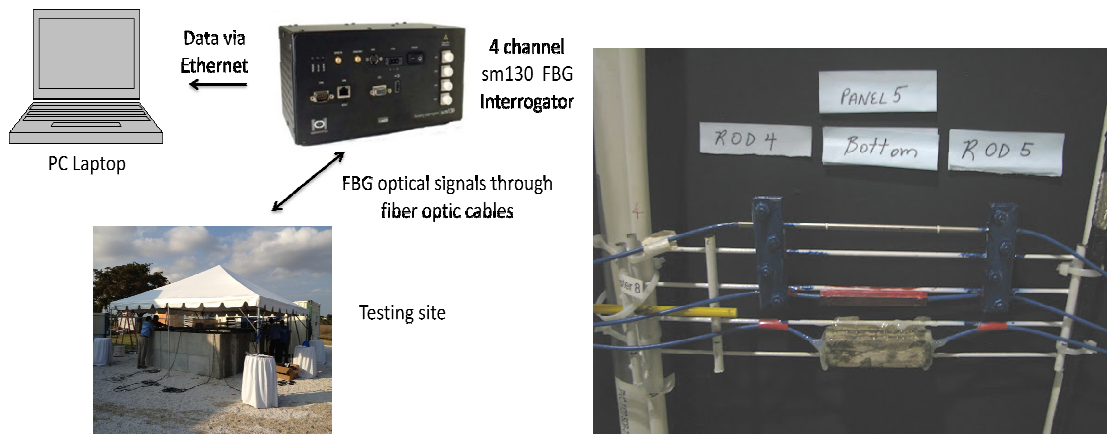


Figure 6-7 (Left) Sensor and data acquisition system configuration. (Right) Example of sensor cluster (Panel 5).

Figure 6-8 shows the installation location of each cluster throughout the grout cube. Table 6-3 summarizes the location of each sensor throughout the cube.

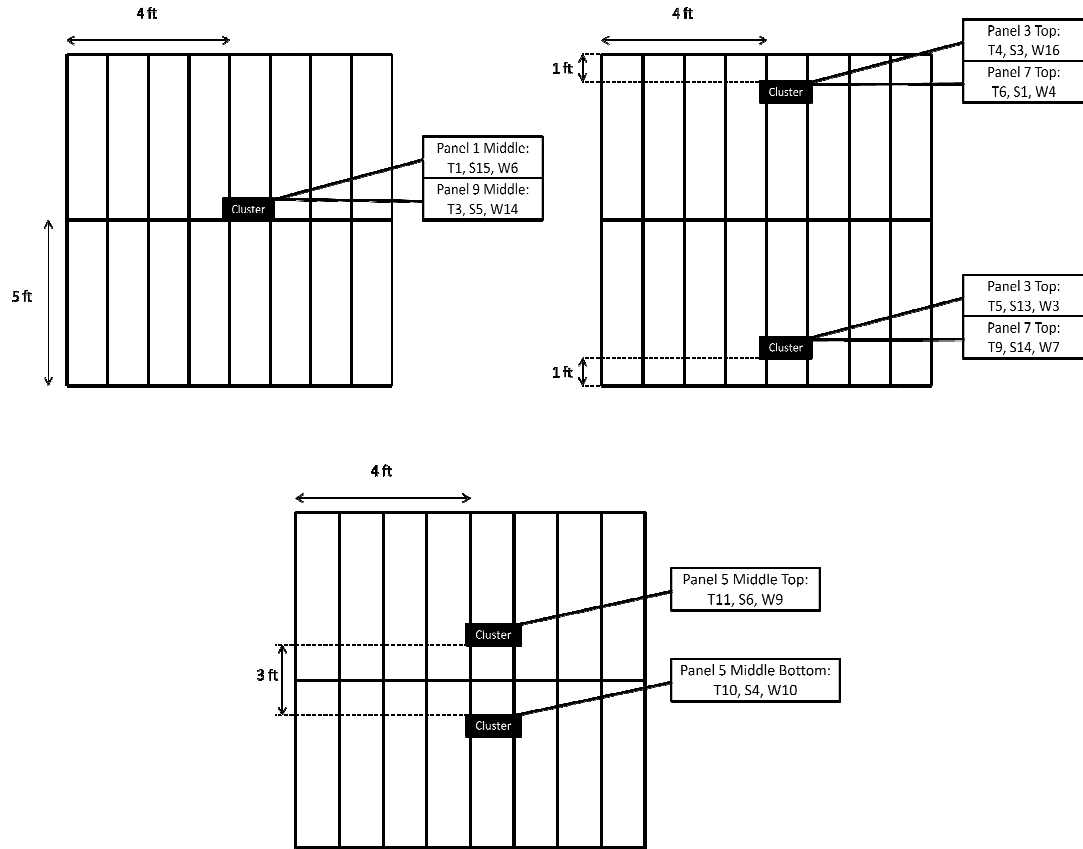


Figure 6-8 (Top Left) Panels 1 and 9 sensor cluster placement. (Top Right) Panels 3 and 7 sensor cluster placement (Bottom) Panel 5 sensor cluster placement.

Table 6-3 Summarization of sensor placement throughout sensor network and grout cube.

Channel 1			Channel 2		
Sensor #	λ (nm)	Location	Sensor #	λ (nm)	Location
T1	1541	P1 Middle	S5	1537	P9 Middle
S15	1546	P1 Middle	S13	1547	P3 Bottom
T3	1550	P9 Middle	S3	1559	P3 Top
T4	1553	P3 Top	T10	1588	P5 Middle Bottom
T5	1556	P3 Bottom	S1 (<i>inactive</i>)	1550	P7 Top
T6	1562	P7 Top			
T11	1585	P5 Middle Top			
T9	1587	P7 Bottom			
Channel 3			Channel 4		
Sensor #	λ (nm)	Location	Sensor #	λ (nm)	Location
W3	1535	P3 Bottom	W4	1538	P7 Top
W6	1542	P1 Middle	W7	1544	P7 Bottom
S6	1546	P5 Middle Top	W9	1546	P5 Middle Top
S4	1550	P5 Middle Bottom	W13	1562	P5 Middle Bottom
W14	1562	P9 Middle			
W16	1565	P3 Top			
S14	1573	P7 Bottom			
T = Temperature; S = Strain; W = Water; P = Panel; λ = Center Wavelength Sensors arranged in ascending order based on wavelength.					

Sensor strength was monitored periodically, and data acquisition settings were modified (e.g., digital gain adjustment) to ensure continuous function. Data corrections were made whenever gain adjustment caused artifacts in the measurements.

6.2.3. Results

6.2.3.1. Strain Sensor Results

Following the pouring of the grout, seven of the eight strain sensors continued to produce signal (P7 top lost signal). The strain measured at each of the seven locations decreased (corresponding to compression) until about Jan. 25, after which the rate of compression slowed down (Figure 6-9 and Figure 6-10).

From Feb. 17 until Mar. 3, about eight negative peaks (peaking before returning to original levels) of strain were observed in the Panel 3 bottom strain sensor. From Feb. 26 to Feb. 28, two downward peaks in strain were observed for Panel 5 middle-top (~ -10 microstrain each) and Panel 5 middle-bottom (~ -4 and -10 microstrain).

Small oscillations corresponding to daily thermal cycling were seen in the signals of most of the strain sensors. The strain sensors at Panel 7 bottom (Jan. 30) and Panel 3 top (Feb. 18 to Feb. 23) temporarily lost signal before going back online, thus causing brief discontinuities in the signal.

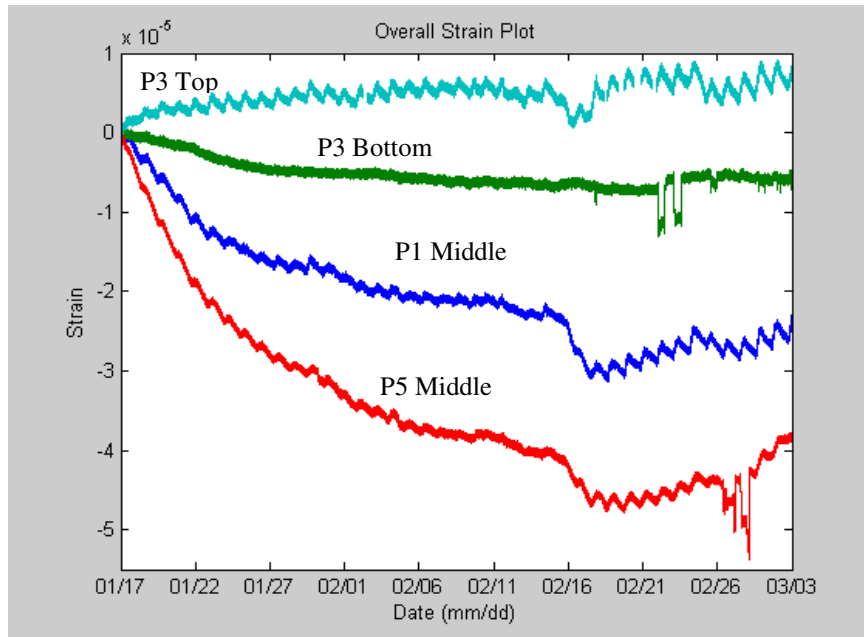


Figure 6-9 Strain sensor results from January 17 to March 3, 2012 (Panels 1, 3, 5).

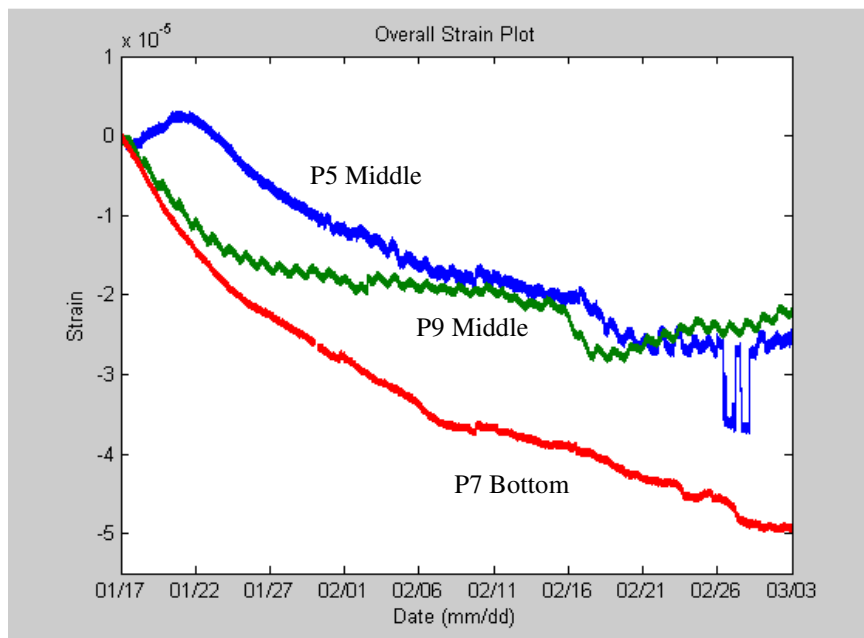


Figure 6-10 Strain sensor results from January 17 to March 3, 2012 (Panels 5, 7, 9).

6.2.3.2. Temperature Sensor Results

The temperature sensor measurements indicate a general downward trend starting from the beginning of data acquisition and sloping towards a steady state reading approximately after Jan. 25. From the overall temperature plots (Figure 6-11 and Figure 6-12), sensors placed near the top of the cube experienced the most oscillations, while sensors embedded deeper in the cube showed little signs of such oscillations. The temperature sensors near the top were the most sharply affected ($\sim 5^\circ\text{C}$ drop), followed by sensors embedded lower in the cube (2°C drop in the middle of Panels 1 and 9; 3°C drop in the bottom of Panel 7; 0°C drop elsewhere).

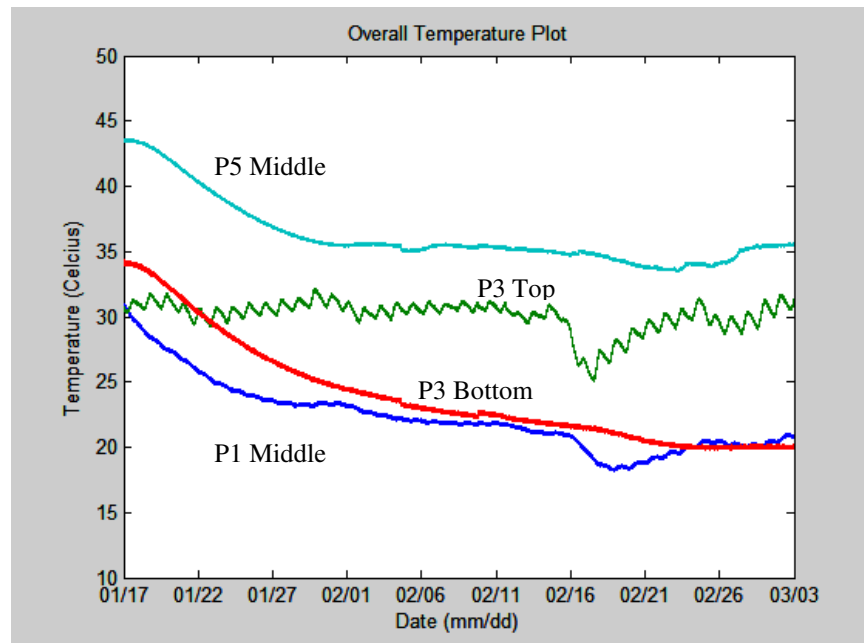


Figure 6-11 Temperature sensor results from January 17 to March 3, 2012 (Panels 1, 3, 5).

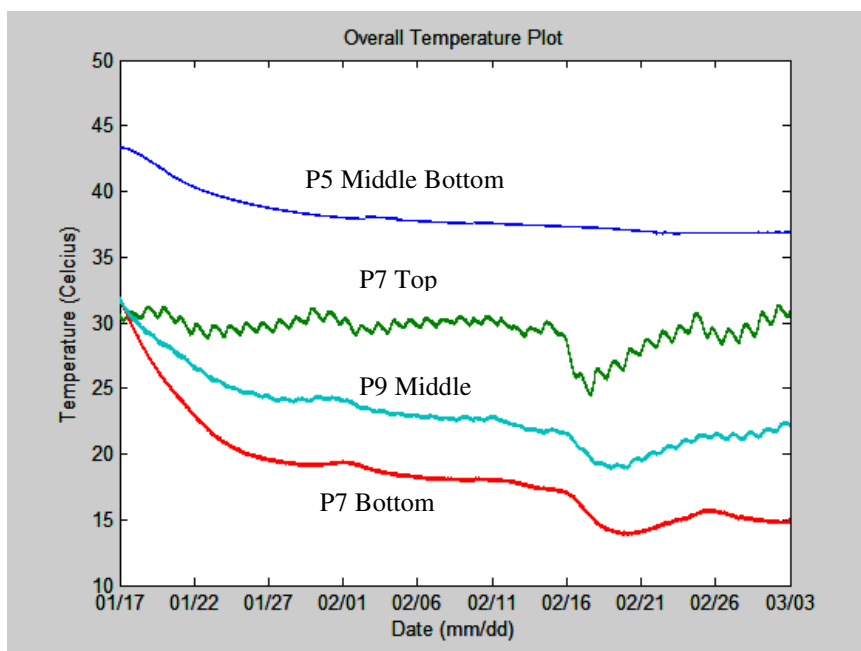


Figure 6-12 Temperature sensor results from January 17 to March 3, 2012 (Panels 5, 7, 9).

In regards to temperature values during steady state, the sensors in the center of the cube indicated elevated temperatures ($\sim 37 - 40^{\circ}\text{C}$). This is followed by the sensors in top of the cube ($\sim 29 - 31^{\circ}\text{C}$). The lowest temperatures were recorded in the middle of Panel 1 ($\sim 20 - 23^{\circ}\text{C}$) and Panel 9 ($\sim 21 - 24^{\circ}\text{C}$), and on the bottoms of Panel 3 ($20 - 23^{\circ}\text{C}$) and Panel 7 ($\sim 15 - 17^{\circ}\text{C}$).

6.2.3.3. Water Sensor Results

Water sensors at Panel 5 middle top (\sim Jan. 20), Panel 1 Middle (Feb. 1), Panel 3 top (Jan. 30), and Panel 7 top (Jan. 24) showed signs of water presence (Figure 6-13 and Figure 6-14) due to a shift in wavelength greater than 0.1 nm. Most noticeably, the water sensor near panel 3 top continued to increase for the duration of the experiment. On Feb 26 to Feb. 28, the water sensor near the top of Panel 7 had a negative peak before rising

back to previous levels. The signals from the water sensor of Panel 1 middle lost signal periodically, but was brought back by increasing the gain.

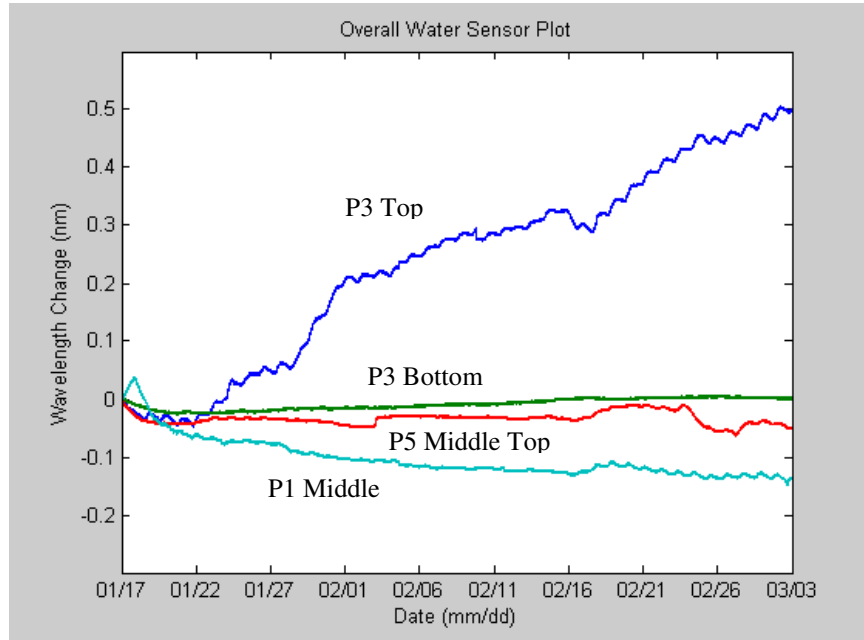


Figure 6-13 Water sensor results from January 17 to March 3, 2012 (Panels 1, 3, 5).

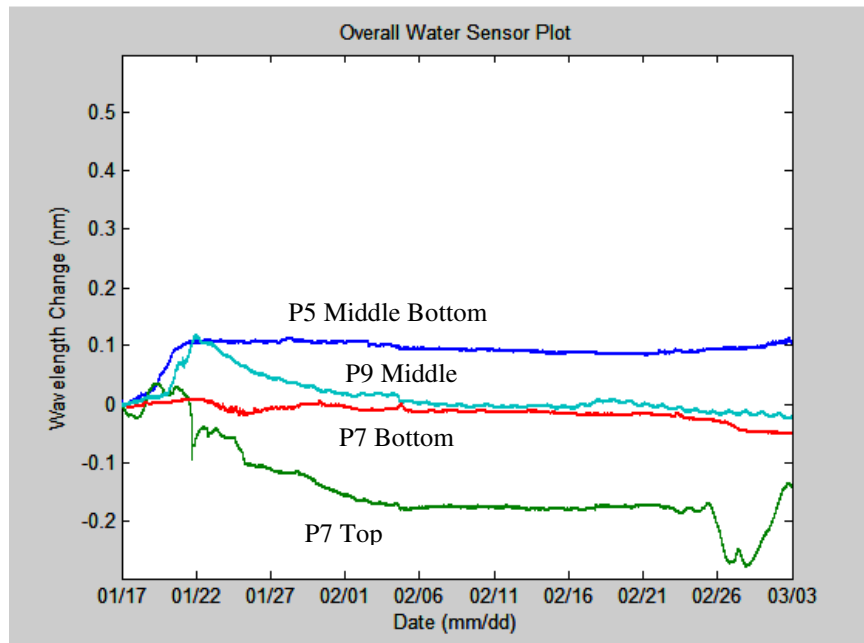


Figure 6-14 Water sensor results from January 17 to March 3, 2012 (Panels 5, 7, 9).

6.2.4. Discussion

6.2.4.1. Temperature sensors

Results show an intuitive picture of the temperature profile within the grout cube throughout the data acquisition time period. Temperatures at the top were closer to the atmosphere and thus experienced more oscillations due to the natural thermal variations associated with sunrise and sunset.

6.2.4.2. Strain sensors

The peaks mentioned in the results are most likely the result of cracking around the sensors. However, based on the magnitude of the change (less than 1.2 microstrain), any amount of cracking would be small. The two negative-strain peaks observed in Panel 3 bottom (Feb. 21-23) later appeared in similar form at Panel 5 middle top and middle bottom (Feb. 26-28) (Figure 6-9 and Figure 6-10). This replication may be indicative of crack propagation from the bottom of Panel 3 to the middle of Panel 5 over the period of several days.

In addition to crack-related strain readings, higher frequency small oscillations in strain appeared throughout the observation period. The oscillations are in-sync with the oscillations seen in the temperature sensors, indicating that the strain oscillations are caused by temperature changes. Based on the overall small scale of strain change (total change observed so far due to the trend was less than 50 microstrains), these oscillations may be due to mechanical strain caused by thermal expansion/contraction of the grout. In comparison to large cracks, these small oscillations will be negligible. An overall downward trend was observed for the strain sensors. Since the strain measurements have

been temperature compensated, the downward trend was most likely caused by the contraction of grout in its curing time.

As can be seen from the data, the FBG strain sensors allowed observation of the curing process of the grout as well as any subsequent developments regarding the state of the grout, such as curing state or the existence of local cracks. For newly erected walls of any structure, knowing the development stage of the construction material can be useful in coordinating the construction schedule or whether the structure has met the required specifications. In subsequent studies, it may be useful to artificially induce damage to the test structure to observe its effects on the sensor system measurements.

6.2.4.3. Water sensors

A total of four sensors showed signs of water infiltration indicating the grout shell of the four water sensors opened after grouting and liquid moisture from the grout entered the sensor cavity. Since data was acquired several days after the grout pouring process, it is possible that more sensors also have liquid moisture infiltration. However, the four sensors mentioned above were observed to have a wavelength shift of greater than 0.1 nm, thus confirming the presence of water in those sensors. Except for the water sensors near the top surface (P3 and P7 top), the rest of the water sensors exhibited no more changes after the first few days of measurement. Possible reasons include the retention (within the steel sensor casing) and migration of moisture within the cube towards the top surface or the migration of small amounts of moisture from the atmosphere towards the top surface sensors (via the porosity of grout); with the lower level of activity in Panel 7 top indicating that its initial grout shell is more intact. During the grout pouring process, liquid moisture was observed leaking through the optical fiber cable ends outside the

cube, indicating that the pressure of the pouring process along with capillary action has forced some of the grout moisture through the sensor connections that were embedded within the cube. To avoid damage to the interrogator and allow as much water as possible to exit the cables, data acquisition was halted until several days after the grout pouring process. Although the liquid within the cables ultimately did not have a significant detrimental effect on the signal strengths, an unknown amount of remaining water (in particular on the sensor branch hosting the water sensor on Panel 3 top) may have entered the sensor gradually over the testing period, thus causing the continuous increase in wavelength shift. This phenomenon may provide motivation to further reinforce or seal fiber optic cable connection points that will be embedded within a structure in order to preclude water entering the fiber cable system and possibility activating the water sensors. Information regarding water leakage within a structure will be important for monitoring vital structures such as nuclear containment facilities as the presence of liquid water may mean that 1) a sizeable opening has exposed the sensor to either an internal source or the atmosphere, and 2) any reinforcing steel members may be in danger of corrosion. In future developments of the water sensor, the SAP may be engineered to be reactive towards selected stimulus, thus expanding the potential use of the water sensor in detecting other chemicals (e.g., biological agents, oil spills, etc.) Note that the water sensors had difficulty returning to its baseline wavelength during the whole testing period. The development of a next generation water sensor that was able to cycle repeatedly in short time periods was discussed in chapter four.

6.2.5. Conclusion

Twenty-three out of twenty-four FBG sensors maintained signal output during the testing period and measured strain, temperature, and the presence of water within the grout cube. The grout pouring process further caused temporary signal loss in four sensors, but gain adjustment amended the signal strength. The data further shows the potential of FBGs for the monitoring of civil structures over an extended period of time due to their inherent advantages of networkability, small size, and flexibility. **Note:** The work in this chapter is also available in the 4th Asia-Pacific Young Researchers and Graduates Symposium 2012 proceedings, and is under the same title.

Chapter 7 FBG Based-Bond Slip Detection of Prestressed Tendons in Concrete Bridge Girders

7.1. Introduction

7.1.1. Background

Pretensioned, prestressed concrete girders are predominantly used in highway bridge construction at present. The force applied to concrete girder through the transfer length strengthens the girder against any future applied loads, and helps the designer to use shallower cross-sections than normal reinforced concrete girders. Problems arise when the concrete-tendon bond along the transfer length become degraded due to many natural and artificial factors, resulting in premature failure of the girder. Recently, many researchers have tried to measure the average slip over the entire transfer length. The following sections of this paper describe a novel concept and method of using fiber optic fiber Bragg grating (FBG) sensors to measure the slip locally. With the new information provided by the sensors, further insight in understanding the bond slip phenomenon may be gained.

7.1.2. Bond Slip in Reinforced Concrete

Concrete structures supported by an internal array of steel tendons or bars (rebars) are categorized as reinforced concrete (RC). The transferral of forces between the concrete and the steel reinforcement through their bonding interface magnifies the overall strength of the concrete structure. Without an adequate bond, the RC structure will have similar strengths as a pure concrete structure. Thus, the steel-concrete bond plays a central role in the strength of an RC structure. Bond slip occurs when an external force overcomes the strength of the steel-concrete bond and induces a relative displacement between the affected reinforcement members and the concrete. The mechanism and behavior of bond-slip depends on the reinforcement geometry (e.g., deformed rebars) as well as the types of materials involved. Depicted in Figure 7-1 are several general stages

of bond slip as defined by the International Federation for Structural Concrete (CEB-FIP) [125, 126].

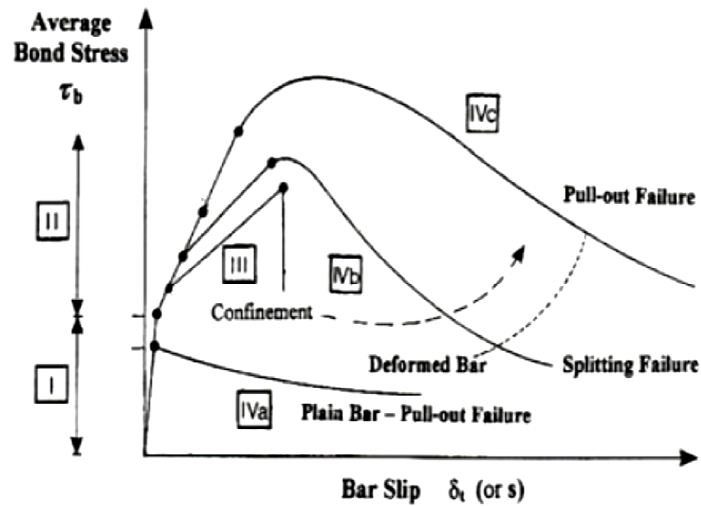


Figure 7-1 Bond stress vs bond slip behavior (adapted from CEB-FIP).

In stage I, the steel-concrete bond is intact and dominated by chemical adhesion, and no cracking has occurred. At stage II, cracking begins and the chemical adhesion in the bonds begins to degrade. For deformed rebars (rebars bearing any protruding geometry as anchorage points for better contact with concrete), microcracks begin forming at protruding portions of deformed rebars to allow for slippage of the rebar. Progression into stages III, IVa, IVb, and IVc depend on the particular conditions of the structure in question (e.g., deformity of rebar, level of confinement, etc.), however these stages all describe the failure mode of the steel-concrete bond [125].

7.1.3. Detection of bond slip

Investigations of the bond slip phenomenon have been performed over the past century. One of the earliest organized study about bond slip was carried out by Abrams in 1913 [127]. In his study, periodically spaced openings in the concrete revealing the reinforcing bar allowed the measurement of local slips. Watstein used a similar method to



measure the local strain of the steel reinforcement [128]. Later, Mains measured the tensile and bond stresses of reinforcing bars by cutting apart the test bars longitudinally, installing strain gauges within, and welding the half bars back together [129]. The use of fiber optics, and in particular, fiber Bragg gratings were quite recent [130, 101]. For example the work done by Kenel et al. measured the local strain of reinforcing steel bars by installing multiplexed FBGs along a 1mm deep x 1mm wide groove running through the side of a 10 mm diameter bar. Their results measured the strain of the steel bars well into the plastic region and demonstrated that bond properties are much less affected when FBGs were used instead of traditional strain gauges due to the compactness of fiber optic lines [130].

The use of strands instead of bars allow for prestressing to be part of the reinforcement. By stretching the strands, or tendons, prior to concrete pouring and releasing them after concrete curing, the entire structure will benefit from additional tensile strength as the tendon strain transfer to the concrete. The bond slip phenomenon also affects prestressing tendons, and has also been studied for some time [132, 133, 134, 135, 131]. Load cells and extensometers have been used to measure the shear stress and slip, respectively. However, such methods only allow the measurement of the average bond slip along the entire transfer length and do not provide much information about the local bonding conditions of the prestressing tendon. While FBGs have been utilized for the monitoring of prestressed concrete structures, the studies that used FBGs either only measured the pretensioning process [136] or hydration and cracking [137]. In the following sections is a new look at the bond slip phenomenon of prestressing tendons through the use of FBG strain sensors described in the earlier sections of this chapter.

Unlike steel rebars, prestressing tendons are composed of braid strands of steel wires and thus prevent the formation of grooves in which FBG sensors may be installed. Without the protection of a host (e.g., steel rebar), the FBG will be exposed and will require separate guarding against hazards associated with the concrete pouring and curing process. Thus by taking advantage of the ruggedly designed strain sensor packaging described previously, FBG strain sensors could be safely installed along a tendon, and allow the measurement of local strain levels.

In the following experimental verification of the method, three FBGs were separately installed on three tendons for the detection of bond slip in the testing of a prestressed concrete bridge girder. An additional FBG strain sensor was embedded in the concrete without contact with reinforcing members, and a FBG temperature sensor was used to compensate for temperature. Table 7-1 shows the different types of FBG sensors used for the experiment, most of which were used in chapter six. For comparison, eight linear variable differential transformers (LVDTs) were set up at the protruded portion of the prestressing tendons.

Table 7-1 FBG strain (short and long gauge) and temperature sensors used during the experiment. Each sensor was encapsulated in a stainless steel casing to provide robustness.

Type	Picture	Size (inches)
Temperature		2.8 x 0.42 x 0.18
Strain (Short Gauge)		Diameter: 0.13 Length: 2.5

Bond slip can be inferred by locally measuring the strain experienced by the tendons during the application of increasing load on the host girder. As the tendon begins to slip from the concrete, less strain will be directly transferred between the concrete and the tendons, and FBG strain readings will present a noticeable divergence between the applied load and the expected strains.

7.2. Experimental Program

7.2.1. Concrete Girder Construction and Testing

The experiment was performed on a Tx28 girder 25 feet in length and 28 inches in depth. The beam was reinforced in flexure with 40 seven-wires, low-relaxation straight tendons 12.7 mm (0.5-in.) in diameter with a cross sectional area of 99 mm² (0.153 in²) (Figure 7-2). The prestressing tendons were pretensioned by hydraulic jacks placed in a prestressing steel platform/bed. Transverse steel along with all the other confining and flexural reinforcements were installed in the girders. TxDOT traditional concrete mix was prepared in a plant mixer, transported to the casting site, and deposited into the formworks using a mobile hopper. During casting, spud vibrators were used to compact the concrete as well as bed vibrator fixed on the side forms. Standard concrete cylinders – 152 mm (6 inches) in diameter and 305 mm (12 inches) in height were cast. Just prior to the actual girder tests, the concrete cylinders were tested to get the representative concrete compressive strength of the girder. One day after casting the girder, the prestressing tendons were slowly released, whereupon the girder reached the required strength. The release strength was 48.95 MPa (7100 psi). After release, girders were transported to the Thomas T.C. Hsu Structural Research Laboratory at the University of Houston.

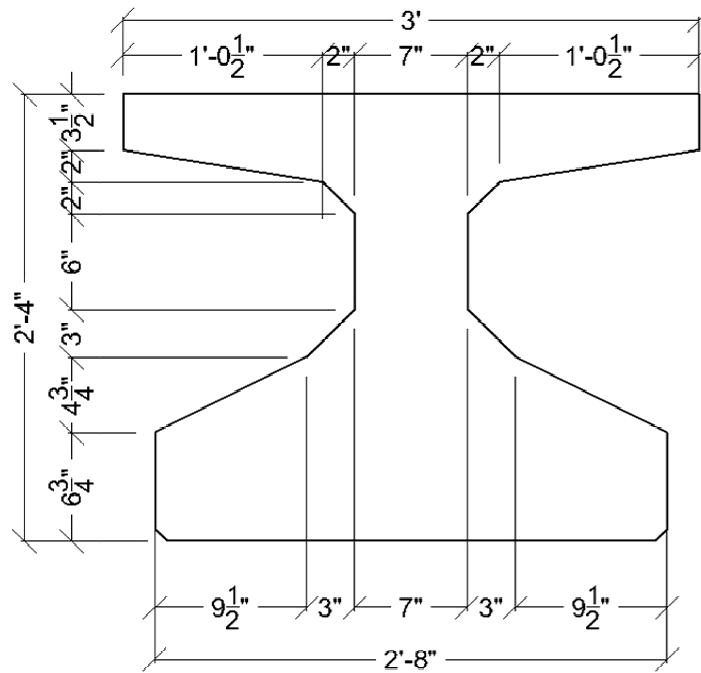


Figure 7-2 Cross section of tested girder Tx28.

During testing, the beam was subjected to vertical loading up to its maximum shear capacity using a steel loading frame (Figure 7-3). An actuator was used to apply loads onto the north side of the beam. The actuator load was applied through a roller assembly consisting of three bearing plates and one roller. Lead sheets were also used between the beam and the load bearing surface. The actuator was placed at a distance of 46" from the north end of the beam. The support at the end of the beam consisted of an assembly of steel plates and a load cell.

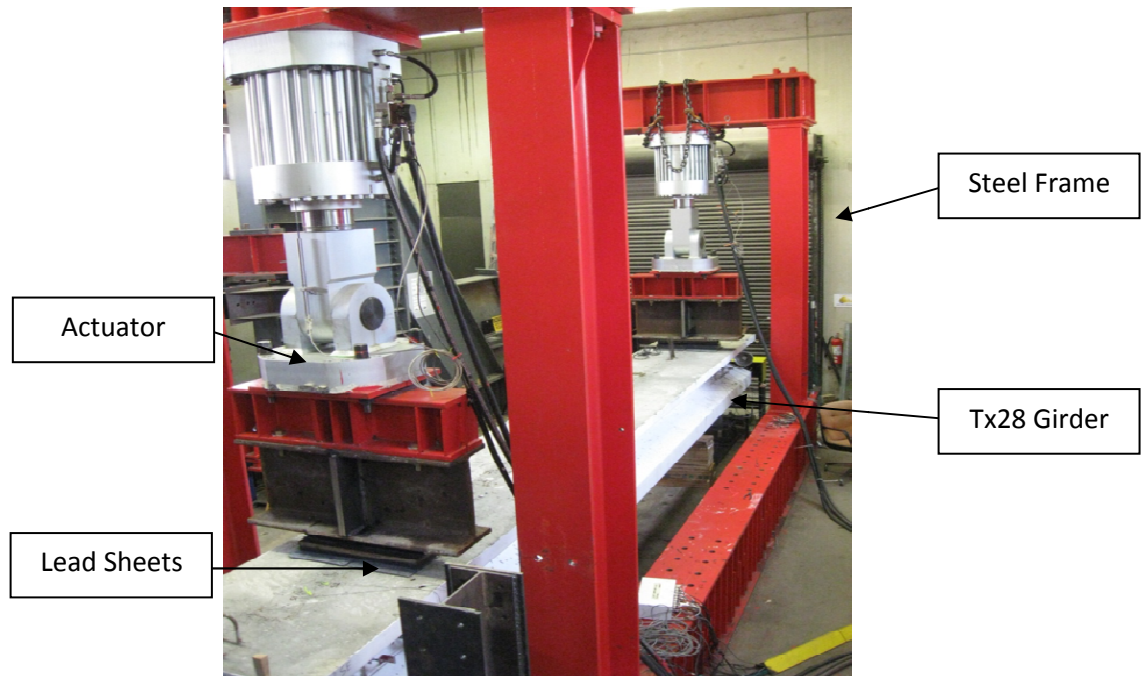


Figure 7-3 Experimental set-up of the girder loading experiment.

Eight linear variable differential transformers (LVDTs) were positioned on selected tendons against the concrete surface to measure any bond slip. Because the shear bond failure is known for the crushing of concrete at the intersection between the bottom flange and the web, which indicates that the most effective tendons are the closest ones to that location, six LVDTs were posted on selected tendons of the closest row to the web against the concrete surface. Additional two LVDTs were posted on the two tendons closest to the web center in the most bottom row. Figure 7-4 shows the locations of the LVDTs. The LVDTs were leveled and tied mechanically to the selected tendons against the concrete surface to ensure their free movement along with the tendons in the case of any slippage. A data acquisition program CATMAN was used to monitor the displacement measured by the LVDTs.

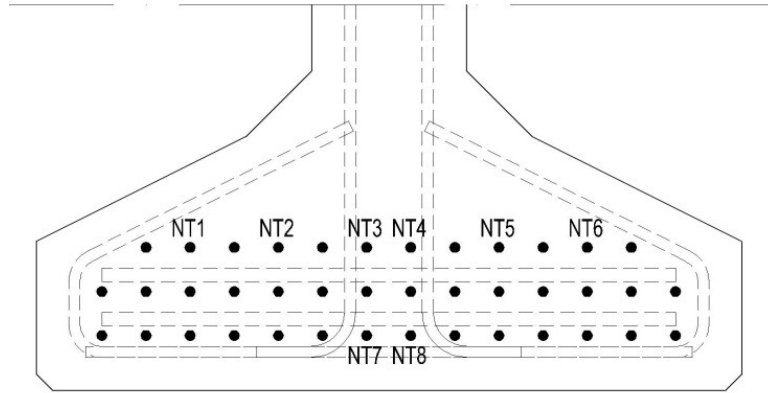


Figure 7-4 Layout of the Selected Tendons with LVDTs.

7.2.1.1. FBG Installation and Interrogation

A total of three FBG (labeled SG1-3) strain sensors and one FBG temperature sensor (labeled T1) were used in the experiment. In-lab calibration (same method as in chapter six) of the strain sensors revealed a sensitivity of $0.2 \mu\epsilon/\text{nm}$. Four of the strain sensors were bonded at their gripping sections along the length of the host tendon using cyanoacrylate (Figure 7-5). The temperature sensor was placed near the strain sensors to allow temperature compensation of the strain sensors in case of fluctuating temperatures. Optical cables connected to the sensors were bound to the vertical rods, with only the connecting ports protruding from the top surface of the girder. Figure 7-6 and Table 7-2 summarizes the positioning of the sensors within the girder.

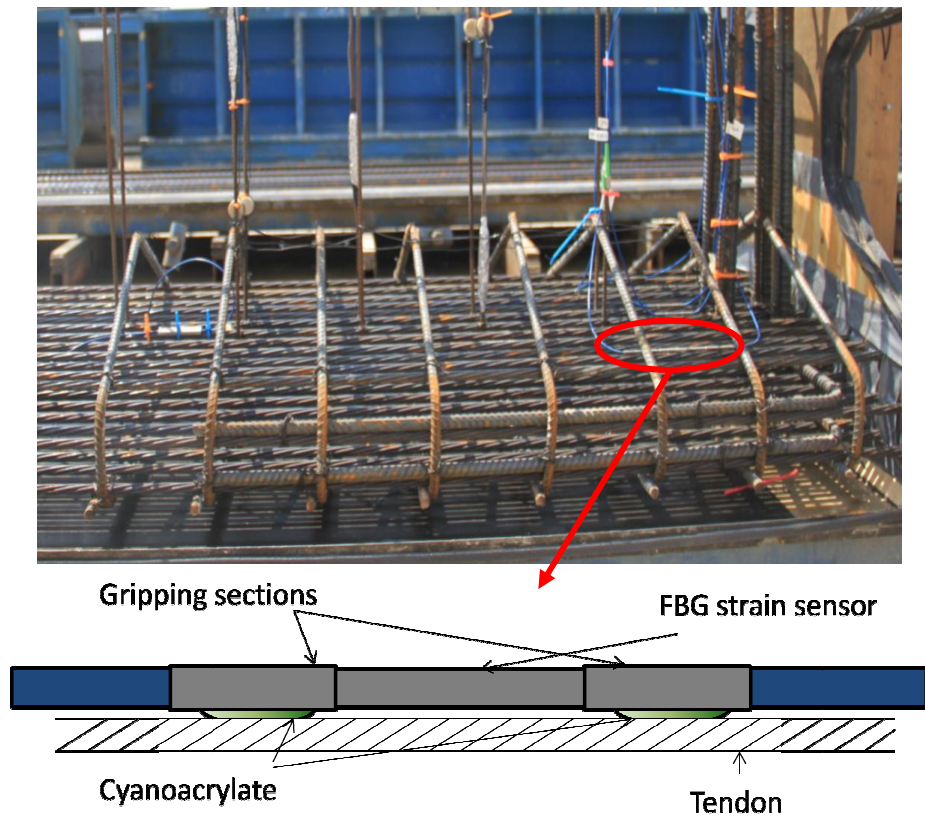


Figure 7-5 (Left) Installation of FBG sensors onto the tendons prior to concrete pouring. (Right) Strain sensors are bonded via cyanoacrylate to the tendons.

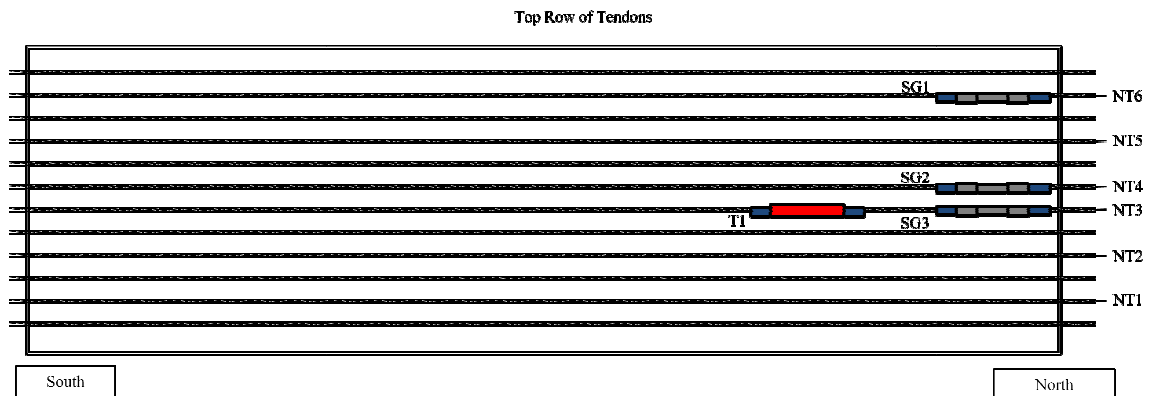


Figure 7-6. Relative placement of FBG sensors in the concrete girder along the top row of tendons.

Table 7-2. Sensor placement within the girder.

Sensor	Type	Location	Central Wavelength
SG1	Strain, Short gauge	2 nd tendon from east edge, 8 inches from north edge	1512 nm
SG2	Strain, Short gauge	6 th tendon from east edge, 8 inches from north edge	1512 nm
SG3	Strain, Short gauge	7 th tendon from east edge, 8 inches from north edge	1564 nm
T1	Temperature	7 th tendon from east edge, 2 feet south of SG3	1543 nm

A custom made FBG interrogator was used to receive signals from the FBG sensors. A LabVIEW based application was used to observe and record data (sampling frequency ranged between 8.9 to 9.1 Hz).

7.3. Experimental Results

7.3.1. LVDT Readings

The first shear crack was observed at a reaction load of 209 kips. The beam failed when the measured reaction was 457 kips. Figure 7-7 shows the behavior of tendons at different stages of loading according to the LVDTs. Most tendons began to slip at shear forces between 200 and 300 kips. Point A (280 kips) in the figure marks the shear force upon which all tendons have begun slipping (first slope change). As the beam approached failure near point B (450 kips), the slip rate experienced a secondary slope change. The tendons closer to the web (NT3 and NT4) exhibited a higher slip than the ones further away.

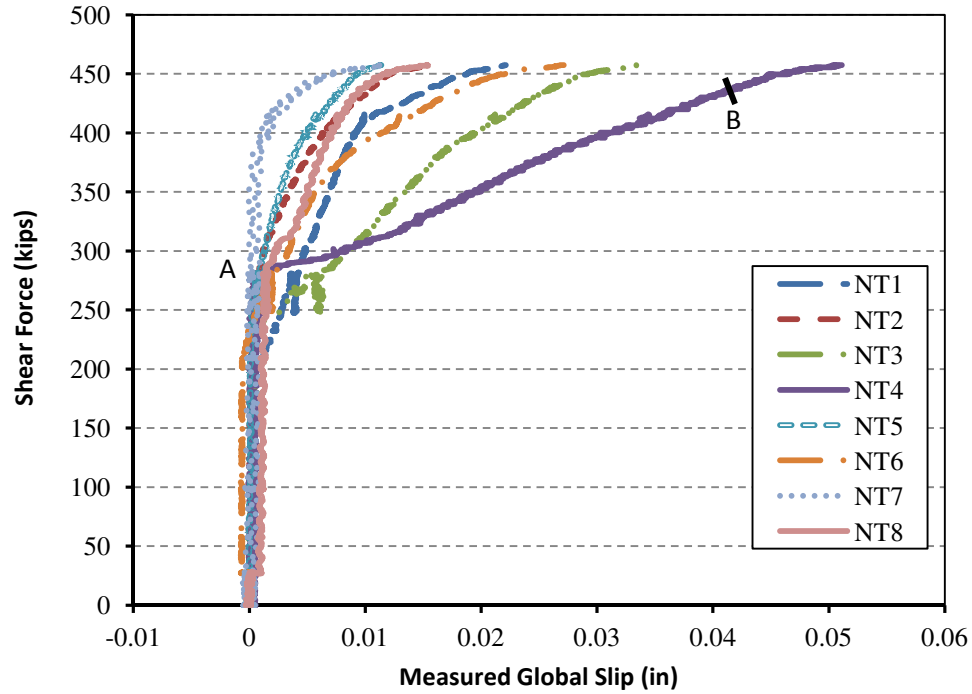


Figure 7-7 Measured Global Slip versus Shear Force.

7.3.2. FBG Readings

The strain readings from the tendon-mounted FBGs generally increased as the loads escalated (Figure 7-). SG1 began to detect slippage (decreasing strains) at 340 kips, while SG2 and SG3 began at 430 kips. Failure of the girder was observed at a shear load of 457 kips, and was coincidental with a sharp spike seen in FBG signals. Noteworthy is that the strain readings began to increase as the loads continued to increase after failure. Eventually with the application of even more load, the tendon-mounted FBGs began to show irregular readings (e.g., > 2000 microstrains) (not shown).

SG2 showed the most change in strain (> 1000 microstrain), while SG1 and SG3 showed little change in comparison (< 40 microstrain). On the other hand, all strain sensors bonded to the tendons (SG1-3) exhibited a similar trend, as described above, in the strain throughout the loading process. Temperature was stable throughout the test at 10 °C, thus not requiring any temperature compensation for any of the other FBG sensors.

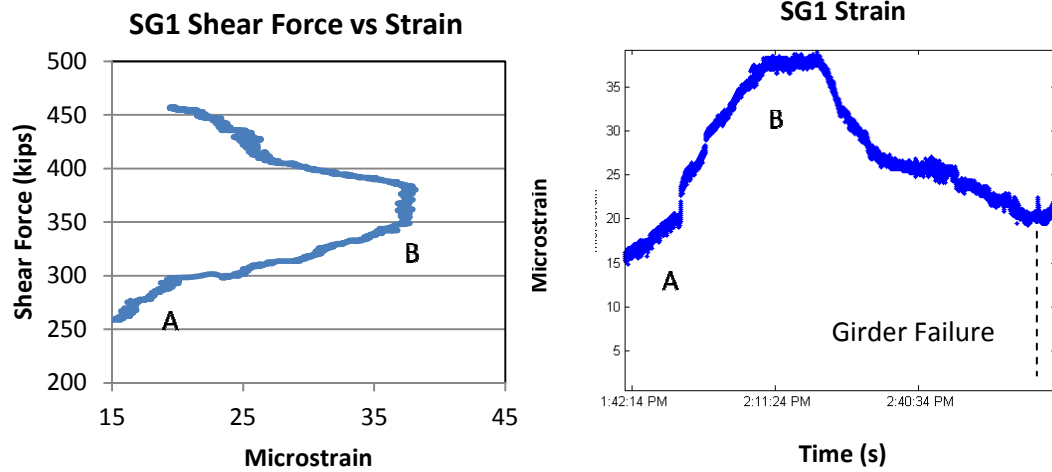


Figure 7-8 Measured Local Slip versus Shear Force. a) Strain profile for sensor SG1.

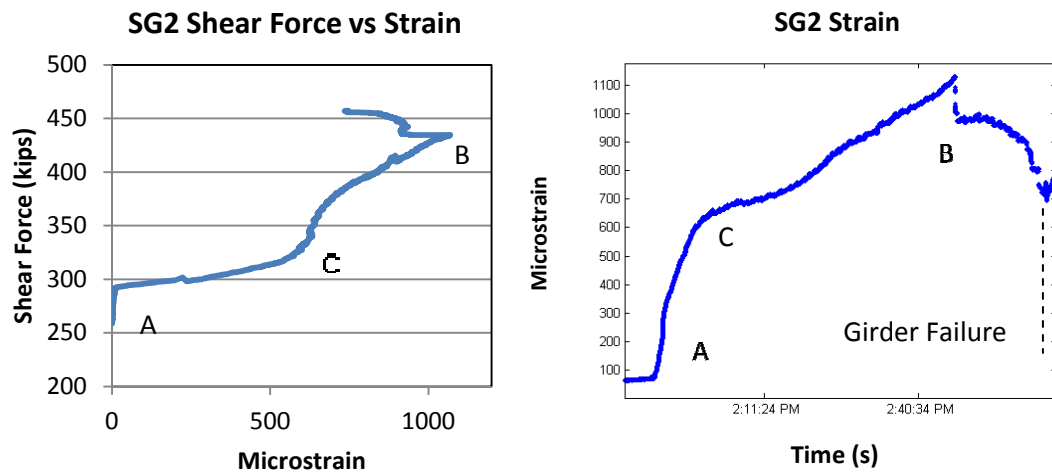


Figure 7-8 Measured Local Slip versus Shear Force (cont.). b) Strain profile for sensor SG2.

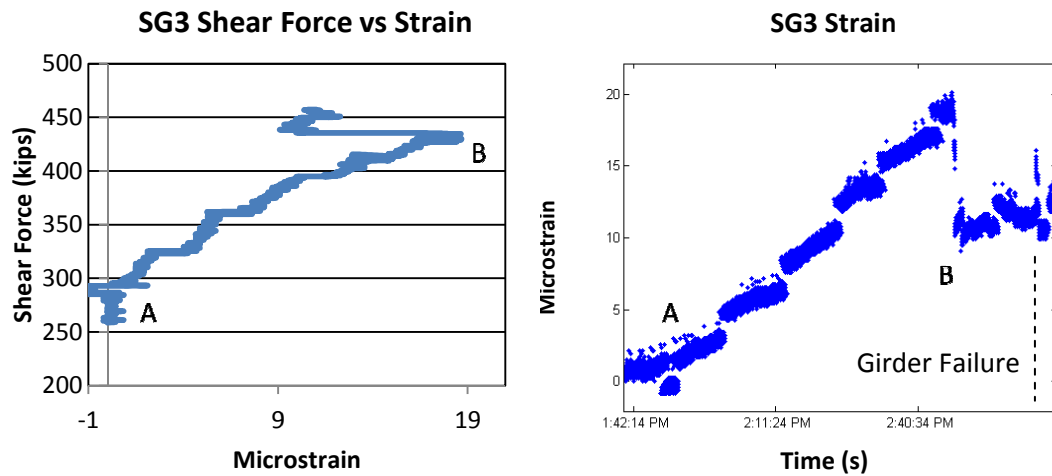


Figure 7-8 Measured Local Slip versus Shear Force (cont.). c) Strain profile for sensor SG3.

7.4. Discussion of FBG Based-Bond Slip Detection

The purpose of the novel FBG sensing method was to provide a new, local perspective of bond slip that was previously not shown by the LVDT sensors (Figure 7-7) or other conventional sensors in the literature. As indicated by the data, a degree of correlation can be observed between the measurements of the FBGs and the LVDTs, but as will be soon discussed, key differences exist especially near the failure of the tendon-concrete bond.

In Figure 7- point A (280 kips) marked the beginning of bond slip while point B (430 kips) marked the failure of the tendon-concrete bond. From the perspective of the FBG sensors, the transition between point A and point B can be generally characterized as positive slope. The complete loss of the bond may be distinguished by the sharp drop in strain observed at point B. SG2 showed an additional change in slope marked by point C that may be a finer indicator of the true beginning of bond slip. For instance, this change in slope may be correlated to the transition from stage I (intact chemical adhesion) to stage II (formation of cracking and degradation of chemical adhesion) in the

progression of bond slip as defined by Figure 7-1. This transition was not observed in SG1 or SG3 potentially due to a stronger bond between SG2 and its tendon that allowed such a measurement. The corresponding points (A and B) are marked in the LVDT readings Figure 7-7. Similar to the FBG readings, the LVDT signals increased between point A and point B. However, unlike the FBG readings, the complete loss of the bond was not observed as the measured slip continued to increase after point B.

On the other hand, the strain sensor that experienced the highest strains (>1000 microstrain) was SG2, which was located close to the web, while the outer-lying sensors experienced less strain (<40 microstrain). While this difference can be attributed partly to potential difference in bonding conditions, the global bond-slip as measured by the LVDTs was also more severe in tendons close to the web (see NT3 and NT4, which were closer to the web-bottom flange interface) thus suggesting a role of the tendon position in determining the degree of bond slip.

A combination of forces, comprising of the sensor-tendon bond and the sensor-concrete bond, acted upon the tendon-mounted FBG sensors during the test. Thus, the strains measured by the FBG sensors, although mainly contributed by the tendons due to the stronger cyanoacrylate bond, were also partially affected by the bond and friction from the concrete. This interaction with the concrete cannot be entirely eliminated due to the fiber optic cables extending from both ends of each FBG sensor. The increasing strains measured by the tendon-mounted FBG sensors output after the girder failed suggest that the sensors experienced tension. However, since the bond stress in the transfer length has vanished due to bond failure, the remaining strain source was generated tension between the FBG strain sensor head (i.e., the sensing portion) and the

fiber optic cables that were still firmly bonded to the concrete. In order for such tension to occur, the FBG strain sensor heads must have relative displacement with respect to the cables, thus confirming that the FBG strain sensor has bonded more strongly with the tendons (Figure 7-9).

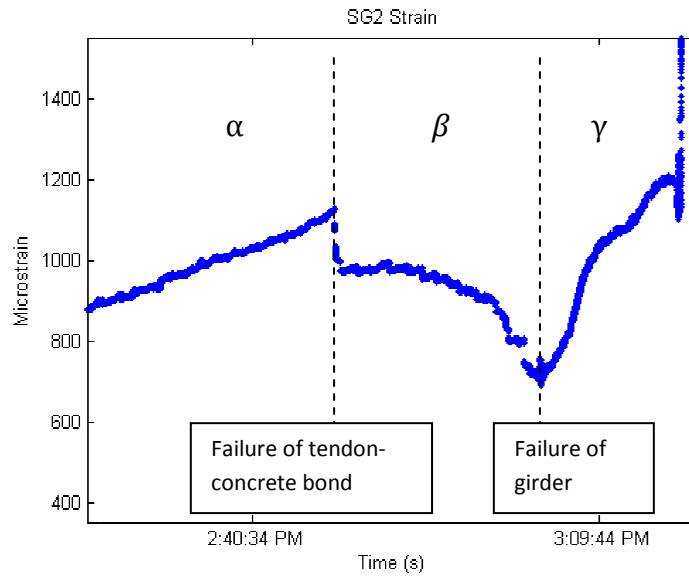


Figure 7-9. Close up of SG2 readings near girder failure.

The sharp drop in strain as indicated in Figure 7-9 is indicative of the complete loss of sensor-concrete bond, giving way to strains originating from the sensor-fiber cable tension and the relaxation of the tendon. The sensor-fiber cable tension may have prevented the FBG strain sensors from measuring the true relaxation of the tendon in the transfer length.

Thus, the loading profile can be divided into three stages as shown in Figure 7-9. In stage α , the forces of the sensor was dominated by the bonds with the tendon and the concrete. In stage β , the sensor was no longer bonded to the concrete, and the strains predominately came from the relaxation of the tendon, the tension in the fiber optic cables, and friction between the sensor and concrete. In stage γ , which occurred after

girder failure, the strains of the FBG were dominated by the increasing tension placed between the sensor head and fiber optic cables. Therefore, the signals of the FBGs were able to show two important events that were not captured by the LVDTs. These events were the complete loss of the tendon-concrete bond and the failure of the girder.

7.5.Conclusions

A novel method using FBGs to provide a local perspective of tendon slip in prestressed concrete girder was developed and presented in this paper. The forces affecting the measurements enabled by the method allowed the observation of the entire slipping process from the beginning of bond slip until complete bond failure, which was not captured in the traditional global measurements of the LVDTs. Future implementations of this method include installing additional FBGs along the transfer length to help in better understand the propagation of bond slip along the entire transfer length.

Chapter 8 General Conclusions and Future Work

FBGs have been used in numerous applications across diverse engineering fields, and are on the road to becoming a mature technology ready for large volume use in the industry. This dissertation has presented examples of how FBGs were used to help solve some of the newest engineering problems in the fields of medicine and SHM. In chapter three, an FBG sensor was embedded into a protective steel cylinder casing and placed inside a model ablation catheter. The sensor was able to determine contact and resting states based on the magnitude and appearance of signal patterns generated by myocardial contracts. A small reversal was seen prior to perforation for the epoxy-based sensor that may potentially act as a warning for impending perforation. A continuation of this work will involve a study on the perforation mechanics of cardiac tissue due to the pressure exerted by an ablation catheter.

Chapter four presented a water sensor that was an improvement upon the water sensor described in chapter four. The improved version of the sensor was able to undergo multiple load cycles and return to its baseline levels within an short timeframe (with respect to the lifetime of a civil structure). Furthermore, the sensor was able to survive and recover from saturating (i.e., flooding) conditions. Subsequent development of this sensor will have deeper analysis of the mechanical theory governing the sensor response in order to correlate the FBG wavelength to the volume of water captured by the sensor. In addition, alternative polymers that are reactive to other chemicals should be tested. For example, the sensor may be used to detect oil spill in the ocean by using a polymer that is sensitive to petroleum-related chemicals and not water.

In chapter five, a new sensor system design was described that allowed the use of FBGs for the measurement of high frequency vibrations. Although the measurable magnitude of vibration was limited region of the optical power profile as seen by the photodiode, the capabilities of the system in sensing dynamic signals were demonstrated through the measurement of acoustic waves emitted by a PZT patch across a distance. Future development of this sensor system would aim towards the multiplexing of more FBGs to allow additional sensing points, and a method to enlarge the range of vibration magnitude measurable by the system. A large scale deployment, potentially with PZT active sensing systems, in a civil structure will further validate the use of the system for SHM.

In chapter six and seven, FBG sensors were demonstrated for use in new cases of SHM. In the first research problem, strain, temperature, and water presence in a model wall of a nuclear containment facility were measured by a network of 23 FBG sensors. The daily temperature fluctuations and the formation of cracks were able to be tracked by the FBGs. In the second research problem, FBGs were successfully used to observe the local strains of a prestressing tendon as bond slip occurred. Several stages of bond slip were observed from the perspective of FBG strain sensors. Future development of this novel FBG-based bond slip measurement includes the installation of additional FBG strain sensors along the prestressing tendons and also the use of a different sensor network setup to avoid tension between the sensor head and the optical cables.

References

1. Kashyap R and López-Higuera J M 2002 *Handbook of Optical Fibre Sensing Technology* ed J M López-Higuera (New York Wiley) p 349
2. Othonos A and Kalli K 1999 *Fiber Bragg Gratings – Fundamentals and Applications in Telecommunications and Sensing* (Norwood Artech House Inc.)
3. Kersey A D, Berkoff T A, and Morey W W 1993 Multiplexed fiber Bragg grating strain-sensor system with a fiber Fabry-Perot wavelength filter *Optics Letters* **18** 1370-1372
4. Kersey A D 1993 Interrogation and multiplexing techniques for fiber Bragg grating strain-sensors *Society of Photo-Optical Instrumentation Engineers* (Boston, US) **2071** 30-48
5. Jackson D A, Lobo Ribeiro A B, Reekie L, and Archambault J L 1993 Simple multiplexing scheme for a fiber-optic grating sensor network *Optics Letters* **18** 1192-1194
6. Geiger H, Xu M G, Dakin J P, Eaton N C and Chivers P J 1996 Progress on grating interrogation schemes using a tunable filter, *Proceedings of 11th Optical Fiber Sensors Conference (OFS'11). 11th Optical Fiber Sensors Conference (OFS'11)* (Washington, US) *Optical Society of America*, pp 376-379
7. Geiger H, Xu M G, Eaton N C, and Dakin J P 1995 Electronic tracking system for multiplexed fibre grating sensors *Electronics Letters* **31** 1006-1007
8. Melle S M, Liu K, and Measures R M 1992 A passive wavelength demodulation system for guided-wave Bragg grating sensors *IEEE Photonics Technology Letters* **4** 516-518
9. Kersey A D, Berkoff T A, and Morey W W 1992 High-resolution fibre-grating based strain sensor with interferometric wavelength-shift detection *Electronics Letters* **28** 236-238

10. Ball G A, Morey W W, and Cheo P K 1994 Fiber laser source/analyzer for Bragg grating sensor array interrogation *IEEE Journal of Lightwave Technology* **12** 700-703
11. Kersey A D, Davis M A, Patrick H J, LeBlanc M, Koo K P, Askins C G, Putnam M A, and Friebele E J 1997 Fiber grating sensors *IEEE Journal of Lightwave Technology* **15** 1442-1463
12. Keating, M T and Sanguinetti, M C 2001 Molecular and cellular mechanisms of cardiac arrhythmias *Cell*, *104*, 569–580
13. Lloyd-Jones D, Wang T J, Leip E P, Larson M G, Levy D, Vasan R S, D'Agostino R B, Massaro J M , Beiser A, Wolf P A, and Benjamin, E J 2004 Lifetime risk for development of atrial fibrillation *Circulation* **110** 1042–1046
14. Haines, D E 1993 The biophysics of radiofrequency catheter ablation in the heart The importance of temperature monitoring *Pacing Clinical Electrophysiology* **16** 586–591
15. Bunch T J, Asirvatham S J, Friedman P A, Monohan K H, Munger T M, Rea R F, Sinak, L J, and Packer D L 2005 Outcomes after cardiac perforation during radiofrequency ablation of the atrium *Journal of Cardiovascular Electrophysiology* **16** 1172–1179
16. Stellbrink C, Siebels J, Hebe J, Hoschky D, Haltern G, Zieger K, Hanrath P, and Kuck K H 1994 Potential of intracardiac ultrasonography as an adjunct for mapping and ablation *American Heart Journal* **127** 1095–1101
17. Chu E, Fitzpatrick A P, Chin M C, Sudhir K, Yock P G, Lesh M D 1994 Radiofrequency catheter ablation guided by intracardiac echocardiography *Circulation* **89** 1301–1305
18. Kalman J M, Fitzpatrick A P, Olgin J E, Chin M C, Lee R J, Scheinman M M, and Lesh M D 1997 Biophysical characteristics of radiofrequency lesion formation *in vivo* Dynamics of catheter tip-tissue contact evaluated by intracardiac echocardiography

19. Calkins H, Niklason L, Sousa J, El-Atassi R, Langberg J, and Morady F 1991 Radiation exposure during radiofrequency catheter ablation of accessory atrioventricular connections *Circulation* **84** 2376–2382
20. Stec S, Zaborska B, Sikor-Frac M, Krynski T, and Kulakowski P 2011 First experience with microprobe transoesophageal echocardiography in non-sedated adults undergoing atrial fibrillation ablation Feasibility study and comparison with intracardiac echocardiography *Europace* **13** 51–56
21. Saxon L A, Stevenson W G, Fonarow G C, Middlekauff H R, Yeatman L A Sherman C T, and Child J S 1993 Transesophageal echocardiography during radiofrequency catheter ablation of ventricular tachycardia *American Heart Journal* **72** 658–661
22. Cao H, Tungjitkusolmun S, Choy Y B, Tsai J Z, Vorperian V R, and Webster J G 2002 Using electrical impedance to predict catheter-endocardial contact during RF cardiac ablation *IEEE Transactions of Biomedical Engineering* **49** 247–252
23. Cao H , Speidel M A, Tsai J Z, van Lysel M S, Vorperian V R, and Webster J G 2002 FEM analysis of predicting electrode contact from RF cardiac catheter ablation system impedance *IEEE Transactions of Biomedical Engineering* **49** 520–526
24. Paul S, Belhe K R, Cao H, and Thao C Assessment of Electrode Coupling of Tissue Ablation *U S Patent 2010/0228247 A1*, 9 September 2010
25. Demos S G, and Sharareh S 2008 Real time assessment of RF cardiac tissue ablation with optical spectroscopy *Optics Express* **16** 15286–15296
26. Yokoyama K, Nakagawa H, Shah D C, Lambert H, Leo G, Aeby N, Ikeda A, Pitha J V, Sharma T, and Lazzara R 2008 Novel contact force sensor incorporated in irrigated

- radiofrequency ablation catheter predicts lesion size and incidence of steam pop and thrombus *Circulation: Arrhythmia Electrophysiology* **1** 354–362
27. Leo G, Aeby N, and Inaudi D Medical Apparatus System Having Optical Fiber Load Sensing Capability, *Endosense WO Patent 2006/092707 A1* 8 September 2006
 28. Shah D, Lambert H, Langenkamp A, Vanenkov Y, Leo G, Gentil-Baron P, and Walpht B 2011 Catheter tip force required for mechanical perforation of porcine cardiac chambers *Europace* **13** 277–283
 29. Ansari F, and Libo Y 1998 Mechanics of Bond and Interface Shear Transfer in Optical Fiber Sensors, *Journal of Engineering Mechanics* **124** 385-394
 30. Li D, Li H, Ren L, and Song G 2006 Strain transferring analysis of fiber Bragg grating sensors *Optical Engineering* **45** 024402-1-024402-8
 31. Zhou G D, Li H N, Ren L, and Li D S 2006 Influencing parameters analysis of strain transfer in optic fiber Bragg grating sensors *Proceedings of SPIE* **6179** R-1 – R-9
 32. Specification sheet for ITW Devcon 5 Minute Epoxy. <www.devcon.com> , Assessed Dec. 14, 2012
 33. Duncan B 2001 The Hyperelastic Properties of a Polyurethane Adhesive, *Performance of Adhesive Joints Programme Project PAJex2 – Flexible Adhesives, National Physical Laboratory* (Teddington: Middlesex, UK)
 34. Haran F M, Rew J K, and Foote P D 1998 A strain-isolated fibre Bragg grating sensor for temperature compensation of fibre Bragg grating sensors. *Measurement Science and Technology* **9** 1163–1166

35. Yeo T L, Eckstein D, McKinley B , Boswell L F, Sun T, and Grattan K T V 2006 Demonstration of a fibre-optic sensing technique for the measurement of moisture absorption in concrete *Smart Materials and Structures* **15** N40-N45
36. Yeo T , Cox M A C, Boswell L F, Sun T, and Grattan K T V 2006 Monitoring Ingress of Moisture in Structural Concrete Using a Novel Optical-Based Sensor Approach *Journal of Physics Conference Series*, **45** 186-192
37. Yeo T L, Sun T, and Grattan K T V 2008 Fibre-optic sensor technologies for humidity and moisture measurement *Sensors and Actuators A* **144** 280-295
38. Healy W, Luo S, Evans M, Sucheta A, and Liu Y 2003 Development of an optical fiber-based moisture sensor for building envelopes *24th AIVC Conferece & BETEC Conference, Ventilation, Humidity Control and Energy Proceedings* 277-282
39. Kunzler W, Calvert S , and Laylor M 2004 Implementing fiber sensors to monitor humidity and moisture *Proceedings of SPIE* **5384** 54-63
40. Visscher G J W 1995 Standard psychrometers a matter of p references *Measurment Science Technology* **6** 1451-1461
41. Rittersma Z M 2002 Recent achievements in miniaturized humidity sensors – areview of transduction techniques *Sensors and Actuators A* **96** 196-210
42. Traversa E 2005 Ceramic sensors for humidity detection the state-of-the-art and future developments *Sensors and Actuators B* **23** 1335-1356
43. Golonka L J, Licznarski B W, Nitsch K, and Terycz H 1997 Thick-film humidity sensors *Measurement Science Technology* **8** 92-98
44. Qu W, and Meyer J -U 1997 Thick-film humidity sensor based on porous MnWO₄ material *Measurement Science Technology* **8** 593-600

45. Wang H, Feng C D, Suin S , Segre C U, and Stetter J R 1998 Comparison of conductrometric humidity-sensitive polymers *Sensors and Actuators B* **40** 2111-2116
46. Gluck A , Halder W, Lindner G, Muller H , and Weindler P 1994 PVDF-excited resonance sensors for gas flow and humidity *measurements* *Sensors and Actuators B* **18-19** 554-557
47. Zhou Q, Shahriari M R, Kritz D, and Sigel Jr G H 1988 Porous fiber-optic sensor for high-sensitivity humidity measurements *Analytical Chemistry* **60** 2317-2320
48. Ando M, Kobayashi T, and Harutu M 1996 Humidity-sensitive optical absorption of CO₂O₄ film *Sensors and Actuators B* **32** 157-160
49. Otsuko S, Adachi K, and Taguchi T 1998 A novel fiber-optic gas sensing arrangement based on an air gap design and an application to optical detection of humidity *Analytical Sciences*, **14** 633-635
50. Sadaoka Y, Matsuguchi M, Sakai Y, and Murata Y 1992 Optical humidity sensing characterstic of Nafion-dyes composite thin film *Sensors and Actuators B* **8** 443-446
51. Brook T E, Taib M N, and Narayanaswamy R 1997 Extending the range of a fibre-optic relative humidity sensor *Sensors and Actuators B* **38-39** 272-276
52. Otsuki S, Adachi K, and Taguchi T 1998 A Novel Fibre-Optic Gas Sensing Arrangement Based on an Air Gap Design and an Application to Optical Detection of Humidity *Analytical Sciences* **14** 633-635
53. Posch H E and Wolfbeis O S 1988 Fibre-optic humidity sensor based on fluorescence quenching *Sensors and Actuators* **15** 77-83
54. Muto S, Suzuki O, Amano T, and Morisawa M 2003 A plastic optical fibre sensor for real-time humidity monitoring *Measurement Science Technology* **14** 746-750

55. Udd E An overview of fiber-optic sensors 1995 *Review of Scientific Instruments* **66** 4015-4030
56. Udd E Fiber optic sensors based on the Sagnac interferometer and passive ring resonator 1991 *Chapter in Fiber Optic Sensors An Introduction for Engineers and Scientists, John Wiley & Sons*
57. Mitschke F 1989 Fiber-optic sensor for humidity *Optics Letters* **14** 967-969
58. James S W, and Tatam R P 2003 Optical fibre long-period grating sensors characteristics and application *Measurement Science Technology* **14** R49-R61
59. Luo S, Liu Y, Sucheta A, Evans M K, and Tassell R V 2002 Applications of LPG fiber optical sensors for relative humidity and chemical-warfare-agents monitoring *Proceedings of SPIE* **4920** doi 10.1117/12.481973
60. Cooper K R, Ma Y, Wikswo J P, and Kelly R G 2004 Simultaneous monitoring of the corrosion activity and moisture inside aircraft lap joints *Corrosion Engineering, Science and Technology* **39** 339-345
61. Healy W M, Luo S, Evans M, Sucheta A, and Liu Y Development of an optical fiber-based moisture sensor for building envelopes *24th AIVC Conference & BETEC Conference, Ventilation, Humidity Control and Energy Proceedings, Oct 14, 2003, Washington, DC*
62. Yeo T L, Sun T, Grattan K T V, Parry D, Lade R, and Powell B D 2005 Characterisation of a polymer-coated fibre Bragg grating sensor for relative humidity sensing *Sensors and Actuators B* **110** 148-155

63. P Lu, L , Men, and Q Chen Polymer-Coated Fiber Bragg Grating Sensors for Simultaneous Monitoring of Soluble Analytes and Temperature *IEEE Sensors Journal*, **9** 4 , 2009 340-345
64. Cong J, Zhang X, Chen K , and Xu J 2002 Fiber optic Bragg grating sensor based on hydrogels for measureing salinity *Sensors and Actuators B* **87** 487-490
65. Huang X F, Sheng D R, Chen K F, and Zhou H 2007 Low-cost relative humidity sensor based on thermoplastic plastic polyimide-coated fiber Bragg grating *Sensors and Actuators B* **127** 518-524
66. Weaver M O, Montgomery R R, Miller L D, Sohns V E, Fanta G F, and Doane W M 1977 A Practical Process for the Preparation of Super Slurper, a Starch-Based Polymer with a Large Capacity to Absorb Water *Starch* **29** 413-422
67. Sakohara S, Muramoto F, and Asaeda M 1990 Swelling and Shrinking Processes of Sodium Polyacrylate-Type Super-Absorbent Gel in Electrolyte Solutions *Journal of Chemical Engineering of Japan* **23** 119-124
68. Liu M, and Guo T 2001 Preparation and Swelling Properties of Crosslinked Sodium Polyacrylate *Journal of Applied Polymer Science* **82** 1515-1520
69. Sohn O, and Kim D 2003 Theoretical and Experimental Investigation of the Swelling Behavior of Sodium Polyacrylate Superabsorbent Particles *Journal of Applied Polymer Science* **87** 252-257
70. Hua F and Qian M 2001 Synthesis of self-crosslinking sodium polyacrylate hydrogel and water-absorbing mechanism *Journal of Materials Science* **36** 731-738
71. Porter T, Stewart R, Reed J, and Morton K 2007 Models of Hydrogel Swelling with Applications to Hydration Sensing *Sensors* **7** 1980-1991

72. Korsmeyer R W, Lustig S R, and Peppas N A 1986 Solute and Penetrant Diffusion in Swellable Polymers I Mathematical Modeling *Journal of Polymer Science Polymer Physics Edition* **24** 395-408
73. Korsmeyer R W, Lustig S R, and Peppas N A 1986 Solute and Penetrant Diffusion in Swellable Polymers II Verification of Theoretical Models *Journal of Polymer Science Polymer Physics Edition* **24** 409-434
74. Keubkeman C H and Peting D Lecture 40 Beam Deflection *Lecture notes from University of Oregon* <http://pages.uoregon.edu/struct/courseware/461/461_lectures/461_lecture40/461_lecture40.html>, Accessed 12/19/2011
75. Frieden J , Gugnoni Joel, Botsis J, Gmur T , and Coric D 2010 High-speed internal strain measurements in composite structures dynamic load using embedded FBG sensors, *Composite Structures* **92** 1905-1912
76. Haber TC, Mock JL, and Kraus J. 2008 Method and apparatus for high frequency optical sensor interrogation, *US Patent No. 20080106745*
77. Cusano A, Breglio G, Giordano M, and Nicolais L 2005 Low-cost all-fiber Bragg grating sensing system for temperature and strain measurements. *Optical Engineering* **44** 084402.1–2.7
78. Sano Y, and Yoshino T 2003 Fast optical wavelength interrogator employing arrayed waveguide grating for distributed fiber Bragg grating sensors, *Journal of Lightwave Technology*, **21** 132–9
79. Takahashi H, Oda K, Toba H, and Inoue Y, 1995 Transmission characteristics of arrayed waveguide NN wavelength multiplexer *Journal of Lightwave Technology* **13** 447–455

80. Teshima M, Koga M, and Sato K, 1995 Multiwavelength simultaneous monitoring circuit employing wavelength crossover properties of arrayed-wave-guide grating *Electronics Letters* **31** 1595–159
81. Betz D C, Thursby G, Culshaw B, and Staszewski W J 2006 Identification of structural damage using multifunctional Bragg grating sensors I. Theory and implementation *Smart Materials and Structures* **15** 1305–12
82. Betz D C, Staszewski W J, Thursby G, and Culshaw B 2006 Identification of structural damage using multifunctional Bragg grating sensors II. Damage detection results and analysis *Smart Materials and Structures* **15** 1313-1322
83. Tosi D, Olivero M, and Perrone G. 2009 Dynamic strain measurement system with fiber Bragg gratings and noise mitigation techniques *Measurement Science and Technology* **20** 065203.
84. Isago R, and Nakamura K 2009A high reading rate fiber Bragg grating sensor system using a high-speed swept light source based on fiber vibrations. *Measurement Science and Technology*, **20** 034021.
85. Lee J-R, Tsuda H and Toyama N 2007 Impact wave and damage detections using a strain-free fiber Bragg grating ultrasonic receiver *NDT & E Int.* **40** 85–93
86. Grouve W J B, Warnet L, de Boer A, Akkerman R and Wekken J 2008 Delamination detection with fibre Bragg gratings based on dynamic behavior *Composites Science and Technology* **68** 2418–24
87. Ling H Y, Lau K T and Cheng L 2004 Determination of dynamic strain profile and delamination detection of composite structures using embedded multiplexed fibre-optic sensors *Composites Science and Technology* **66** 317–26

88. Christmas S P and Jackson D A 2001 A new method for interrogation of serial arrays of dynamic FBG strain sensors *Measurement Science and Technology* **12** 897–900
89. Garcia-Souto J A and Rivera H L 2000 Multichannel fiber-optic interferometric sensor for measurements of temperature and vibrations in composite materials *IEEE Journal Selected Topics in Quantum Electronics* **6** 780–7
90. Lobo Ribeiro A B, Ferreira L A, Santos J L, and Jackson D A 1997 Analysis of the reflective-matched fiber Bragg grating sensing interrogation scheme *Applied optics* **36** 934-939
91. Wang L K, Chiang Y J, and Yang C C. 2004 Dual Fiber Bragg Grating Strain Sensor System *US Patent 6,829,397B2*
92. Song G, Gu H, and Mo Y L 2008 Smart aggregates multi-functional sensors for concrete structures – a tutorial and a review *Smart Materials and Structures* **17** 033001.
93. Song G, Gu H, and Mo Y L 2008 Piezoceramic-based Smart Aggregate for unified Performance Monitoring of Concrete Structures *US Patent 7,987,728B2*
94. Housner, G W, Bergman, L A, Caughey T K, Chassiakos A G, Claus R O, Masri S F, Skelton R E, Soong T T, Spencer B F, and Yao J T P 1997 Structural Control Past, Present, and Future *Journal of Engineering Mechanics* **123** 897-971
95. Glisic B and Inaudi D 2007 Fibre optic methods for structural health monitoring *Chichester (West Sussex, England) (Hoboken: John Wiley)*
96. Majumder M, Gangopadhyay T K, Chakraborty A K, Dasguta K, and Bhattacharya D K 2008 Fibre Bragg gratings in structural health monitoring – Present status and applications *Sensors and Actuators A Physical* **147** 150-164

97. Li H N, Li D S, and Song G B 2004 Recent applications of fiber optic sensors to health monitoring in civil engineering *Engineering Structures* **26** 1647-1657
98. Schulz W L, Conte J P, and Udd E 2001 Long gage fibre optic Bragg grating strain sensors to monitor civil structures, *Proceedings of SPIE* **4330** 56
99. Leng J S, Mays G C, and Fernando G F 2006 Structural NDE of concrete structures using protected EFPI and FBG sensors *Sensors and Actuators A* **126** 340–347
100. Ansari F 2008 Practical Implementation of Optical Fiber Sensors in Civil Structural Health Monitoring, *Journal of Intelligent Material Systems and Structures*, **19** 1163-1172
101. Chung W and Kang D 2008 Full-scale test of a concrete box girder using FBG sensing system *Engineering Structures* **30** 643–652
102. Dawood T A, Shenoit R A, and Sahin M 2007 A procedure to embed fibre Bragg grating strain sensors into GFRP sandwich structures *Composites A* **38** 217–226
103. Johnson A E , Donlon E P, Braun F D, and Hoang L V 2005 Athermal package for fibre Bragg gratings with two or more bonding regions *US Patent* 6,856,730
104. Moyo P, Brownjohn J M W, Suresh R and Tjin S C 2005 Development of fiber Bragg grating sensors for monitoring civil infrastructure *Engineering Structures* **27** 1828-1834
105. Ansari F 2009 Structural health monitoring with fiber optic sensors *Frontiers of Mechanical Engineering* **4** 103-110
106. Chan T H T, Yu L, Tam H Y, Ni Y Q, Liu, S Y, Chung W H, and Cheng L K 2006 Fiber Bragg grating sensors for structural health monitoring of Tsing Ma bridge background and experimental observation *Engineering Structures* **28** 648-659

107. Gebremichael Y M, Li W, Boyle W J O, Meggit B T, Grattan K T V, McKinley B, Fernando G F, Kister G, Winter D, Canning L, and Luke S 2005 Integration and assessment of fibre Bragg grating sensors in all-fibre reinforced polymer composite road bridge *Sensors and Actuators A Physical* **118** 78-85
108. Kerrouche A, Boyle W J O, Sun T, and Grattan K T V 2009 Design and in-the-field performance evaluation of compact FBG sensor system for structural health monitoring applications *Sensors and Actuators A Physical* **151** 107-112
109. Leng J, and Asundi A 2003 Structural health monitoring of smart composite materials by using EFPI and FBG sensors *Sensors and Actuators A Physical* **103** 330-340
110. Rodrigues C, Felix C, Lage A, and Figueiras J 2010 Development of a long-term monitoring system based on FBG sensors applied to concrete bridges *Engineering Structures* **32** 1993-2002
111. Tennyson R C, Mufti A A, Rizkalla S, Tadros G, and Benmokrane B 2001 Structural health monitoring of innovative bridges in Canada with fiber optic sensors *Smart Materials and Structures* **10** 560-573
112. Torres B, Paya-Zaforteza I, Calderon P A, and Adam J M 2011 Analysis of the strain transfer in a new FBG sensor for Structural Health Monitoring *Engineering Structures* **33** 539-548
113. Ren L, Chen J, Li H N, Song G, and Ji X 2009 Design and application of a fiber Bragg grating strain sensor with enhanced sensitivity in the small-scale dam model *Smart Materials and Structures* **18** 035015
114. Ngoi B K A, Paul J, Zhao L P, Fang Z P 2004 Enhanced lateral pressure tuning of fiber Bragg gratings by polymer packaging *Optical Communications* **242** 425-430

115. Ren L, Li H N, Zhou J, Li D S, and Sun L 2006 Health monitoring system for offshore platform with fiber Bragg grating sensors *Optical Engineering* **45** 084401-1-9
116. Ren L, Development of FBG-based Water Sensor, *Unpublished*.
117. Decommissioning Nuclear Facilities *World Nuclear Association* < <http://www.world-nuclear.org>>, Oct. 27, 2012
118. Fact Sheet on Decommissioning Nuclear Power Plants *United States Nuclear Regulatory Commission* < <http://www.nrc.gov>> Oct. 27, 2012
119. Ferdinand P, Gaucher J C, Magne S, Martinez C., Marty V, Pichon L, Roy O, and Rougeault S 1998 Potential applications for optical fiber sensors and networks within the nuclear power industry *Optical Sensors*, ed. J M Lopez-Higuera
120. Justus B L, Pavlovich K J, Merritt C D, and Huston A L 1999 Optically and Thermally stimulated luminescence characteristics of Cu⁺-doped fused quartz *Radiation Protection Dosimetry* **81** 5-10
121. Ferdinand P, Cahen C, Dessus, and Lesne J L 1983 A two-frequency Optical Fiber Ring interferometer as a sensitive current sensor 4th *International Conference on Integrated Optics and Optical Fiber Communication (Tokyo: Japan)* I pp. 114-115
122. Rogers A 1979 Optical measurement of current and voltage on power systems *Electrical Power Applications* **2** 120-124
123. Ferdinand P and Magne S 2002 *Handbook of Optical Fibre Sensing Technology* ed J M Lopez-Higura (New York Wiley) p 543
124. Ferdinand P, Magne S, Dewynter-Marty V, Martinez C, Rougeault S, and Bugaud M 1997 Applications of Bragg grating sensors in Europe *Proceedings of the Optical Fiber-Sensors Conference (OFS-12) (Williamsburg: USA)* pp 14-19

125. CEB-FIP 2000 State-of-the-Art Report on Bond of Reinforcement in Concrete. *State-of-Art Report Prepared by Task Group Bond Models (former CEB Task Group 2.5) FIB - Féd. Int. du Béton* 1-97
126. Li X 2007 Finite Element Modeling Of Skewed Reinforced Concrete Bridges And The Bond-Slip Relationship Between Concrete And Reinforcement *Auburn University MS Thesis*
127. Abrams D A 1913 Tests of bond between concrete and steel Bulletin No. 71
128. Watstein D 1947 Distribution of bond stress in concrete in pull-out specimens *ACI Journal* **44** 1041–1052.
129. Mains R M 1951 Measurement of the distribution of tensile and bond stresses along reinforcing bars *ACI Journal* **48** 225–252
130. Kenel A, Nellen P, Frank A, and Marti P 2005 Reinforcing Steel Strains Measured by Bragg Grating Sensors *Journal of Materials in Civil Engineering* **4** 423-431
131. Benitez J M and Galvez J C 2011 Bond modeling of prestressed concrete during the prestressing force release *Materials and Structures* **44** 263-278
132. Gustavson R 2004 Experimental studies of the bond response of three-wire strands and some influencing parameters *Materials and Structures* **37** 96–106
133. den Ujil J A 1992 Bond and splitting action of prestressed strand. In *Bond in concrete from research to practice Riga Technical University and CEB, Riga Latvia* **2** 2-79–2-88
134. Abrishami H and Mitchell D 1993 Bond characteristics of pretensioned strand *ACI Materials Journal* **90** 228–235

135. Tassios T, and Bonataki E 1992 Experimental analysis of the bond behaviour of prestressed tendons. In Bond in concrete from research to practice *Riga Technical University and CEB, Riga, Latvia* **1** 2-29–2-37
136. Moerman W, Waele W D, Coppens C, Taerwe L, Degrieck J, Baets R, and Callens M 2001 Monitoring of a Prestressed Concrete Girder Bridge with Fiber Optical Bragg Grating Sensors *Strain* **37** 151-153
137. Lin Y B, Chang K C, Chern J C, and Wang L A 2004 The health monitoring of a prestressed concrete beam by using fiber Bragg grating sensors *Smart Materials and Structures* **13** 712-718

Appendix I

The following graphs are examples of the calibration for the strain and temperature sensors used for chapters six and seven.

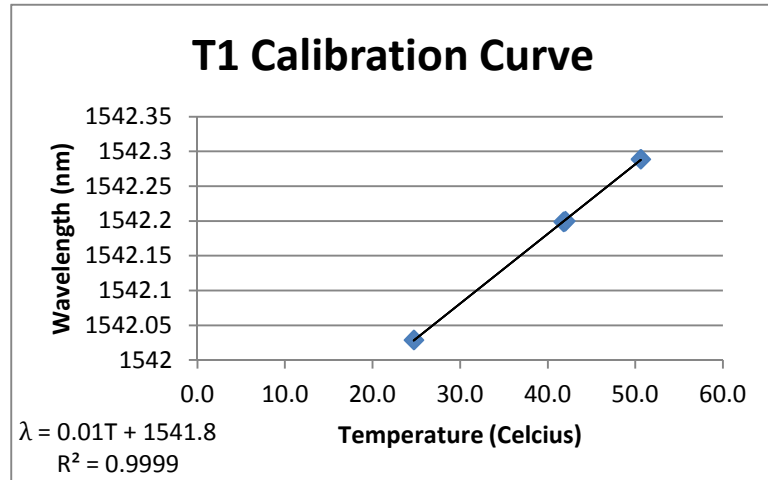


Figure 9-1 Calibration curve of FBG temperature sensor.

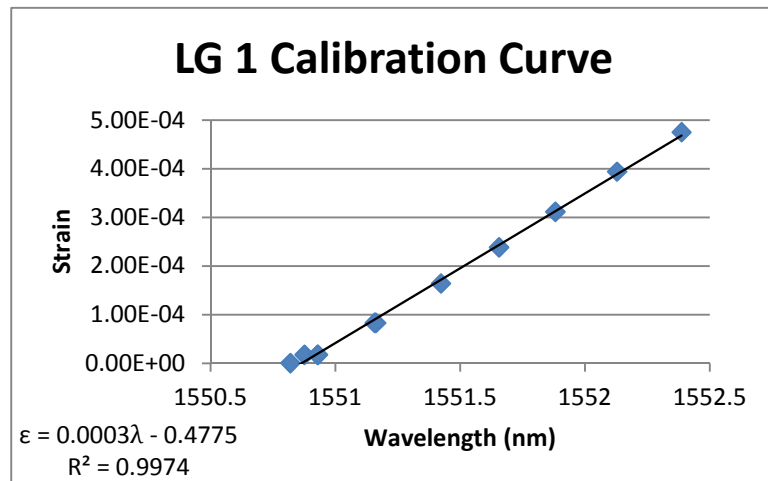


Figure 9-2 Calibration curve of FBG strain sensor.